# Computational Modeling of Spinal Cord Stimulation for Inspiratory Muscle Activation and Chronic Pain Management

by

Hans J. Zander

A dissertation submitted in partial fulfillment
of the requirements for the degree of
Doctor of Philosophy
(Biomedical Engineering)
in the University of Michigan
2021

Doctoral Committee:

Assistant Professor Scott. F. Lempka, Chair
Associate Professor Tim M. Bruns
Associate Professor Parag G. Patil
Professor James D. Weiland

Hans J. Zander

hzander@umich.edu

ORCID iD: 0000-0001-9720-9553

**Acknowledgements**

First, I would like to thank my advisor, Dr. Scott Lempka. He has helped me grow in my writing, critical thinking, presenting, and communication skills. His mentorship always emphasized the need for well-grounded, scientifically accurate models that should be used for meaningful interpretations/predictions, or practical applications. I would also like to thank my dissertation committee, Drs. Tim Bruns, Parag Patil, and Jim Weiland. They have pushed and motivated me to understand the utility, limitations, and purpose of my work. It is very easy to make models without real world value, and they have helped to keep me focused on the clinical implications and needs of this research.

I would like to thank my fellow lab members in the neuromodulation lab, specifically: Bobby Graham, Evan Rogers, Carlos Anaya, Meagan Brucker, Ehsan Mirzakhalili, and Vishwanath Sankarasubramanian. They are always willing and able to help, whether it be brainstorming ideas, editing manuscripts, deciphering code, debugging, fixing my computers/licenses, sitting through practice talks, or even going on Dr. Pepper, Dominos, or Jimmy Johns runs.

Thank you to my fellow graduate students and peers. Including, but not limited to; Elena, Jacopo, Aileen, Pez, Kate, Melissa, Phil, Charles, Katy, Elissa, Alyse, Sam, Claire, Negin, Steven, Michelle, Tyler, Tiff, and Morgan. I appreciate the falafel and burrito contests, repaintings, tubing trips, parties, and the fun we have had together. I would like to specifically thank Danny and Shannon Quevedo for the adventures, board games, shame meals, tv shows, memes, and great

nights. Special thanks as well to Dorsa Ghaffari, Muru Zhou, and Beomseo Koo for the pandemic games, daily lunches, unhealthy amounts of Coco, and for being the most easily distracted people in the office.

I would also like to thank my friends back in Minnesota; Katie Bridges, Lauren Cutshall, and Carter Gruss. You three have kept me sane throughout graduate school, and I am so grateful for our camping and hiking, daytrips, fires, stories, jokes, and challenges. I would like to thank my aunts, uncles, and cousins as well. You are too many to name, but I am blessed to have your support and to be able to enjoy the Thanksgiving dinners, video games, phone calls, pizza barns, investing talks, big bonfires, boat trips, beers, and fantastic corn pudding. I would also like to thank my grandparents, Carl and Marion, Bob and Peggy, and my Auntie My. Some are not with us anymore, but I still feel all their love and support.

Finally, I would like to thank my family, my Mom, Dad, and brother Noah. You have provided me the foundation on which my life grows. I am so thankful for your support, love, guidance, and laughs. You always are there to listen to my worries, fears, hopes, and dreams. I feel so lucky and honored to have you in my life.

## Table of Contents

## List of Tables

## List of Figures

**Abstract**

Spinal cord stimulation (SCS) is a neuromodulation technique that applies electrical stimulation to the spinal cord to alter neural activity or processing. While SCS has historically been used as a last-resort therapy for chronic pain management, novel applications and technologies have recently been developed that either increase the efficacy of treatment for chronic pain or drive neural activity to produce muscular activity/movement following a paralyzing spinal cord injury (SCI). Despite these recent innovations, there remain fundamental questions concerning the neural recruitment underlying these efficacious results. This work evaluated the neural activity and mechanisms for three SCS applications: both conventional SCS and closed-loop SCS for pain management, as well as ventral, high frequency spinal cord stimulation (HF-SCS) for inspiratory muscle activation following a SCI.

I developed computational models to both predict the neural response to SCS and explore factors influencing neural activation. Models consisted of three components: a finite element model (FEM) of the spinal cord to predict the potential fields generated by stimulation, biophysical neuron models, and algorithms to apply time-dependent extracellular potentials to the neuron models and simulate their response.

While this cutting-edge modeling methodology could be used to predict neural activity following stimulation, it was unclear how anatomical and technical factors affected neural predictions. To evaluate these factors, I designed an FEM of a T9 thoracic spine with an implanted electrode array. Then, I sequentially removed details from the model and quantified the changes in neural predictions. I identified several factors with large (>30%) effects on neural thresholds,

including overall electrode impedance (for voltage-controlled stimulation), the electrode position relative to the spine, and dura mater conductivity. This work will be invaluable for basic science and clinical applications of SCS.

Next, I developed a canine model to evaluate T2 ventral HF-SCS for inspiratory muscle activation after an SCI. This model infrastructure included two neuron populations hypothesized to lead to inspiratory behavior: ventrolateral funiculus fibers (VLF) leading to diaphragm activation and inspiratory intercostal motoneurons. With this model, I predicted robust VLF and T2-T5 motoneuron recruitment within the experimental range of stimulation. I used this model framework to optimize several design parameters related to HF-SCS for inspiration. The optimal lead design parameters were evaluated via *in vivo* experiments, which found excellent agreement with model predictions. This work expands our mechanistic understanding of this novel therapy, improves its implementation, and aids in future translational efforts towards human subjects.

Finally, I developed a computational model to evaluate closed-loop SCS for chronic pain management. This work characterized the neural origins of the evoked compound action potential (ECAP), the controlling biomarker of closed-loop stimulation. This modeling work showed that ECAP properties depend on activation of a narrow range of axon diameters and quantified how anatomical and stimulation factors (e.g., CSF thickness, stimulation configuration, lead position, pulse width) influence ECAP morphology, timing, and neural recruitment. These results improve our mechanistic understanding of closed-loop stimulation and neural recruitment during SCS.

In summary, this dissertation work improves the methodology, validation, and applications of computational models of SCS. It also has direct applications to the clinical/pre-clinical implementation of SCS and may be invaluable for expanding the utility and efficacy of several

treatments. The improved mechanistic understandings of neural activation described in this work may also aid in the future development of these therapies.

# Chapter 1: Introduction

Spinal cord stimulation (SCS) is a neurostimulation technique predominantly used for the treatment of neuropathic chronic pain that is refractory to conventional medical management [1]. Over 50,000 epidural SCS devices are implanted every year, with total annual sales exceeding $1.8 billion in 2014 [2]–[4]. Despite the widespread clinical use of SCS, its analgesic mechanisms are poorly understood, leading to an overall moderate success rate, limited improvements in patient quality of life, and poor long-term efficacy [2]. In addition to chronic pain, SCS has also recently been evaluated as a treatment for paralysis following spinal cord injury and can drive motor control of various muscles below the site of injury [1]. This novel application of SCS has been used to generate reaching and grasping motions in the upper limbs, walking in the lower limbs, as well as to generate respiratory muscle activation in the inspiratory intercostals and diaphragm [5]–[8]. While studies have identified the neural targets of upper and lower limb motor control by SCS, there remain many unknowns about SCS for inspiratory motor control [6], [7], [9]–[11]. Overall, even though SCS is a prominent treatment with several applications, more research needs to be done to understand the neural activation and mechanisms that lead to efficacious treatments.

## 1.1 Spinal cord stimulation

### *1.1.1 Background*

SCS was first developed in the 1960's to treat chronic pain and is the most prevalent form of clinical neuromodulation [1], [12]. Conventional SCS applies biphasic 50 Hz electric

stimulation in the dorsal epidural space of the lower thoracic spinal cord to drive neural activation within the dorsal spinal cord (**Figure 1.1**) [2], [12], [13]. One benefit of SCS stems from the unique anatomy and function of the cord, which aggregates sensory information from the periphery, processes it, then transmits it towards the brain (or vice versa). In fact, at every vertebral level, the dorsal columns carry information from all body regions caudal to that level [12]. Consequently, stimulation applied to the cord via a single electrode can lead to neuromodulatory effects, such as pain relief, over large areas of the body [14].

### *1.1.2 Spinal cord anatomy*

Traditional SCS targets axons traveling in the dorsal columns (DCs) of the spinal cord, which carry proprioceptive and sensory (afferent) information from the periphery to the brain (**Figure 1.1**) [15]. Because stimulation activates proprioceptive and/or mechanoreceptive fibers in the DCs, patients experience paresthesia (e.g., tingling, buzzing, pins and needles, pressure). The locations of the perceived paresthesias are hypothesized to depend on which dermatomes (**Figure 1.1**) are stimulated, and so these paresthesias are commonly used to guide the lead location during the implantation procedure and the selection of stimulation parameters [12]. In fact, overlap of paresthesia and pain has been shown to be a necessary component to pain relief during conventional SCS [12], [16]. At each spinal cord level, the cord has both ventral and dorsal roots (DR) which carry neural signals to and from the corresponding dermatome of the body. While stimulation of the dorsal columns can relieve pain, activation of the dorsal rootlets is generally thought to lead to discomfort or painful sensations [15]. Consequently, a common goal of SCS for the treatment of pain is to maximize DC activation and minimize DR activation [15]. However, targeting of specific spinal regions can prove challenging due to the highly conductive cerebrospinal fluid (CSF) that surrounds the cord. This fluid limits precise targeting of spinal cord

structures using epidural contacts, reduces the current flow into the cord to less than 10% of the total injected current, and is highly varied across patient populations [15], [17].

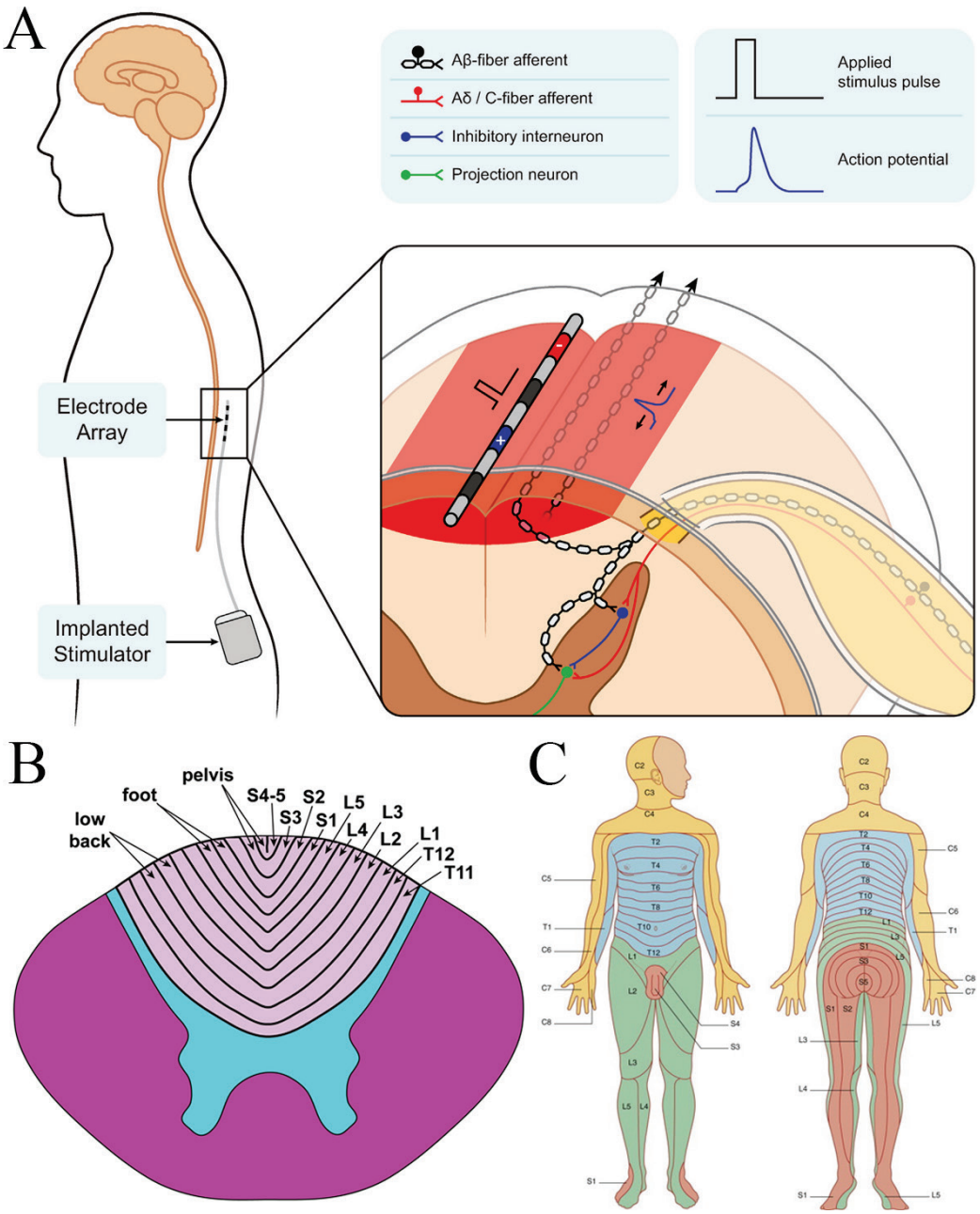


**Figure 1.1**: Spinal cord stimulation and spinal cord anatomy. Images adapted from [2], [18]. A. Spinal cord stimulation for pain with implanted array and stimulator. Stimulation targets large Aβ fibers within the DCs, initiating orthodromic and antidromic action potentials. These are believed to "close the gate" and prevent projection neuron pain transmission. B. The dermatome layout of the dorsal columns of the cord. Dermatome refers to the area of skin innervated by a single spinal nerve. C. The corresponding dermatome layout of the skin.

## 1.2 Chronic pain

### *1.2.1 Background*

Pain is defined as "an unpleasant sensory and emotional experience associated with, or resembling that associated with, actual or potential tissue damage" [19]. To be chronic, pain must persist for a minimum of 3-6 months [20]. Pain is a multi-faceted disorder, and in addition to the physical pain itself, there are associated economic, social, and psychological problems that manifest from the pain that can negatively impact quality of life [21]. A number of studies have also shown statistically significant relationships between pain, depression, and suicide [22], [23]. The economic impact of pain is tremendous as well, and studies have found that healthcare costs for chronic pain can be up to $300 billion per year, with an additional $335 billion per year cost from the loss of productivity associated with pain [21].

While the number of patients and economic impacts of chronic pain are immense, the treatment options for patients experiencing chronic pain are limited. The most common treatment for chronic pain is pharmaceuticals, including nonsteroidal anti-inflammatory drugs, acetaminophen, and opioids [24]. These pharmaceuticals are often inadequate to manage pain, and in the case of opioids, are highly addictive and contribute to the ongoing opioid epidemic in the United States [24]–[26]. Additional conventional therapies for pain management include physical therapy, nerve blocks, lesions, injections, and counseling; however, these treatment options too often provide inadequate relief for pain, or have success rates that are unreported in literature [24], [27]–[30]. Neuropathic pain (i.e., pain caused by a lesion or disease of the somatosensory nervous system) tends to be more severe, more likely to be chronic, and less responsive to conventional medical management (CMM) relative to nociceptive pain [19], [31], [32]. A recent study

evaluating the efficacy of CMM on a neuropathic pain patient population found that only 9% of patients successfully responded to CMM alone [27].

SCS is currently approved by the United States Food and Drug Administration for neuropathic limb pain that is refractory to CMM [2]. Despite being a last resort treatment for many patients, conventional SCS therapy for pain has success rate of around 58% (successful treatment is defined as a ≥ 50% overall reduction in pain), leaving a significant portion of patients with few remaining treatment options [4]. Importantly, the market for SCS for pain has only continued to grow over recent years, and some estimates predict the global market size may grow to over $4.1 billion by the end of 2026 [33].

### *1.2.2 The gate theory of pain*

The conventional mechanistic understanding of SCS is derived from the gate control theory of pain (**Figure 1.1A**, **Figure 1.2**) [13]. In this theory, small (S) Aδ and C fibers carry painful sensations from the periphery to the spinal cord and synapse onto transmission (T) neurons (also called projection neurons) which send the pain signals to the brain. The gate theory hypothesizes that SCS antidromically activates large (L) Aβ fibers within the DCs. The resultant action potentials travel caudally down the dorsal columns to collateral branch points. From these branches, the action potentials travel (now orthodromic) into the dorsal horn and excite inhibitory interneurons in the substantia gelatinosa (SG) (**Figure 1.1A**, **Figure 1.2**). The excited SG inhibitory interneurons then "close the gate" on pain (i.e., inhibit the transmission of the pain signals within the spinal cord, preventing them from reaching the brain) (**Figure 1.1A**) [2], [13]. While the original gate theory hypothesized some aspect of "central control" over the gate (**Figure 1.2**), there was little known about it at the time, and it was believed that the predominant factor was the segmental effect [34], [35]. However, recent evidence suggests that supraspinal

mechanisms, such as descending inhibition, may also play a larger role in reducing pain [2], [36]. While the gate control theory of pain provides the original foundation for the development of SCS, the theory is incomplete and detailed knowledge on how SCS provides pain relief is still lacking [1], [4], [37]. For example, the gate control theory of pain cannot explain pain relief persisting after terminating stimulation, the long-term reduction in SCS effectiveness, or why SCS tends to be less effective for treatment of nociceptive pain conditions [2], [36].

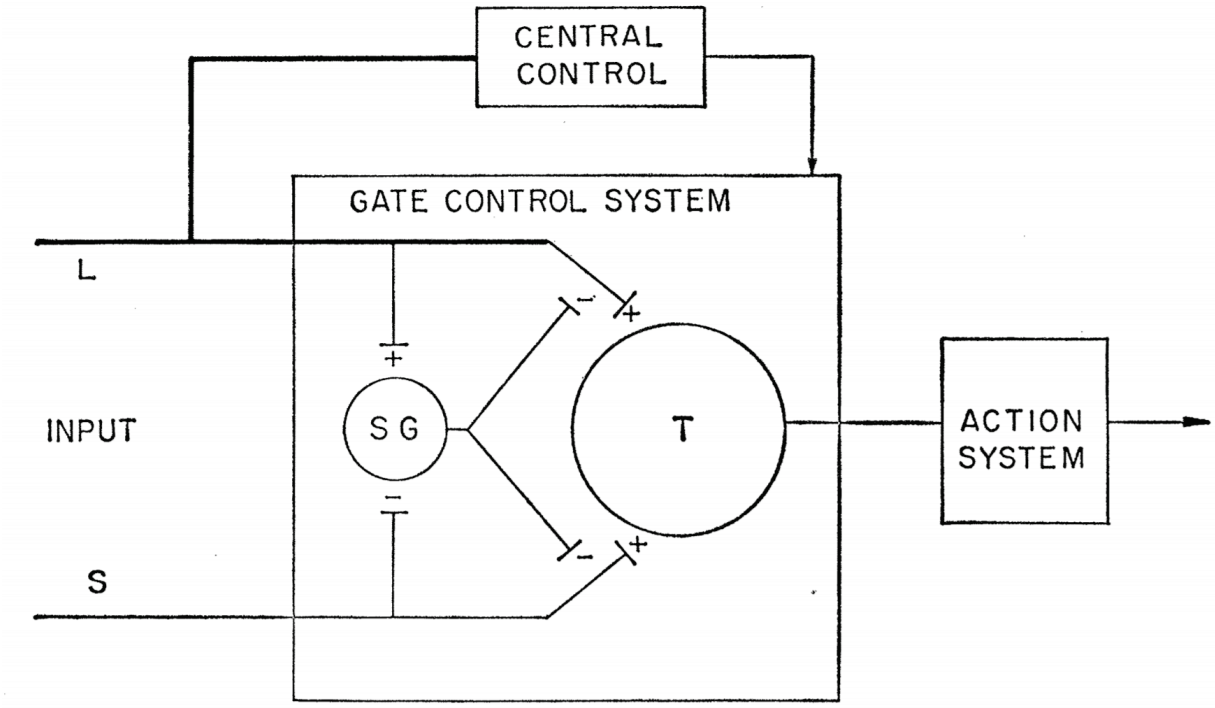


**Figure 1.2**: The gate control theory of pain. Adapted from [13]. Large (L) and small (S) diameter neurons activate transmission (T) cells in the dorsal horn of the spinal cord. This theory postulates that large fiber activation excites (+) an inhibitory cell in the substantia gelatinosa (SG) which, in turn, inhibits (-) transmission of painful sensations.

In recent years, several novel stimulation paradigms and techniques have emerged that demonstrate increased treatment efficacy. Unlike conventional paresthesia-based SCS, these novel stimulation paradigms (i.e., kilohertz-frequency SCS, burst SCS) can produce analgesia without concomitant paresthesias [2]. These therapies have been shown to be more efficacious than

traditional SCS [38]–[42]. While preliminary evidence suggests alternate mechanisms of pain relief other than the traditional gate control theory of pain, nobody has yet been able to definitively explain how pain is suppressed by these novel applications and there remain further unanswered questions about their mechanisms (including the lack of concomitant paresthesia, role of supraspinal processing for these therapies, or that kilohertz-frequency SCS does not necessitate pain-paresthesia overlap like conventional SCS) [2], [43]–[45].

### *1.2.3 Closed-loop spinal cord stimulation*

Recently, another novel form of SCS implements closed-loop control over stimulation. This paradigm actively controls the stimulation amplitude by measuring the evoked compound action potentials (ECAP) generated in the spinal cord during stimulation. ECAP recordings represent the summation of individual action potentials generated within the spinal cord in response to stimulation, and as such are representative of the total neural recruitment active by stimulation [2], [46]. A recent double-blind, randomized, controlled trial (the Evoke study) showed that significantly greater and more clinically meaningful pain relief was obtained using closed-loop stimulation over traditional stimulation paradigms [42]. Closed-loop stimulation addresses a major limitation of traditional open-loop stimulation: movement of the spinal cord within the spinal canal. This movement (up to ~2-3 mm in the lower thoracic cord) is a result of postural changes, breathing, movement, or heart rate and can result in overstimulation and/or understimulation of the spinal cord. During closed-loop stimulation, stimulation amplitudes are continually adjusted to keep the ECAP amplitude (and consequently the total neural recruitment) within the pre-defined therapeutic window (**Figure 1.3**) [2], [41], [47], [48].

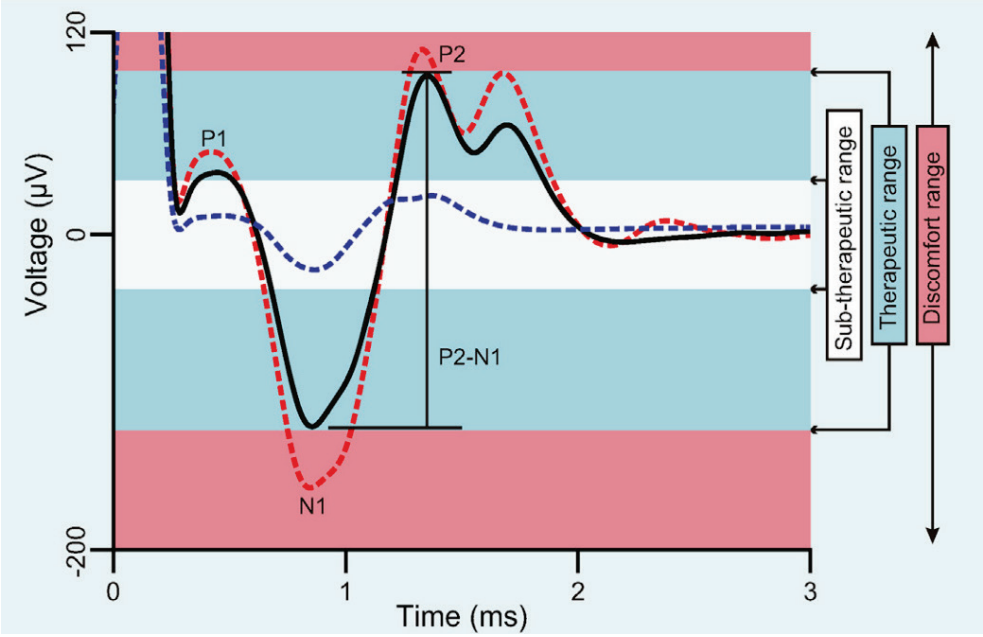


**Figure 1.3**: Evoked compound action potential generated during closed-loop spinal cord stimulation. Adapted from [2]. The ECAP signal consists of 3 peaks, the initial positive peak (P1), the initial negative peak (N1), and the second positive peak (P2). The stimulation amplitude is adjusted to keep the P2-N1 amplitude within the therapeutic range of treatment.

ECAPs are typically measured using inactive electrodes on the implanted SCS array(s). ECAPs have a multiphasic morphology, which is typically separated into three standard peaks, an initial positive peak (P1), a secondary negative peak (N1), and a tertiary positive peak (P2) (**Figure 1.3**). ECAP amplitudes are most commonly characterized by evaluating the difference between the N1 and P2 peak, which ranges between 10 μV and 1.5 mV [48]. There are many factors that may influence the shape and amplitude of the ECAP recordings, including the stimulation configuration, recording configuration, lead location, electrode geometry, contact size, electrode material, stimulation frequency, pulse amplitude, and pulse width, in addition to patient anatomical factors, such as the size of the spinal cord and its position within the thecal sac [46], [48]–[50]. However, the effects of these factors on neural recruitment and the overall ECAP size, shape, and timing, have not been well characterized.

## 1.3 Spinal cord injury

### *1.3.1 Background*

A spinal cord injury (SCI) is damage to the spinal cord or surrounding nerves that affects the conduction of motor and/or sensory signals [51]. This injury can lead to lasting long-term physical challenges and diminishing quality of life [52]. It is estimated that in the United States, between 294,000 to 368,000 people are currently living with a SCI, with an average of about 17,810 new injuries occurring each year [53]. The primary causes of SCI in the United States since 2015 are vehicular accidents and falls, which together account for over 70% of injuries [53]. Severity of the injury is highly dependent on both the extent of damage and location, with high-level injuries increasing the extent of patient paralysis.

### *1.3.2 Ventilation following an SCI*

A spinal cord injury in the upper cervical cord may disrupt the bulbospinal tracts, which carry neural signals from the brain to the respiratory muscles [7], [54]. For severe high level cervical SCIs (C3-C5), patients may suffer complete paralysis of both the inspiratory and expiratory muscles (**Figure 1.4**) [55]. For these patients, long-term mechanical ventilation may be required for survival [7]. In 2019, nearly 20% of patients admitted to a hospital for an SCI required the use of a respirator at rehabilitation entry [56]. In a retrospective analysis, the strongest negative predictor of survival during the first year following hospital discharge was ventilator dependence, with respiratory complications accounting for 31% of deaths [57].

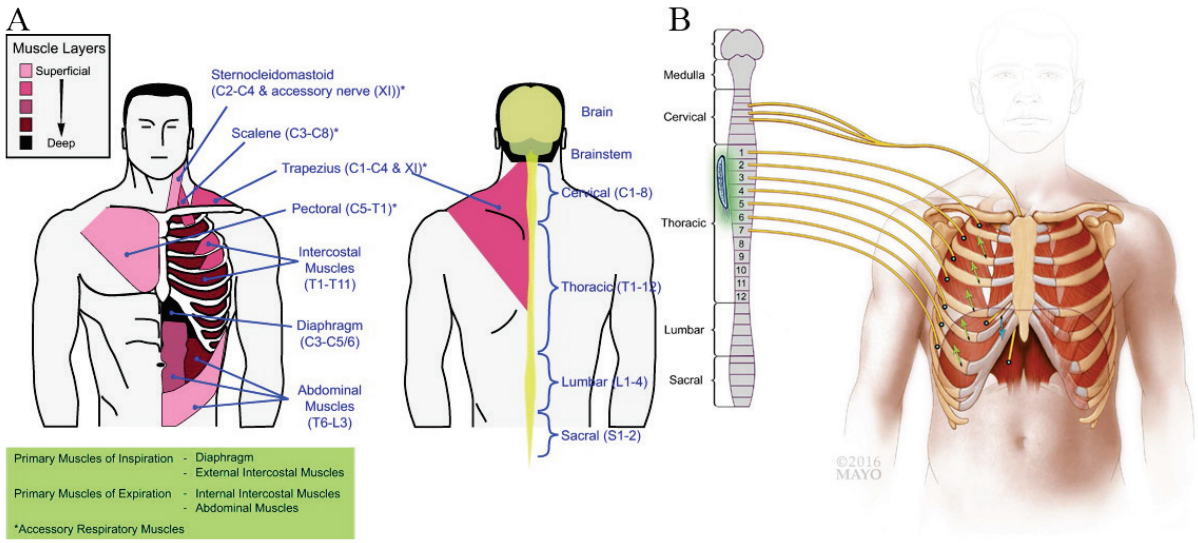


**Figure 1.4**: The primary respiratory muscles and hypothesized neural connections. Adapted from [58], [59]. A. The primary muscles of inspiration and expiration and the locations, as well as the innervation level for humans. B. The diaphragm is innervated by the phrenic motoneurons (C3-C6 spinal level). Intercostal motoneurons positioned in the upper thoracic spinal cord (T1-T7) predominantly innervate inspiratory (external, parasternal) intercostal muscles [60].

While mechanical ventilation may be a necessity for patients, it is a double-edged sword that has many limitations. It is extremely expensive, and patients requiring long-term ventilation are ranked highest by Medicare in terms of cost per patient [57]. Ventilation can also induce trauma to the airway which can lead to infection, result in limited mobility or speech, or produce high levels of noise [7]. Patients on long-term ventilation also have a fear of disconnection of the device due to loss of power [7].

### *1.3.3 Diaphragm pacing*

A safe and practical neurostimulation alternative to mechanical ventilation is diaphragm pacing [7], [61]. Diaphragm pacing is a technique in which electrodes are placed next to the phrenic nerve or within the diaphragm itself. Stimulation of these electrodes leads to diaphragm activation, generating inspiration. As compared to mechanical ventilation, diaphragm pacing reduces barotrauma, increases speech, and reduces respiratory infection [62]. Additionally, patients with

diaphragm pacing have enhanced mobility and less concern about power outages leading to device disconnection. Importantly, one study found that over a 20-year period, diaphragm pacing led to no significant change in longevity as compared to mechanical ventilation [7], [63]. However, diaphragm pacing has several significant limitations, namely inadequate inspired volumes, and incomplete diaphragm activation (possibly due to the synchronous activation of motor units in the diaphragm, the lack of concurrent intercostal activation, or electrical stimulation recruiting motoneurons in the reverse recruitment order compared to natural breathing).

### *1.3.4 High-frequency spinal cord stimulation (HF-SCS) for respiration*

In recent years, there have been several novel applications of SCS that have shown promise to treat paralysis caused by a paralyzing SCI. These techniques use spinal cord stimulation to produce coordinated movement in the absence of supra-spinal inputs [1]. To date, these novel approaches have been used for several applications, including stepping/gait control in rats and humans, reaching/grasping in non-human primates, cough in canine and humans, and inspiratory muscle activation in canines, among others [1], [6], [7], [9], [64]–[67]. For each technique, the efficacy of motor activation varies based on the location of the spinal cord stimulator and neural targets, the applied stimulus waveform, and the spinal circuitry leading to muscular activation (among many other factors) [7], [11], [67]. In order to effectively translate these new therapies into viable clinical technologies, it is vital to understand the neural activation and mechanisms leading to coordinated muscle activity in response to stimulation [1].

One novel approach, high-frequency spinal cord stimulation (HF-SCS) for inspiratory muscle activation, has the potential to address many of the limitations associated with mechanical ventilation or diaphragm pacing in patients with a ventilator-dependent tetraplegics. In several recent canine experiments, HF-SCS (300 Hz) was applied at the ventral surface of the T2 spinal

cord to produce near maximal inspiratory activity in C2-sectioned dogs [7], [68]–[71]. Interestingly, stimulation led to synchronous inspiratory activity in both the diaphragm as well as the intercostal muscles [7]. Additionally, HF-SCS produced asynchronous patterns of EMG and single motoneuron firing frequencies that were similar to natural breathing [7], [68], [69]. However, the exact mechanisms through which SCS produces activation of both the intercostal muscles as well as activation of the diaphragm are unknown [7], [11].

Due to the upper thoracic (T2) implantation of the stimulating contact, HF-SCS is unlikely to directly lead to activation of the phrenic motor neurons (C3-C6) (**Figure 1.4**). However, stimulation may lead to direct activation of the local inspiratory intercostal muscles, which are predominantly located in the upper thoracic cord [7], [72]. As for diaphragm activation, it is hypothesized that stimulation activates the intercostal-to-phrenic reflex arc as it ascends in the ventrolateral funiculus of the spinal cord [7], [73], [74]. While these neurons and pathways have been identified as possible targets for stimulation, the extent of activation and optimal stimulation configuration to target them remains unknown.

## 1.4 Computational modeling

### *1.4.1 Background*

Computational models of SCS and other neurostimulation technologies are frequently used to provide a well-controlled environment to help answer questions that are difficult to answer experimentally. Biophysical models have been used in the analysis of many diverse neuromodulation therapies, including deep brain stimulation, transcranial electrical stimulation, nerve stimulation, dorsal root ganglia stimulation, and retinal stimulation, among others [75]–[82]. Modeling provides many advantages to other experimental and clinical based research techniques,

including a highly controlled working environment, the ability to systematically and rapidly evaluate a large number of parameters, and the capability to investigate highly invasive techniques in full scale human models. Models are also highly repeatable, relatively rapid to implement and analyze, and cost-effective [1]. Because of these benefits, models have been important in the design process for a large variety of research fields, and have been essential for the development of our modern understanding and implementation of SCS [1].

### *1.4.2 History of SCS modeling*

Computational modeling has a long and complex history that has helped advance the technical aspects of SCS and improve the mechanistic understanding of the therapy. The first models of SCS were developed in the 1980's by Coburn and Sin to evaluate the diameters of dorsal column fibers activated by stimulation [83]–[85]. Computational models of SCS were further expanded in the 1990's by Holsheimer and colleagues, who further validated modeling, explored neural targets of stimulation, designed improved stimulation configurations and lead designs, and investigated how anatomic variabilities changed model predictions [15], [17], [37], [86]–[89]. In recent years, computational modeling has been used to improve several aspects of SCS, including lead design, programming procedures, and waveform parameters [90]–[93]. Various studies have also attempted to elucidate a more mechanistic understanding of SCS for existing and novel stimulation waveforms, locations, and indications [6], [9], [43].

### *1.4.3 Computational modeling variability across literature*

The primary goal of this dissertation is to use computational models to evaluate the neural activation generated by spinal cord stimulation. To build valid models, it is imperative that they include the appropriate anatomical details to accurately predict the electric fields generated during

stimulation. However, previous computational models of SCS include various simplifications to lessen the computational demand or decrease the time spent developing the model. These simplifications, such as representing the vertebral column to be a cylinder, can alter the shape of the electric field and affect the predictions of the models [43]. Importantly, these simplifications are not uniform across literature, and model designs may vary extensively between studies[1] [9], [43], [88], [90], [92], [94], [95]. To use computational models to understand SCS, we must first understand the effects of these simplifications and quantitatively describe how these changes affect neural predictions.

### 1.5 Summary of dissertation

In this work, I use computational models to evaluate SCS for pain control and for inspiration following SCI. These models evaluate the direct effects of stimulation (i.e., how does stimulation directly influence neural activation or recruitment). Therefore, this dissertation focuses on identifying the types and properties of spinal neurons activated by stimulation. My work further evaluates changes in neural activation thresholds due to variations in the electric field (arising from anatomical simplifications, FEM design, electrode design, lead location, stimulation waveform/polarity, and stimulation configuration). The work included in this thesis highlights the potential for SCS for a variety of clinical treatments while also emphasizing the importance of computational models to quantitatively explore hypotheses and explain phenomena that are exceedingly difficult to investigate otherwise.

[1] A comprehensive list comparing model simplifications across literature can be found in Table 1 of Khadka et al., 2020. [95]

Chapter 2 of this dissertation focuses on identifying which anatomic and technical details are necessary to evaluate computational models of SCS. In this work, I developed a detailed FEM of the lower thoracic spinal cord (dorsal T9 implanted electrode array) and evaluated how model predictions change when details were removed. I investigated how activation thresholds change as a function of several anatomical variables (e.g., spine geometry, dorsal rootlet anatomy), stimulation types (i.e., voltage-controlled vs. current-controlled), electrode impedances, lead positions, lead types, and electrical properties of surrounding tissues (e.g., dura conductivity, frequency-dependent conductivity). In this chapter, I found several anatomic and modeling factors that significantly impact model predictions. These factors should be considered for future clinical and modeling work, and they are used in model development for subsequent chapters of this dissertation.

In Chapter 3, I describe a computational model to evaluate neural recruitment during ventral high-frequency spinal cord stimulation (HF-SCS) applied at the T2 spinal level in the canine spinal cord. Previous experimental work determined that stimulation at this level resulted in recruitment of both the diaphragm and the inspiratory intercostals [7], [68], [70], [96]. However, the activation thresholds, extent of activation, and optimal electrode configurations (i.e., lead separation, contact spacing, and contact length) to activate these neural elements remain unknown. My model evaluated two neural targets: ascending fibers in the ventrolateral funiculus of the spinal cord and the local intercostal motoneurons. For this work, I determined the extent of activation of both neural targets and determined lead designs to maximize their recruitment. These lead designs were evaluated via *in vivo* experiments, and the computational model predictions demonstrated excellent agreement with experimental results.

In Chapter 4, I present a computational model to evaluate a novel form of closed-loop SCS for chronic pain management. While closed-loop SCS has been shown to be more effective than conventional open-loop stimulation, there remain open questions on the origins of the recorded evoked compound action potential (ECAP) used as a control signal [2], [42]. For this chapter, I developed a computational model of closed-loop SCS by simulating the neural response to stimulation and then using the neural response to simulate an ECAP recording. I used this model to investigate the origins of the ECAP waveform, timing, and amplitude. I evaluated how the waveform changes in response to changes in lead position, dorsal CSF thickness, lead lateralization, pulse width, and stimulation configuration.

In summary, there were several main goals and achievements for this work. I evaluated variations in model design and identified several design considerations that have impacts on future model development. I also developed the first computational model of HF-SCS for inspiratory muscle activation and improved the mechanistic understanding and technical implication of this therapy. My results will also aid in future translational efforts. Finally, I developed a model to simulate closed-loop SCS, which I used to identify the neural origins of the ECAP. I also evaluate how this waveform changed with variations in anatomy and stimulation. This work impacts the implementation and understanding of closed-loop stimulation can be used to improve validation of future computational models.

# Chapter 2: Anatomical and Technical Factors Affecting the Neural Response to Epidural Spinal Cord Stimulation

Part of the material for this chapter has been adapted with modifications from the following publication:

1. **H. J. Zander** *et al.*, "Anatomical and technical factors affecting the neural response to epidural spinal cord stimulation", *J. Neural Eng.*, vol. 17, no. 3, 2020, doi: 10.1088/1741-2552/ab8fc4. [97]

## 2.1 Abstract

*Objective*

Spinal cord stimulation (SCS) is a common neurostimulation therapy to treat chronic pain. Computational models represent a valuable tool to study the potential mechanisms of action of SCS and to optimize the design and implementation of SCS technologies. However, it is imperative that these computational models include the appropriate level of detail to accurately predict the neural response to SCS and to correlate model predictions with clinical outcomes. Therefore, the goal of this study was to investigate several anatomic and technical factors that may affect model-based predictions of neural activation during thoracic SCS.

*Approach*

We developed computational models that consisted of detailed finite element models of the lower thoracic spinal cord, surrounding tissues, and implanted SCS electrode arrays. We positioned multicompartment models of sensory axons within the spinal cord to calculate the activation threshold for each sensory axon. We then investigated how activation thresholds changed as a function of several anatomical variables (e.g., spine geometry, dorsal rootlet anatomy), stimulation type (i.e., voltage-controlled vs. current-controlled), electrode impedance, lead position, lead type, and electrical properties of surrounding tissues (e.g., dura conductivity, frequency-dependent conductivity).

*Main results*

Several anatomic and modeling factors produced significant percent differences or errors in activation thresholds. Rostrocaudal positioning of the cathode with respect to the vertebrae had a large effect (up to 32%) on activation thresholds. Variability in electrode impedance produced significant changes in activation thresholds for voltage-controlled stimulation (40 to 51%) but had little effect on activation thresholds for current-controlled stimulation (less than 13%). Changing the dura conductivity also produced significant differences in activation thresholds (up to 60%).

*Significance*

This study demonstrates several anatomic and technical factors that can affect the neural response to SCS. These factors should be considered in clinical implementation and in future computational modeling studies of thoracic SCS.

## 2.2 Introduction

Spinal cord stimulation (SCS) is a common neurostimulation therapy that can be used to treat a variety of conditions that are refractory to traditional medical management (e.g., chronic pain, poor ventilation, spasticity, as well as poor locomotion following spinal cord injury) [5], [8], [12], [98]. For chronic pain management, it is estimated that more than 50,000 devices are implanted each year with annual sales of more than $1.8 billion in 2014 [3], [4]. However, even with the prevalence of this procedure, the mechanisms of action of SCS for pain are still largely unknown and only 58% of patients respond to SCS (i.e., ≥ 50% pain reduction) [4].

Computational models of SCS and other neurostimulation technologies are frequently used to provide a well-controlled environment to help answer questions that are difficult to answer experimentally. Computational analysis of SCS typically occurs in two stages: (1) a volume conductor model (e.g., finite element model (FEM)) is used to calculate the electric fields generated within the spinal cord during SCS, and (2) neuron models (e.g., multicompartment cable models) are used to estimate the neural response to stimulation. In the past, multiple groups have used computational models to improve several aspects of SCS, including lead design, programming procedures and parameters (e.g., pulse width), and electrode design [87], [90]–[92], [99], [100]. Several studies have also attempted to elucidate the mechanisms of action of various forms of SCS [9], [15], [43]. While these studies have improved our understanding of the physiological and technical factors relevant to SCS, many phenomena associated with SCS are still unknown [2], [4], [101].

To help improve SCS technologies, it is imperative that computational models include the appropriate anatomical details to accurately calculate the electric fields and corresponding neural response during SCS [94]. Computational models of SCS are subject to several assumptions that may limit their ability to characterize the physiological and technical factors relevant to SCS. To

lessen the demand of computational resources and model design, numerous anatomic simplifications are incorporated into the volume conductor models. For example, while some previous studies include detailed three-dimensional (3D) representations of the vertebral column and vertebrae, other studies represent the spine with a simplified cylindrical domain around the epidural tissue [9], [43], [90], [92], [102]. These models may also exclude certain anatomical domains, such as the dura mater, spinal cord root structures, and encapsulation tissue surrounding the implanted electrode arrays. Similarly, computational models typically ignore the frequency-dependent electrical properties of the relevant biological tissues. Across studies, model designs may vary extensively [9], [43], [88], [90], [92], [94].

Previous computational modeling studies provide a means to qualitatively assess how certain model design parameters affect neural recruitment during SCS (e.g., [86], [103], [104]); however, only limited quantitative analyses have been performed, especially for thoracic SCS. Therefore, the goal of this study was to quantify how model simplifications and designs influence neural recruitment. To do this, we developed multiple FEMs containing the spinal cord and its surrounding anatomy, as well as an implanted SCS electrode array. Each FEM contained different simplifications in the design that could influence neural activation. We then calculated the extracellular voltage distributions generated by SCS for either current-controlled (CC) or voltage-controlled (VC) stimulation. We coupled the corresponding voltage distribution to multicompartment models of spinal cord axons and calculated the activation threshold for each axon. Finally, we calculated the percent difference or error in activation thresholds between FEMs to quantify the effects of specific anatomical factors and/or model simplifications on the neural response to SCS. The results of this study suggest that several simplifications can be incorporated into model designs without significantly affecting the predicted neural response to SCS. However,

our results suggest that some conditions, such as the position of the stimulating electrodes relative to the vertebrae or the electrode impedance, may have a large influence on activation thresholds. Therefore, this study highlights anatomical factors that should be considered during clinical implementation of SCS and future computational modeling studies investigating the physiologic and technical factors relevant to thoracic SCS.

### 2.3 Methods

We used computational models to investigate the direct axonal response to SCS. We used the following three steps to perform our analysis: (1) We created a FEM to calculate the extracellular voltage distribution generated in the spinal cord during SCS, (2) we generated and distributed multicompartment sensory axon models within the dorsal roots (DR) and white matter of the spinal cord, and (3) we assessed the axonal response to stimulation by applying the voltage distributions (step 1) to the axon models (step 2). Initially, our model included many anatomical details, such as rootlets, dura, realistic vertebrae, etc. We then introduced common simplifications into our model design and evaluated changes in activation thresholds. We used the most detailed model (i.e., the 'base' model) as the ground truth in our analysis and compared the activation thresholds predicted from simplified models to the thresholds predicted by this 'base' model. We have previously used this approach and a similar model design to evaluate evoked compound action potentials generated in the spinal cord during SCS [105].

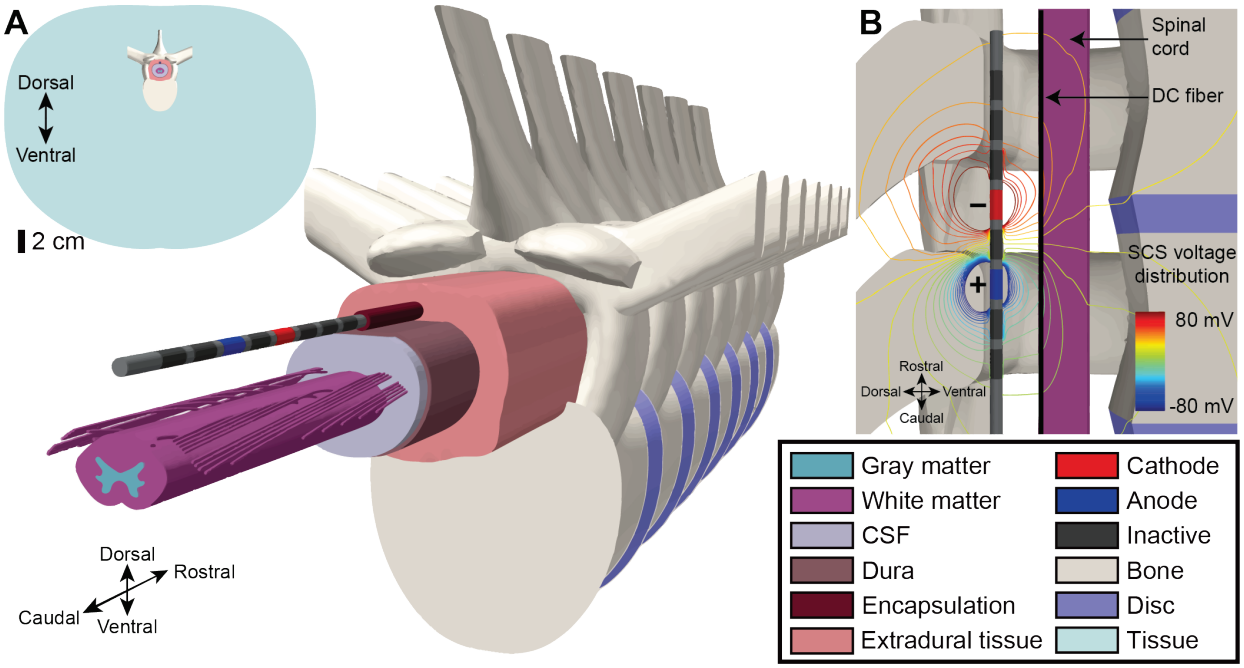


**Figure 2.1**: Finite element model (FEM) of spinal cord stimulation (SCS). We developed a FEM of the spinal cord with an implanted eight-electrode percutaneous SCS lead, encapsulation, explicit representation of the dorsal rootlets, dura mater, and a 3D vertebral column including intervertebral discs. A) Axial view and an exploded isometric view of the 'base' FEM. B) Isopotential tissue voltages generated by 1 V bipolar stimulation.

### *2.3.1 Modeling process*

*Step 1: Create an FEM and calculate the extracellular voltages generated by SCS:*

We generated a 3D FEM of SCS at the lower thoracic spinal levels. This FEM included representations of gray matter, white matter, cerebrospinal fluid (CSF), dura, epidural tissue, bone, intervertebral discs, electrode encapsulation layer, and bulk tissue. We defined the gray and white matter boundaries of the spinal cord model using cadaveric cross-sections at the T11 spinal cord level [106], [107]. At each spinal cord level, we included a dorsal root that was divided into five 0.25 mm diameter rootlets [108]–[110]. We separated the entry of each rootlet into the spinal cord by 3.28 mm in the rostrocaudal direction, resulting in a dorsal root entry zone of 13.1 mm [108]. Each rootlet individually ascended 46.5 mm rostrocaudally through the CSF and followed a curved trajectory before entering the spinal cord (**Figure 2.1A**) [107], [111]. We surrounded the spinal

cord with a CSF domain that was enclosed by dura mater with a thickness of 0.3 mm [112]. The distance between the dorsal surface of the spinal cord and the dura was 3.2 mm [43]. Exterior to the dura, we placed an epidural tissue domain that included a percutaneous SCS lead with eight annular electrodes. Each electrode had a length of 3 mm and a diameter of 1.3 mm with an edge-to-edge spacing of 1 mm. We also included a 0.3 mm thick encapsulation layer domain surrounding the electrode array [113]. We placed the lead and encapsulation layer domain on the dorsal surface of the dura at the anatomical midline of the spinal cord. Previous modeling work has demonstrated improved predictions of neural thresholds with an anatomically based vertebral column [97]. Therefore, we stacked seven identical and anatomically-accurate T9 vertebrae with intervertebral discs to represent the vertebral column surrounding the epidural space [114]–[116]. The center-to-center distance between each vertebrae was 22.2 mm, which resulted from an endplate thickness of 19.3 mm and an intervertebral disc thickness of 3.86 mm [114], [116]. Finally, we included a bulk tissue layer with dimensions representative of an average male body [117]–[119] (**Figure 2.1A**). We discretized our FEM into tetrahedral elements using 3matic (Materialise NV, Belgium), defining a region of interest (within 17.5 mm of the SCS lead) with higher node densities near the lead and resulted in a finalized mesh containing more than 51 million elements.

To calculate the voltage distributions generated during SCS, we imported our mesh into COMSOL (COMSOL Inc., USA). We initially defined electrical conductivities for each tissue type using data from the literature (**Table 2.1**) [43], [92], [113]. We then adjusted the electrical conductivity of the encapsulation layer until the FEM produced electrode impedances resembling average impedance values measured clinically (i.e., monopolar impedance of 370 Ω) [90]. We calculated the extracellular voltage distributions by assigning Dirichlet boundary conditions of a

unit stimulus (i.e., 1 V) at the cathode and ground at the anode (i.e., 0 V). We modeled inactive contacts as equipotential with zero net current across their surface. We applied an insulating boundary condition to the outer boundaries of the FEM. We performed simulations for bipolar stimulation with a center-to-center spacing of 8 mm between the anode and cathode. We calculated electrostatic FEM solutions with an iterative equation solver using the conjugate gradient method (**Figure 2.1B**). The resulting voltages were interpolated and applied to the axon models presented in Step 2.

**Table 2.1**: Electrical conductivities used in the frequency-independent FEMs

| Tissue | Conductivity (S/m) | Reference |
|---|---|---|
| Gray matter | 0.230 | [120] |
| White matter (longitudinal) | 0.600 | [120] |
| White matter (transverse) | 0.083 | [120] |
| Cerebrospinal fluid | 1.700 | [120] |
| Dura mater | 0.600 | [43] |
| Encapsulation layer[a] | 0.110 | |
| Extradural tissue | 0.250 | [92] |
| Vertebral bone | 0.020 | [121] |
| Intervertebral disc | 0.650 | [92] |
| General thorax | 0.250 | [120] |

[a]Adjusted so that monopolar electrode impedance matched clinical values

*Step 2: Generate electrical models of axons within the spinal cord and rootlets*

Next, we created multi-compartment models of Aβ somatosensory axons populating the white matter and dorsal rootlets of our FEM model. While other methods of axonal modeling, such as the activating function (AF) (i.e., second-order spatial derivative of the extracellular voltage and predictor of the relative response of the axon transmembrane voltage at stimulus onset) and driving force predictors, allow for more rapid predictions, multi-compartment models typically

provide more accurate estimates of the neural response to stimulation [122]–[126]. These multi-compartment models were based on previously-published mammalian motor axons that were adapted to have properties of sensory fibers [77]. Each Aβ-fiber was a double-cable model consisting of nodes of Ranvier separated by three distinct finite impedance myelin segments: the myelin attachment segment (MYSA), paranodal main segment (FLUT), and internode regions (STIN) (**Figure 2.2A**) [127]. The nodes of Ranvier contained active (fast $Na^+$, persistent $Na^+$, fast $K^+$, and slow $K^+$) and passive (linear leak conductance, capacitance) membrane properties that reproduce action potential characteristics and conduction velocities observed in sensory axons [128], [129].

Previous studies have traditionally distributed fibers throughout the spinal cord by placing them in a grid with an arbitrary number of fibers [43], [90]. In this work, we used histological measurements from the superficial dorsal columns in the human spinal cord to define an anatomically-realistic distribution of axons that covered a wide range of axon diameters (i.e., 5.7 – 16.0 μm) found in the human spinal cord [14]. We assumed an average density of 22.92 fibers/1000 $\mu m^2$ throughout the spinal cord. Our 3D spinal cord model (step 1) contained white matter with a cross-sectional area of 23.62 $mm^2$. Therefore, we estimated that our anatomically-realistic fiber distribution should contain approximately 541,000 axons. Because the double-cable axon model [127] was developed for discrete fiber sizes (i.e., 5.7, 7.3, 8.7, 10.0, 11.5, 12.8, 14.0, 15.0, 16.0 μm), we calculated the proportion of fibers belonging to each diameter from the fiber-size distribution histograms [14]. To reduce computational demand, we only included ~1% of each fiber diameter population in our model analysis. Due to the sparsity of larger fiber diameters, all fibers larger than 11.5 μm were combined into the 11.5 μm fiber population; resulting in 5 fiber-diameter populations; 5.7, 7.3, 8.7, 10.0, and 11.5 μm with 1145, 717, 274, 89 and 28 fibers,

respectively (2253 total fibers). Even with 1% of anatomical sampling, the number of fibers tested provided sufficient spatial sampling resolution to calculate activation thresholds throughout the spinal cord. We initially placed each fiber-diameter population randomly throughout the white matter, and then used Lloyd's algorithm (Voronoi iterations) to evenly distribute the fibers throughout the white matter (**Figure 2.2B**) [130], [131]. The white matter fibers ran along the rostrocaudal axis of the FEM while the DR fibers followed the trajectory defined for each rootlet. Where the DR fibers entered the spinal cord, they branched into ascending and descending daughter fibers running parallel to the white matter fibers [111]. The parent DR fibers had larger diameters relative to the dorsal column daughter fibers to account for the higher peripheral conduction velocity relative to spinal cord conduction velocity [132]. Additionally, the diameter of the branching node was 1.5 times larger than the parent DR fiber [88]. The DR fiber diameters were 7.3, 8.7, 10.0, 12.8, and 14.0 μm with corresponding white matter daughter fiber diameters of 5.7, 7.3, 8.7, 10.0, and 11.5 μm, respectively. We performed the neuron simulations with the software package, NEURON, within the Python programming environment [133].

*Step 3: Assess the axonal response to SCS*

In the third step of our model analysis, we assessed the direct axonal response to SCS. We estimated the direct axonal response to SCS by applying the extracellular voltages calculated in the FEM (step 1) to the axon models (step 2). To model the time-dependent output generated by an implantable pulse generator (IPG) during CC or VC stimulation, we included an equivalent circuit model of the IPG output (**Figure 2.3A**) [37]. We then simulated the time-dependent voltage output at the electrode tissue interface and scaled our spatial FEM voltage solutions to calculate the corresponding spatiotemporal voltage distributions [37]. We interpolated the scaled extracellular voltages onto the model axons described above and used a bisection algorithm (error

< 1%) to calculate the activation threshold for each axon (**Figure 2.2C**). For each set of model parameters, we calculated the activation thresholds (i.e., the stimulation amplitude needed to induce at least two action potentials) for axons located at each position in the spinal cord (**Figure 2.2D**). Using these maps, we calculated the percent difference in activation thresholds throughout the white matter and the DR fibers for the various FEM comparisons summarized below (see **Table 2.2**). These maps show the percent difference or percent error at each position within the spinal cord. The final percent difference/error plots represent the mean percent difference/error for all the fiber diameter groups tested.

*2.3.2 Anatomical factors and model complexity*

We used this model-based approach to characterize how various anatomical factors and model conditions affected the corresponding activation thresholds. We systematically varied several parameters (e.g., impedance, cathode position) and simplified the FEM design. We then compared predictions from different conditions and/or simplifications to the activation thresholds predicted with our original model. For each condition, we calculated the activation thresholds and corresponding percent errors or percent differences for bipolar stimulation using both CC and VC stimulation. We used the term, percent error, for situations in which simplifications were made to the model. We used the term, percent difference, for situations in which different conditions (and not simplifications) were considered in the analysis.

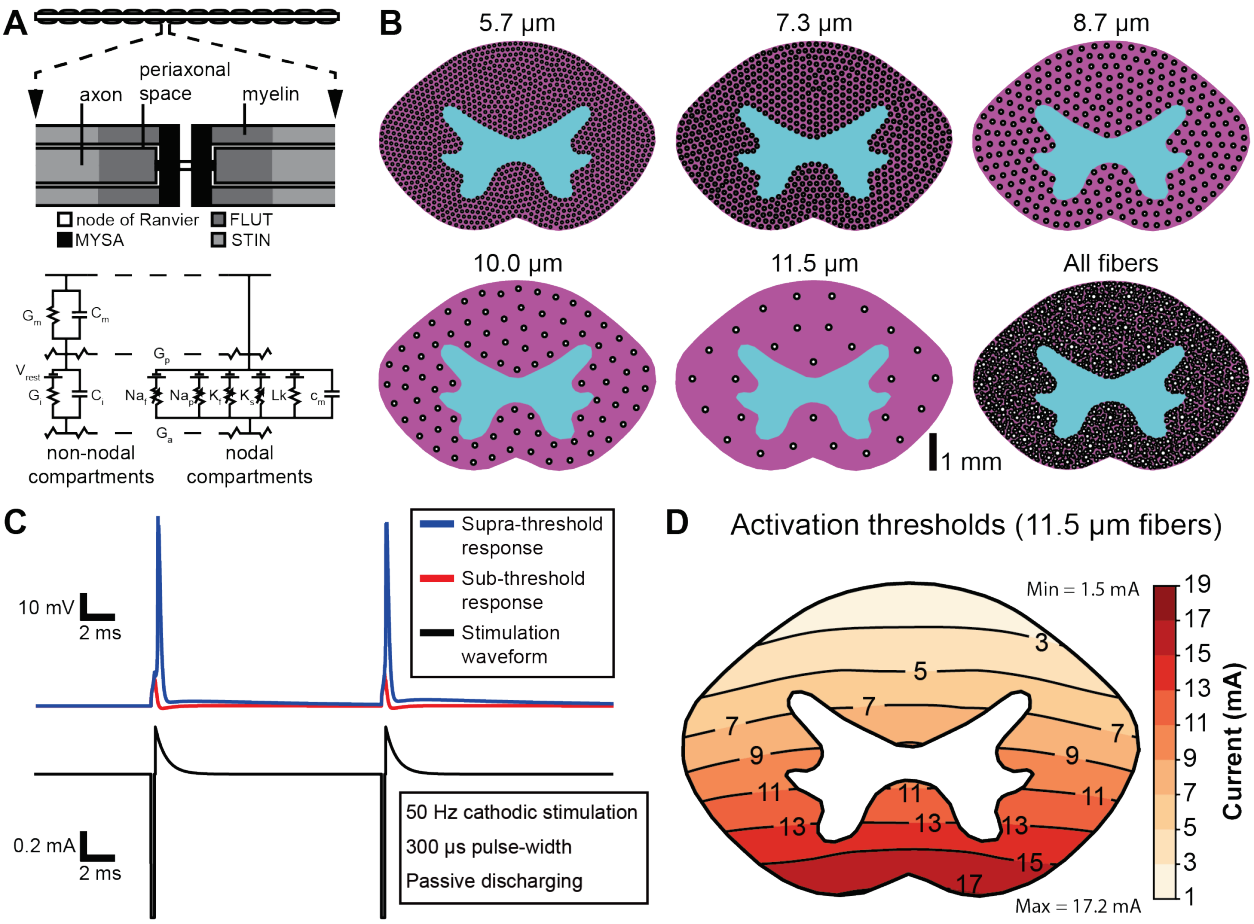


**Figure 2.2**: Axon models and response to stimulation. A) We represented sensory fibers using multicompartment cable models of myelinated axons. Figure adapted from [127]. B) We generated a range of axon diameters (5.7 – 11.5 µm) within the white matter to match the densities found in the superficial dorsal columns in the human spinal cord [14]. To reduce computational demand, we only represented 1% of fibers of each diameter. We distributed fibers evenly throughout the white matter using Lloyd's algorithm [130], [131]. C) We determined the axonal response to stimulation by interpolating the SCS-induced extracellular voltages directly onto the axon models. We then determined the minimum stimulation amplitude needed to elicit a supra-threshold response. D) Thresholds required to elicit an action potential throughout the spinal cord for 11.5 µm fibers in the 'base' model.

*Electrode impedance*

Due to the foreign body reaction, SCS electrode impedance can vary over time and between individual electrodes [103], [134], [135]. These impedance fluctuations can potentially affect the corresponding neural response (e.g., higher electrode impedance may require a higher stimulation amplitude for activation). Therefore, to investigate the effects of electrode impedance on neural activation, we varied the conductivity of the encapsulation layer to mimic low impedance (~270

Ω) and high impedance (~470 Ω) conditions that have been observed in clinical monopolar SCS impedance measurements (368 ± 98 Ω) [90] (**Figure 2.3**).

*Electrode position relative to vertebrae*

Previous work has shown that the vertebral lamina structure may affect the amplitude of recordings of extradural spinal cord compound action potentials generated during SCS [105], [136]. We hypothesized that electrode placement relative to the complex 3D structure of the vertebrae could also produce differences in activation thresholds during SCS. Therefore, we evaluated activation thresholds when the cathode was placed between two successive laminae versus directly ventral to the lamina (**Figure 2.4A**). Throughout the manuscript, we refer to a cathode placement between two laminae as the 'base' model.

We also evaluated the significance of electrode position relative to vertebrae for a laminectomy or paddle-style electrode array. The 3-column paddle electrode array had 16 electrodes with 1.5 mm x 4 mm electrode contacts. For this paddle lead, we calculated the activation thresholds for a bipolar stimulation configuration when the cathode was adjacent to a lamina versus when the cathode was in between two laminae (**Figure 2.5A**).

*Cylindrical bone domain*

A common simplification of previous SCS models is to represent the vertebral column as a cylindrical domain that does not vary along the rostrocaudal axis [43], [91], [102], [137], [138]. Models with this simplified bone domain are unable to consider potential threshold changes due to the detailed 3D structure of vertebrae and the relative position of the stimulating electrodes. To evaluate the potential consequences of using a cylindrical bone regime, we generated an additional FEM with a cylindrical bone using dimensions from a previously-published model [43].

*Dorsal root (DR) anatomy*

A majority of SCS modeling studies do not include explicit representations of the dorsal roots and/or rootlets within the FEM mesh [43], [90], [92], [103], [111], [136]. These models place the DR axons within the CSF until they enter the spinal cord. Because white matter has a lower conductivity than CSF (**Table 2.1**) [120], explicit representation of the DR anatomy within the FEM could potentially influence DR fiber activation thresholds and the site of action potential initiation. In simplified FEMs, the rapid transition in electrical conductivities at the boundary between the CSF and the spinal cord could lead to an overestimation of axon excitability (i.e., lower activation thresholds) with action potential initiation occurring at the node of Ranvier closest to this discontinuity. Therefore, we calculated activation thresholds with and without explicit representations of the DR anatomy within the FEM. We utilized the same finite element mesh in both conditions. For the model solutions with and without the DR anatomy, we set the DR rootlet domain conductivity to the conductivity of white matter and CSF, respectively (**Table 2.1**).

*Dura mater*

The spinal cord is enclosed within a thin dural sac that may influence the neural response to SCS. The electrical properties of dura mater are largely unknown [139]. Therefore, in computational models of SCS the conductivity of the dura has been modified to best match clinical impedance measurements. The conductivity values used in computational models typically range from 0.02 S/m to 0.6 S/m [10], [43], [90], [93], [111], [138], [140]–[142]. To examine the effect of dura conductivity on model-based activation thresholds, we performed simulations for two commonly used dura conductivities (i.e., 0.03 and 0.6 S/m) that largely covered this range (**Figure 2.6**). We adjusted the conductivity of the encapsulation layer for both models so that the average

model impedance matched the average clinical impedances reported in [90] (i.e., encapsulation conductivities of 0.29 and 0.11 S/m for dura conductivities of 0.03 and 0.6 S/m, respectively).

*Frequency-dependent electrical tissue properties*

Biological tissues have frequency-dependent electrical properties that can potentially affect the extracellular voltages generated within the spinal cord during SCS [121]. However, SCS modeling studies typically assume frequency-independent tissue properties that only account for the resistive component of the tissue impedance at a single frequency [143], [144]. This assumption has been justified by previous studies for traditional SCS frequency ranges [144], [145]. However, novel forms of SCS apply stimulation pulses in the kilohertz frequency range, which could potentially affect the validity of this assumption. One new form of SCS applies stimulation pulses at a rate of 10 kHz [40]. To consider potential frequency-dependent volume conduction in this frequency range, we used a Fourier FEM approach to calculate time- and space-dependent solutions of the voltage distributions generated during 10 kHz SCS [143]. We calculated the first 50 frequency components of the Fourier series expansion for a 10 kHz biphasic rectangular waveform (30 μs pulse width, 20 μs interphase interval) that matched the waveform applied by the clinical 10 kHz SCS system [43], [146]. In our base FEM, we defined the frequency-dependent conductivity and permittivity of each tissue, except for the encapsulation, using the Cole-Cole equations and data from [147] (**Figure 2.7A**). We assigned the encapsulation layer domain the frequency-independent electrical conductivity from **Table 2.1** and a relative permittivity of zero. We solved Laplace's equation at each of the 50 frequencies and scaled each FEM solution by the corresponding frequency component of the Fourier series expansion of the stimulation waveform. Finally, we used the inverse Fourier transform to calculate the spatiotemporal voltage distribution generated during 10 kHz SCS. To consider the effects of frequency-dependent volume conduction

on the neural response to 10 kHz SCS, we calculated the activation thresholds for both frequency-independent and frequency-dependent FEM solutions. For the frequency-independent FEM, we assigned electrical conductivities using the Cole-Cole parameters at the lowest solved frequency, 10 kHz, and assigned a permittivity of zero for each domain [147]. We assessed the neural response during 50 ms of 10 kHz stimulation (i.e., 500 pulses). We defined the activation threshold as the minimum stimulation amplitude that produced repetitive firing in the axon under consideration during the entire stimulation window (**Figure 2.7D**).

## 2.4 Results

We performed model-based analysis of SCS under a wide range of model conditions to investigate how various anatomical and technical factors affected the predicted neural response to SCS. For each set of model conditions, we calculated the activation thresholds for each axon and the corresponding percent change in activation. In our 'base' model, the minimum stimulation amplitude that produced continuous action potential firing was 1.5 mA and 1.3 V for CC and VC stimulation, respectively (300 μs pulse width, 50 Hz cathodic leading biphasic pulse). Activation was lowest at the most superficial aspect of the dorsal columns and occurred in the largest fiber size tested (i.e., 11.5 μm fibers). Our model thresholds fell within clinical sensory thresholds [148]. Relative to the white matter fibers, the DR fibers had higher minimum stimulation thresholds of 2.1 mA and 1.8 V for CC and VC SCS, respectively. This trend agreed with previous modeling studies [90].

*2.4.1 Electrode impedance*

To examine how variability in electrode impedance affected activation thresholds, we performed simulations for low- and high-impedance conditions. We altered the encapsulation layer conductivity so that the overall monopolar model impedance mimicked the range of clinically-reported monopolar impedances (i.e., 368 ± 98 Ω) [90]. We used encapsulation layer conductivities of 0.25 and 0.07 S/m to produce average monopolar electrode impedances of 270 and 470 Ω for the low- and high-impedance model conditions, respectively.

In the low-impedance model, the minimum white matter fiber activation thresholds were 1.5 mA and 0.9 V for CC and VC stimulation, respectively. In the high-impedance model, the minimum white matter fiber activation thresholds were 1.5 mA and 1.6 V for CC and VC stimulation, respectively. For VC stimulation, the high vs. low electrode impedance conditions produced large percent differences in activation thresholds of 37.6 – 50.8% (**Figure 2.3C**, **Table 2.2**). The largest difference was in the superficial dorsal columns. However, for CC stimulation, the high vs. low impedance conditions only produced small percent differences in activation thresholds of -12.9 – 1.0%, with the largest difference at the ventral side of the spinal cord (**Figure 2.3C**, **Table 2.2**).

We observed a similar trend for activation of the dorsal rootlets. In the low-impedance model, the minimum DR fiber activation threshold was 1.5 mA and 1.4 V for CC and VC stimulation, respectively. In the high-impedance model, the minimum DR fiber activation threshold was 1.5 mA and 2.2 V for CC and VC stimulation, respectively. The high vs. low impedance conditions produced mean percent differences in DR fiber activation thresholds of 44.2% and -5.9% for VC and CC stimulation, respectively (**Table 2.2**).

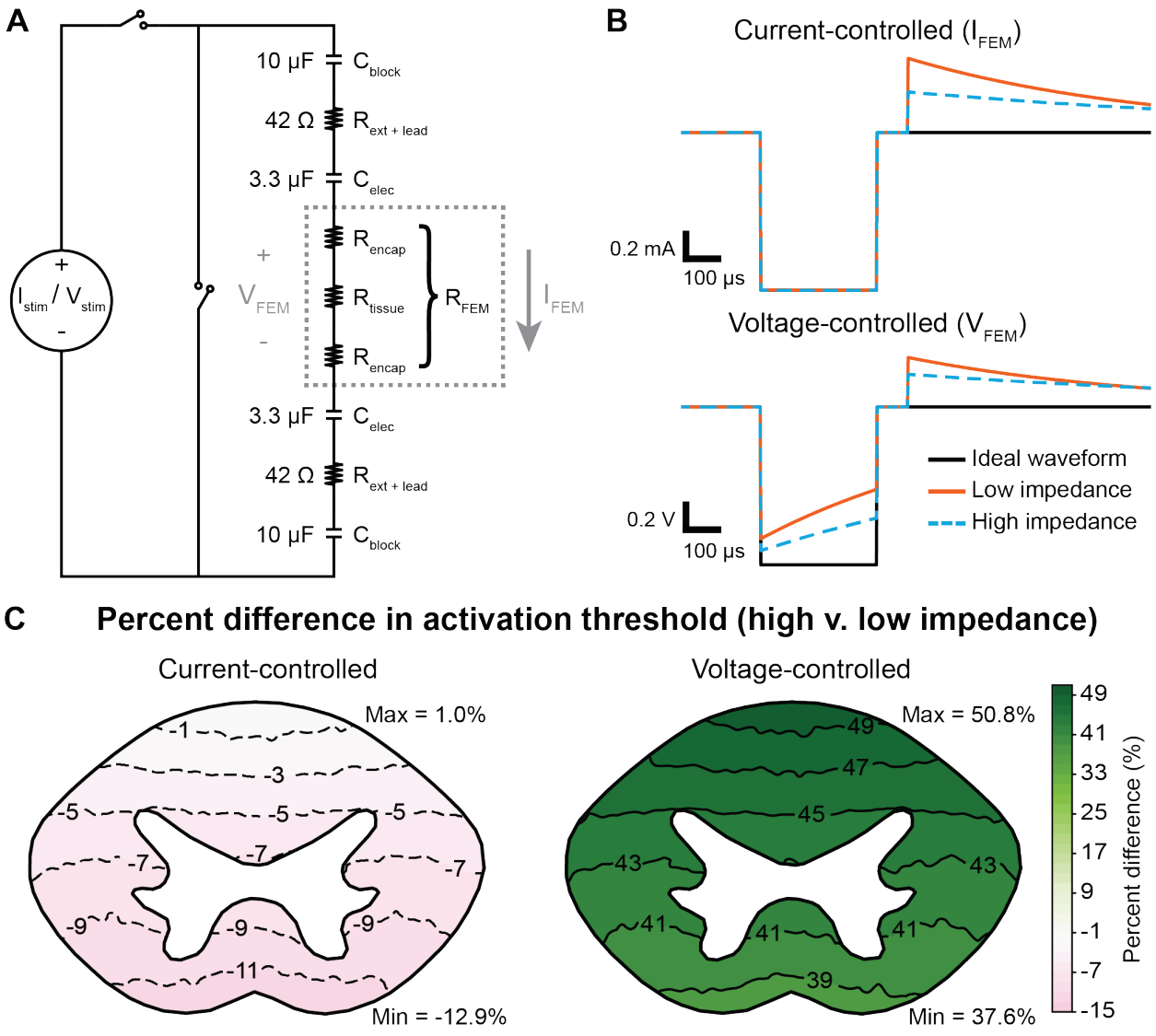


**Figure 2.3**: Effect of model impedance on activation thresholds. A) The bipolar circuitry model of an implantable pulse generator applying either current-controlled (CC) or voltage-controlled (VC) stimulation [37]. Switches allow the model to reproduce the output of the IPG in a time-dependent manner (applying the stimulus pulse and capacitive discharging). B) Computer simulations of $I_{FEM}$ for CC stimulation and $V_{FEM}$ for VC stimulation resulting from altered impedance. We varied the conductivity of the encapsulation layer to produce the high impedance ($R_{FEM}$ = 855 Ω) or low impedance ($R_{FEM}$ = 429 Ω) waveforms for bipolar stimulation. C) Percent difference in activation thresholds between the high impedance model and the low impedance model for both CC and VC stimulation.

**Table 2.2**: Range of percent error/difference between the various model conditions

| **Model comparison** | **Percent error/difference (%)** | | | |
|---|---|---|---|---|
| | **Spinal cord fibers** | | **Dorsal rootlet fibers** | |
| | *Current-controlled* | *Voltage-controlled* | *Current-controlled* | *Voltage-controlled* |
| High vs. low impedance[a] | [-12.9, 1.0] | [37.6, 50.8] | [-8.9, 1.7] | [41.5, 51.3] |
| Cathode position relative to vertebrae (percutaneous)[a] | [-31.5, -10.4] | [-29.7, -8.8] | - | - |
| Cathode position relative to vertebrae (paddle)[a] | [-10.5, 1.4] | [-10.4, 1.3] | - | - |
| Vertebrae vs. cylindrical bone domain | [-17.9, -7.2] | [-16.8, -6.2] | [-15.9, -6.9] | [-14.4, -5.9] |
| Rootlets in the FEM | [-1.5, 2.7] | [-1.8, 2.9] | [-1.8, 1.4] | [-1.9, 1.5] |
| Dura conductivity | [-2.3, 61.3] | [-6.8, 57.3] | - | - |
| Frequency-dependent vs. Frequency-independent | [-3.2, 7.0] | - | [-4.3,8.2] | - |

[a]Percent difference was used for the calculation as opposed to percent error

*2.4.2 Anatomical considerations*

To examine the potential significance of electrode placement relative to the vertebrae, we compared activation thresholds with the cathode placed between two successive laminae versus the cathode placed directly ventral to the lamina (**Figure 2.4A**). With the cathode placed between two successive laminae, the minimum activation thresholds were 1.5 mA and 1.3 V for CC and VC stimulation, respectively. With the cathode placed ventral to the lamina, the minimum activation thresholds were 1.3 mA and 1.2 V for CC and VC stimulation, respectively. For CC stimulation, the two electrode placements produced percent differences in activation threshold of -31.5 to -10.4%. For VC stimulation, the change in electrode placement produced percent differences in activation threshold of -29.6 to -8.8% (**Table 2.2**; Cathode position relative to vertebrae (percutaneous)). The average percent differences were largest in the ventral spinal cord for both CC and VC stimulation (**Figure 2.4B**).

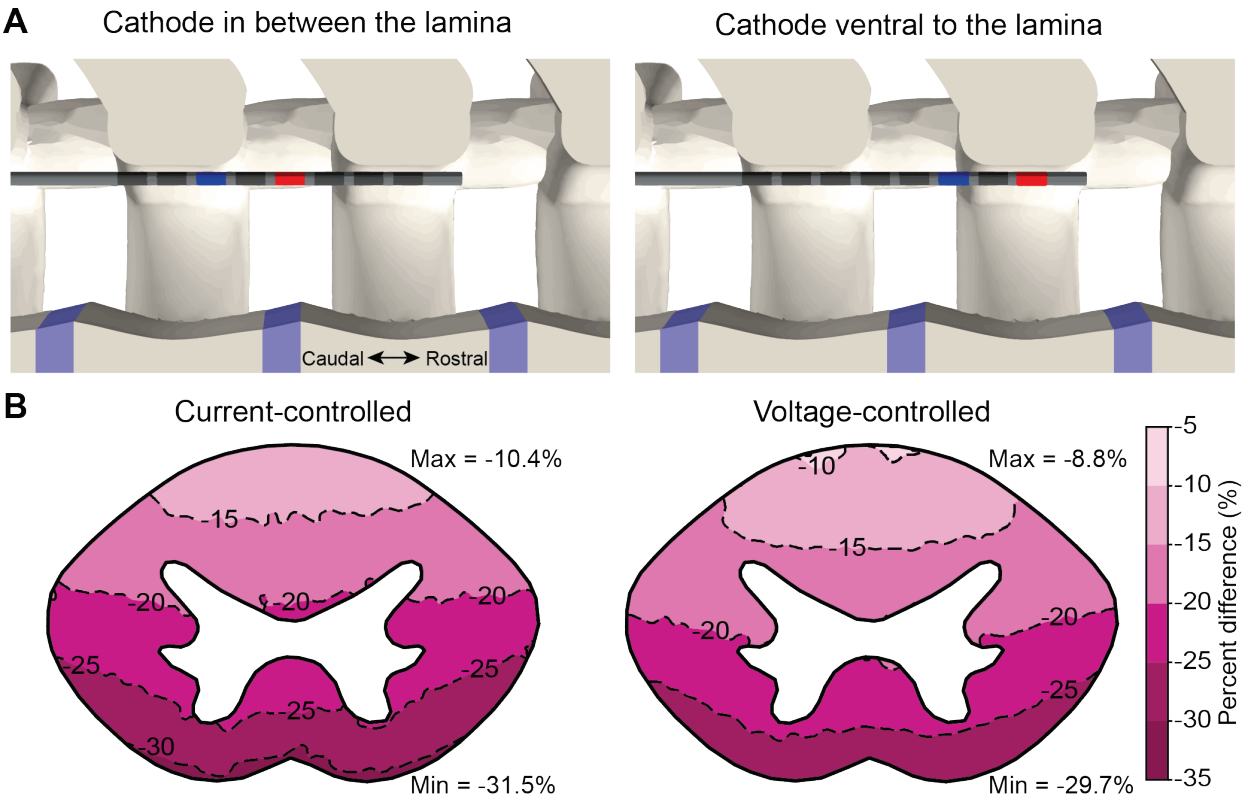


**Figure 2.4**: Effect of electrode position with respect to the bone. A) The 'base' model (left), has the cathode positioned in between the two adjacent laminae (spinal cord not shown). We also evaluated the model with the cathode positioned directly ventral to a lamina (right). B) Percent difference in activation threshold between these two models for CC and VC stimulation.

In addition to the percutaneous lead, we evaluated the predicted thresholds for a paddle style electrode array. For the paddle lead, we compared activation thresholds when the cathode was placed between two successive laminae relative to when the cathode was placed directly ventral to a lamina. For both cathode positions, the minimum activation thresholds were 0.9 mA and 1.1 V for CC and VC stimulation, respectively. For the paddle lead, the different lead positions produced percent differences in activation thresholds of -10.5 to 1.4% and -10.4 to 1.3% for CC and VC stimulation, respectively (**Table 2.2**; Cathode position relative to vertebrae (paddle)). The average percent differences were largest at the ventral aspect of the spinal cord (**Figure 2.5C**).

We calculated activation thresholds for a FEM with the percutaneous electrode and a simplified uniform cylindrical bone domain that has been used in previous SCS modeling studies [43], [90],

[102], [137]. Relative to the base model, this simplified model produced percent errors in activation thresholds of -17.9 to -7.2% and -16.8 to -6.2% for CC and VC stimulation, respectively (**Table 2.2**; Vertebrae vs. cylindrical bone domain).

We examined the significance of explicitly representing the anatomy and electrical properties of the dorsal rootlets within the FEM. With regards to the activation of axons within the spinal cord, removing the rootlet structures from the FEM only produced percent errors of -1.5 – 2.7% and -1.8 – 2.9% for CC and VC stimulation, respectively (**Table 2.2**). Similarly, with regards to the activation of DR fibers, removing the anatomical rootlet structures from the FEM, only produced percent errors of -1.8 to 1.4% and -1.9 to 1.5% for CC and VC, respectively (**Table 2.2**; Rootlets in the FEM). Furthermore, only minor changes were observed in the location of action potential initiation.

We also examined the significance of the dura conductivity within the FEM. Activation thresholds were higher for a dura conductivity of 0.03 S/m relative to the base model with a dura conductivity of 0.6 S/m. Minimum thresholds were 2.6 mA and 2.2 V for CC and VC stimulation, respectively. The overall percent differences between the models ranged from -2.3 to 61.3% for CC stimulation and from -6.7 to 57.4% for VC stimulation (**Figure 2.6**). The largest difference between the models was on the dorsal surface of the spinal cord.

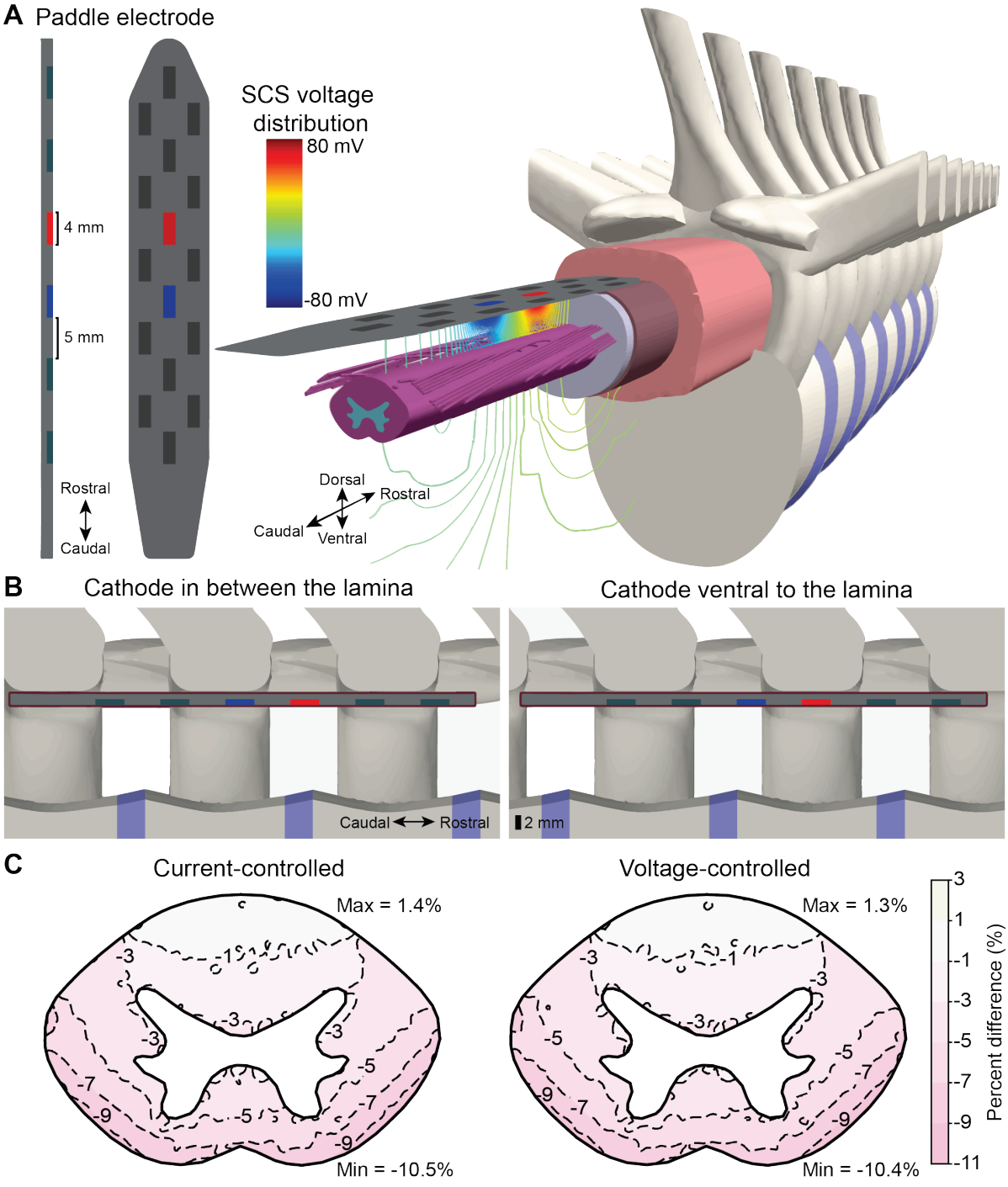


**Figure 2.5**: Effect of electrode position using a paddle electrode with respect to the vertebrae. A) The paddle lead and isopotential lines generated by 1 V bipolar stimulation. B) We positioned the lead with the cathode in between the lamina (left) or ventral to the lamina (right). C) The average percent difference in activation threshold for CC and VC stimulation.

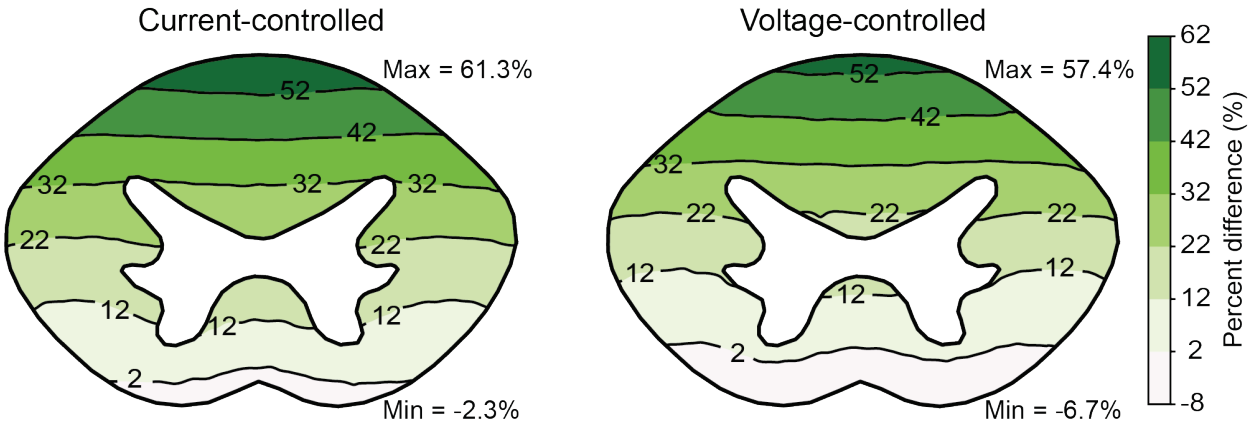


**Figure 2.6**: Effect of dura conductivity. Percent differences in activation thresholds between models with a dura conductivity of 0.6 S/m (base model) and 0.03 S/m for both CC and VC stimulation.

### *2.4.3 Frequency-dependent electrical tissue properties*

To examine the impact of frequency-dependent tissue properties on neural activation during kilohertz-frequency SCS, we used a Fourier FEM approach to calculate the spatiotemporal voltage distributions and the corresponding activation thresholds throughout the spinal cord during 10 kHz SCS [143]. The frequency-dependent solution produced extracellular voltages with temporal profiles that contained rounded lead and trailing edges due to tissue capacitance that resembled results from a previous modeling study (**Figure 2.7B**) [144]. During 10 kHz SCS, the minimum threshold to produce activation in the frequency-dependent model was 6.1 mA, while the frequency-independent model had a minimum threshold of 5.9 mA. The percent errors for all fibers ranged from -3.2 to 7.0% (**Table 2.2**). We observed the largest percent errors near the center of the spinal cord and only small percent errors near the superficial borders of the spinal cord (**Figure 2.7C**). Simulations for the dorsal rootlet fibers produced a similar trend.

The minimum threshold for activation of these fibers was 8.0 mA in the frequency-dependent model and 7.9 mA in the frequency-independent model. For the dorsal rootlet fibers, the percent error between the two models ranged from -4.3 – 8.2% with an average error of 1.5% (**Table 2.2**; Frequency-dependent vs. Frequency-independent).

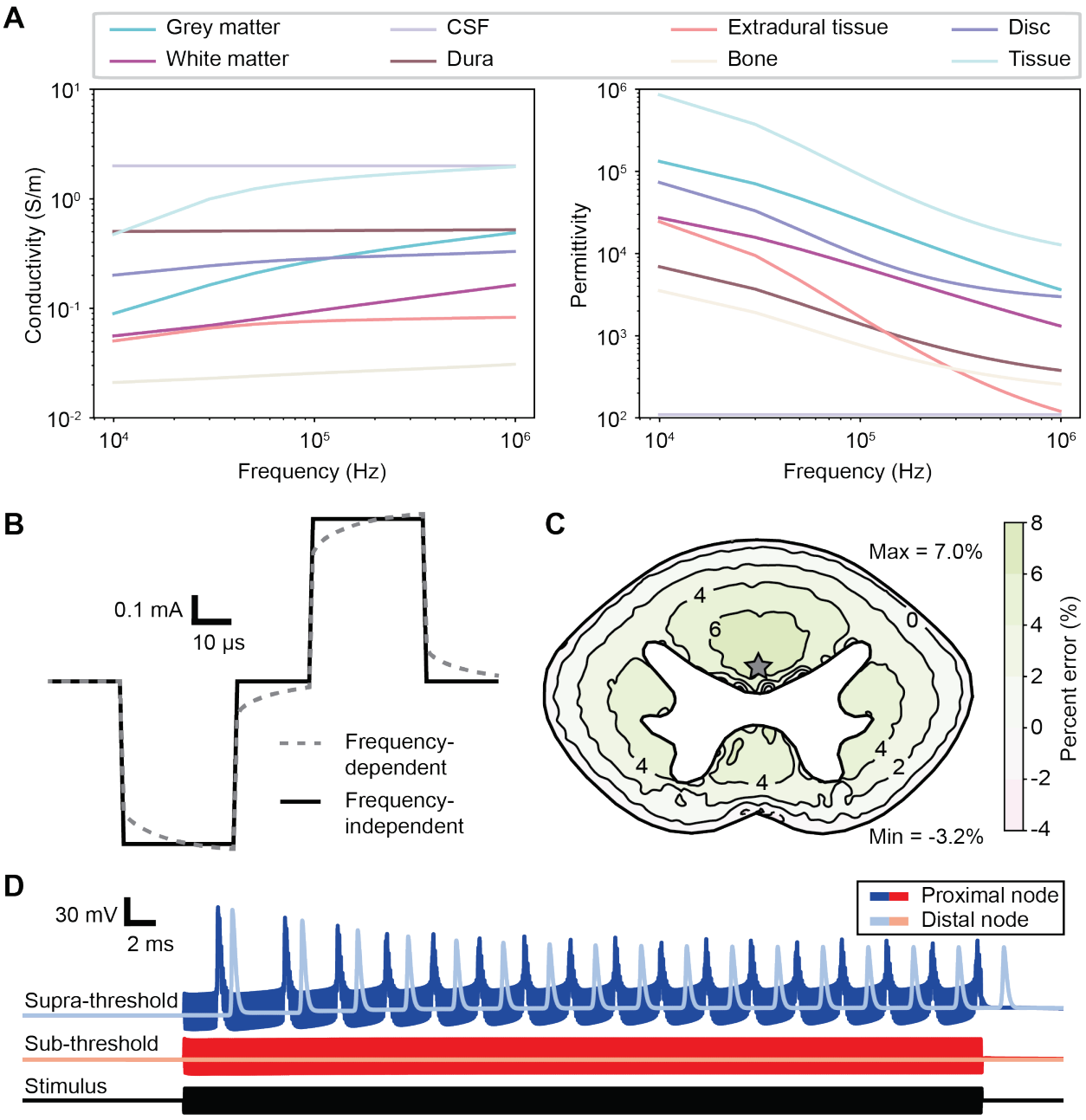


**Figure 2.7**: The frequency dependent tissue solution using the Fourier FEM approach. A) Conductivity and permittivity values for the various tissues were determined using Cole-Cole equations [147]. We assigned the encapsulation domain a permittivity of zero and a conductivity of 0.11 S/m. B) Comparison of the extracellular tissue voltages calculated with the frequency-independent and frequency-dependent models for 1 cycle of the 10 kHz stimulus. C) Percent errors in activation thresholds calculated with the frequency-independent solution relative to the frequency-dependent solution. The gray star near the middle of the spinal cord represents the location of the extracellular voltages shown in B. D) Axonal membrane voltage in response to supra-threshold and sub-threshold stimulation at a proximal (near the electrode) and a distal (away from the electrode) node of Ranvier. An axon was considered activated if it continued to generate action potentials throughout the 50 ms stimulation period.

## 2.5 Discussion

In this study, we performed computational analysis of SCS under a variety of model conditions to examine how several anatomical and technical factors affected predictions of the neural response to SCS. We developed volume conductor models of the implanted electrodes, spinal cord, and other surrounding tissues. We incorporated various details within these volume conductor models, such as realistic spine and spinal cord anatomy, multiple SCS lead types, and frequency-dependent electrical tissue properties. For each set of model conditions, we coupled the corresponding FEM solutions to multicompartment cable models of sensory axons within the dorsal rootlets and spinal cord to predict the activation thresholds. To investigate which anatomical factors significantly affected the neural response to SCS, we calculated the percent difference or percent error in the activation thresholds predicted for each individual axon.

### *2.5.1 Electrode impedance*

To improve neural targeting, SCS arrays typically include a large number of electrodes (i.e., 8-32) [2]. Large variations in electrode impedance can be observed across these electrodes within the same array and/or across patients [12]. This impedance variability across electrodes can affect the extracellular voltages generated within the spinal cord and necessitate frequent adjustment of the stimulation parameters to optimize efficacy [103]. Therefore, we used our model-based approach to assess the effects of clinically relevant differences in electrode impedance on the neural response to SCS. Commercial SCS systems utilize either CC or VC stimulation, so we considered both types of stimulation in our analysis (**Figure 2.3**) [2]. We observed a significant difference in activation thresholds predicted between low- and high-impedance conditions for VC but not for CC stimulation (**Figure 2.3C**, **Table 2.2**). For the high-impedance condition, the encapsulation tissue surrounding the electrodes had a lower conductivity

(i.e., 0.07 S/m vs. 0.25 S/m for the low-impedance condition). For VC stimulation, this lower encapsulation layer conductivity resulted in a lower average peak AF (i.e., 49.4% decrease for high impedance vs. low impedance) with little change in the shape of the AF (data not shown). Therefore, for the high-impedance VC conditions, increased activation thresholds were mainly due to the larger voltage drop across the encapsulation layer and corresponding lower peak extracellular voltages and AF generated along the axons. However, because CC stimulation regulates the electrode current, CC stimulation for high and low impedances produced higher and lower mean extracellular voltages along the axons, respectively, with little changes in the peak voltage differences and the AF (i.e., 0.2% difference in the average peak AF for high-impedance vs. low-impedance conditions). Therefore, our modeling results resemble experimental observations [149] and support the concept that CC stimulation should significantly reduce the consequences of impedance variability observed in clinical SCS.

### *2.5.2 Electrode position relative to vertebrae*

The spine has a complex 3D anatomy. Previous theoretical and experimental studies have shown that the recording amplitude of compound action potentials evoked during SCS was affected by the position of the recording electrodes relative to the 3D spine anatomy [105], [136]. Therefore, we used our model-based approach to investigate how electrode position relative to the spine affected activation thresholds during SCS. For a percutaneous-style lead, our model results suggested that cathode placement ventral to the lamina lowered activation thresholds relative to cathode placement between two successive vertebrae (**Figure 2.4**, **Table 2.2**). Percutaneous leads contain annular electrodes. Therefore, when the cathode was positioned next to a lamina, the low conductivity of the bone relative to the other surrounding tissues directed more current towards the spinal cord and produced lower activation thresholds. We analyzed the difference between the

models using the AF [123], [124]. With the cathode placed directly ventral to the lamina versus between two successive laminae, we observed higher extracellular voltages along the axons and increases in the peak of the AF (i.e., 10.9% and 8.4% at the dorsal spinal cord and 33.9% and 30.9% at the ventral spinal cord for CC and VC stimulation, respectively) with only small changes to the shape of the AF (data not shown). The consistent increase in the peak AF reflected the lower activation thresholds required for all conditions with the cathode placed directly ventral to the lamina versus between two laminae. However, the larger percent increases in the peak AF at the ventral surface, reflected the larger decreases in activation thresholds observed at the ventral surface relative to the dorsal surface of the spinal cord (**Figure 2.4B**).

We performed the same analysis for paddle leads that are also widely used in SCS. One potential advantage of paddles leads is that the electrodes are only exposed on the ventral aspect of the lead body and help focus stimulation towards the spinal cord [150]. This lead design largely reduced changes in activation thresholds due to cathode placement especially for axons located in the dorsal spinal cord which would likely have the lowest threshold to SCS (**Figure 2.5**, **Table 2.2**). As described above for the percutaneous SCS lead, we observed the largest decreases in activation threshold at the ventral surface for both CC and VC stimulation due to differences in the peak AF.

### *2.5.3 Dura mater*

The dura is a fibrous membrane and the outermost layer of the meninges surrounding the CSF and spinal cord. Due to the largely unknown electrical conductivity of the dural membrane [139], we evaluated two dura conductivities (i.e., 0.03 S/m and 0.6 S/m) commonly used in computational models of SCS. For both models, we adjusted the conductivity of the encapsulation layer domain so that average model impedances matched average clinical electrode impedances.

The model with the lower dura conductivity (i.e., 0.03 S/m) had significantly higher thresholds when compared to the base model (i.e., 0.6 S/m) for both CC and VC stimulation on the dorsal surface of the cord. The lower dura conductivity resulted in a large decrease in the peak of the AF (i.e., 51.7 and 54.9% for CC and VC, respectively) with only a small change in shape of the AF (data not shown). These results demonstrate that the choice of dura conductivity can have a significant effect on model-based predictions, even after matching the overall electrode impedance.

These results illustrate a potential limitation in model-based analysis of SCS. The electrical properties of tissue local to the stimulating electrodes determine the direction and magnitude of the current flow generated during SCS. Therefore, the quantitative results from the FEM are related to the conductivity of the dura mater and other local tissues. Because the electrical properties of the dura are largely unknown, the assumed conductivity will affect model predictions. Computational models of neurostimulation are particularly well suited to describe qualitative trends in the neural response to stimulation as a function of specific parameters (e.g., stimulation configuration, pulse width). However, due to uncertainty associated with model parameters, such as tissue conductivities, model accuracy is limited with regards to absolute thresholds. As SCS systems continue to become more sophisticated with increased electrode counts and multiple waveform paradigms, it will become more challenging to use traditional clinical programming methods to exhaustively search the enormous parameter space to determine the optimal stimulation settings. Therefore, accuracy will play a critical role if these computational models are to help increase personalization of SCS technologies. In this case, additional experimental work is needed to ensure the accuracy of computational models of SCS.

*2.5.4 Frequency-dependent tissue properties*

Biological tissues have frequency-dependent electrical properties that may affect the 3D voltage distributions generated during SCS [147]. To reduce computational demands, these frequency-dependent properties are typically ignored in computational modeling studies of SCS and other neuromodulation therapies [43], [151]. This assumption has been justified by previous studies showing that capacitive effects can largely be ignored for standard neurostimulation pulse widths and frequencies [144], [145]. However, novel forms of SCS apply stimulation pulses at much higher pulse frequencies, such as 10 kHz, which may affect the validity of this assumption [40], [152]. Therefore, we used a Fourier FEM approach to consider the effects of frequency-dependent volume conduction during 10 kHz SCS [143]. The frequency-dependent conductivities and permittivities produced modest changes in the activation thresholds. The frequency-independent solution only produced errors of -3 to 7% relative to the frequency-dependent solution (**Figure 2.7C**, **Table 2.2**). The largest percent errors occurred for axons located near the center of the dorsal columns due to tissue filtering effects. Percent errors were lower near the periphery of the spinal cord due to the largely frequency-independent conductivity and permittivity of CSF within the relevant frequency range. This result suggests that, even at pulse frequencies in the 10 kHz frequency range, tissue capacitance has a small effect on volume conduction during SCS.

*2.5.5 Model reductions*

*Spine anatomy*. To reduce computational demands, SCS models often represent the complex 3D structure of the vertebral column with a simplified cylindrical domain or tube [43], [90], [102]. We considered the errors in activation thresholds predicted with a simplified bone domain relative to our base model with the cathode placed between two laminae in a realistic 3D spine anatomy. The simplified spine geometry produced modest errors in the activation thresholds

(**Table 2.2**) and suggests that the 3D spine anatomy may need to be considered for specific conditions.

*Dorsal rootlet anatomy*. Computational models of SCS typically do not include an explicit representation of the anatomy and electrical properties of the dorsal roots or rootlets within the finite element mesh [9], [43], [90], [92], [111]. This simplification is equivalent to directly placing sections of the multicompartment models of DR fibers within the CSF domain and the more ventral aspects within the white matter of the spinal cord. However, in reality, DR fibers project rostrally along the spinal cord with several rootlets entering the spinal cord at each level [107]–[109], [153]. These rootlets have a different conductivity relative to CSF and their presence may affect the 3D voltage distribution generated during SCS. Therefore, this method produces an artificial discontinuity in the extracellular conductivity surrounding these model fibers and potential inaccuracies in the predicted 3D voltage distributions generated during SCS. Previous modeling studies have demonstrated that DR fiber activation typically occurs at the node of Ranvier closest to this artificial discontinuity between the CSF and the spinal cord [154]. Therefore, we performed model analysis to investigate if the rootlet anatomy affected either the activation thresholds or the site of action potential initiation. Within the same finite element mesh, we performed simulations with and without explicit representation of the dorsal rootlet anatomy by altering the conductivity of the rootlets to match either white matter or CSF. Inclusion of the dorsal rootlets within the FEM only produced small errors in the activation thresholds for the DR and spinal cord fibers (**Table 2.2**). We also observed only minor differences in the site of action potential initiation in the DR fibers (data not shown). These results suggest that the anatomy of the DR fibers can largely be ignored in the FEM design. However, it is important to note that our model was designed to study SCS at lower thoracic spinal levels and rootlet structure varies at different spinal levels. For

example, at the cervical or the lumbar spinal levels, the dorsal roots are much denser and larger, which could affect activation thresholds and/or the site of action potential initiation [155], [156]. Therefore, it may be important to consider the dorsal rootlet anatomy in computational models at other spinal cord levels.

### *2.5.6 Limitations*

While the modeling in this work was derived from standard computational practices, there were still several potential limitations. One of the main limitations was that no ground truth currently exists, so we used our most detailed model as our standard for model comparisons. In our spinal cord model, we uniformly positioned the sensory axons throughout the white matter. In reality, the spinal cord consists of heterogeneous fiber diameters and densities throughout the spinal cord [14]. However, our fiber size densities were based on histological data of the superficial dorsal columns which contain the large-diameter myelinated axons that most likely have the lowest thresholds to SCS [14], [15]. Another potential limitation of our model is that we separated our dorsal rootlets into five unique rootlets that did not combine to form a larger root, as is seen anatomically. However, we designed our model to match descriptions of the dorsal root entry zone available in the literature [108]–[110], [157] because this zone is the site of activation for rootlets close to the stimulating electrodes. Due to its relevance in clinical SCS [16], [158], [159], we focused our analyses on a simple bipolar stimulation configuration. It is not clear if the results of this study can be extended to monopolar or multipolar stimulation configurations and these stimulation configurations should be considered in future studies. It would also be important to consider additional physiological effects of SCS. For example, because 10 kHz SCS is typically applied at sub-sensory amplitudes, it is unlikely to directly activate dorsal column axons and several additional physiological mechanisms have been proposed (e.g., depolarization block,

desynchronization, membrane integration, tissue heating) [36], [43], [160]–[164]. Finally, to limit the number of parameters and corresponding model iterations required in this study, we did not investigate several factors that have been considered in previous computational modeling studies that have been shown to affect model-based activation thresholds, such as dorsal CSF thickness, dorsoventral position of the stimulating electrode, position of the spinal cord within the dural sac, the influence of collateral branching on dorsal column thresholds, and dorsal root threshold with respect to electrode location [43], [86]–[88], [93], [99], [111], [137], [140], [165]–[167].

## 2.6 Conclusions

In this study, we utilized a computational modeling approach to investigate how several anatomical and technical factors affected the predicted neural response to thoracic level SCS. Our results suggest that anatomical variables, such as the position of the active electrodes relative to the spine, can significantly change activation thresholds to SCS. Variability in electrode impedance, can significantly affect the stimulation amplitudes required to produce neural activation with voltage-controlled, but not current-controlled, stimulation. To simplify computational demands, our results also suggest that it is possible to ignore anatomical features, such as the dorsal rootlets, without producing significant errors in model predictions. Our results also demonstrate that the choice of dura conductivity can have a significant influence on model-based predictions. Therefore, this study highlights several issues that should be considered during clinical implementation of SCS and in future computational modeling studies investigating the physiological and technical factors affecting the neural response to SCS.

# Chapter 3: Model-based Optimization of Spinal Cord Stimulation for Inspiratory Muscle Activation

Part of the material for this chapter has been adapted with modifications from the following publication:

1. **H. J. Zander** *et al.*, "Model-based optimization of spinal cord stimulation for inspiratory muscle activation", *Neuromodulation: Technology at the Neural Interface (2021).* doi: 10.1111/ner.13415 [168]

## 3.1 Abstract

*Objective*

High-frequency spinal cord stimulation (HF-SCS) is a potential method to provide natural and effective inspiratory muscle pacing in patients with ventilator-dependent spinal cord injuries. Experimental data has demonstrated that HF-SCS elicits physiological activation of the diaphragm and inspiratory intercostal muscles via spinal cord pathways. However, the activation thresholds, extent of activation, and optimal electrode configurations (i.e., lead separation, contact spacing, and contact length) to activate these neural elements remain unknown. Therefore, the goal of this study was to use a computational modeling approach to investigate the direct effects of HF-SCS on the spinal cord and to optimize electrode design and stimulation parameters.

*Materials and Methods*

We developed a computer model of HF-SCS that consisted of two main components: 1) finite element models of the electric field generated during HF-SCS, and 2) multicompartment cable models of axons and motoneurons within the spinal cord. We systematically evaluated the neural recruitment during HF-SCS for several unique electrode designs and stimulation configurations to optimize activation of these neural elements. We then evaluated our predictions by testing two of these lead designs with *in vivo* canine experiments.

*Results*

Our model results suggested that within physiological stimulation amplitudes, HF-SCS activates both axons in the ventrolateral funiculi (VLF) and inspiratory intercostal motoneurons. We used our model to predict a lead design to maximize HF-SCS activation of these neural targets. We evaluated this lead design via *in vivo* experiments, and our computational model predictions demonstrated excellent agreement with our experimental testing.

*Conclusions*

Our computational modeling and experimental results support the potential advantages of a lead design with longer contacts and larger edge-to-edge contact spacing to maximize inspiratory muscle activation during HF-SCS at the T2 spinal level. While these results need to be further validated in future studies, we believe the results of this study will help improve the efficacy of HF-SCS technologies for inspiratory muscle pacing.

## 3.2 Introduction

Patients with a severe cervical spinal cord injury sustain a devastating injury that often results in respiratory failure requiring long-term mechanical ventilation for survival in some patients [52], [56]. Of the nearly 13,000 patients admitted for spinal cord injuries in 2019, over 300 patients still required a mechanical ventilator one-year post spinal cord injury [56].

An injury to the high cervical spinal cord can sever the bulbospinal pathways, which connect the respiratory center in the medulla to both the diaphragm and intercostal motoneuron pools, yet segmental neural circuitry and reflexes below the site of injury often remain intact [7], [54]. While the neural connections from the brain to these motoneuron pools are lost, the motoneuron pools can still be activated and recruited through segmental reflex pathways below the level of injury or through the use of electrical stimulation [7], [73], [74].

High-frequency (>300 Hz) spinal cord stimulation (HF-SCS) of the upper thoracic spinal cord is a novel stimulation technique shown to produce naturalistic inspiratory activity in both the inspiratory intercostal muscles and diaphragm of C2-spinalized canines [7], [11], [68]–[70], [96]. It's been hypothesized that this stimulation applied by electrodes in the ventral epidural space activates fibers associated with the intercostal-to-phrenic reflex pathway, which facilitates diaphragm activation in response to activation in the lower thoracic cord [59], [73], [74], [169]. However, it is unknown if the stimulation amplitudes utilized in HF-SCS (i.e., 4-6 mA) would produce direct activation of the fibers in this reflex pathway that are located within the ventrolateral funiculus (VLF) of the spinal cord [7]. Likewise, it is also unclear to what degree HF-SCS activates the inspiratory intercostal muscles by the recruitment of motoneurons near the stimulating electrodes.

Therefore, the goal of this study was to utilize computational models and experimental testing to investigate HF-SCS recruitment of two target populations: 1) axons in the VLF

associated with the intercostal-to-phrenic reflex pathway, and 2) motoneurons innervating the inspiratory intercostal muscles. We evaluated HF-SCS recruitment with various lead designs and stimulation configurations. We then tested two of these lead designs via *in vivo* canine experiments. Our theoretical and experimental results suggest that within physiological stimulation amplitudes, HF-SCS activates axons in the VLF and inspiratory intercostal motoneurons within the T2-T4 spinal cord. Furthermore, our results suggest maximal inspiratory activity is produced with monopolar, bipolar, or tripolar stimulation configurations applied with wire electrode leads with longer contacts (e.g., 6 mm length) and larger edge-to-edge contact spacing (e.g., 12 mm). The results of our study will assist in the development of electrode designs to achieve optimal HF-SCS for inspiratory muscle pacing.

## 3.3 Methods

### *3.3.1 Computational model*

*Finite element model.* We developed a volume conductor model with dimensions that mimicked the canine model in our experimental studies. Our anatomical finite element model (FEM) consisted of the spinal cord, cerebrospinal fluid (CSF), dura, epidural space, vertebrae, intervertebral discs, and a surrounding bulk tissue (**Figure 3.1A**). We determined the canine geometry of the vertebral column and white and gray matter boundaries from experimental measurements and literature [170]–[174]. The spinal cord was ovular, with dimensions of 6.0 x 7.7 mm [171]. The cord was surrounded by CSF and dura mater with a thickness of 0.3 mm, as well as nine identical and anatomically accurate vertebrae with intervertebral discs representing the vertebral column [97], [170]–[174]. We then created multiple lead designs that we positioned

in the epidural tissue on the ventral side of the spinal cord. To mimic experimental conditions, we placed the return electrode in the bulk tissue domain dorsal and lateral to the vertebral column.

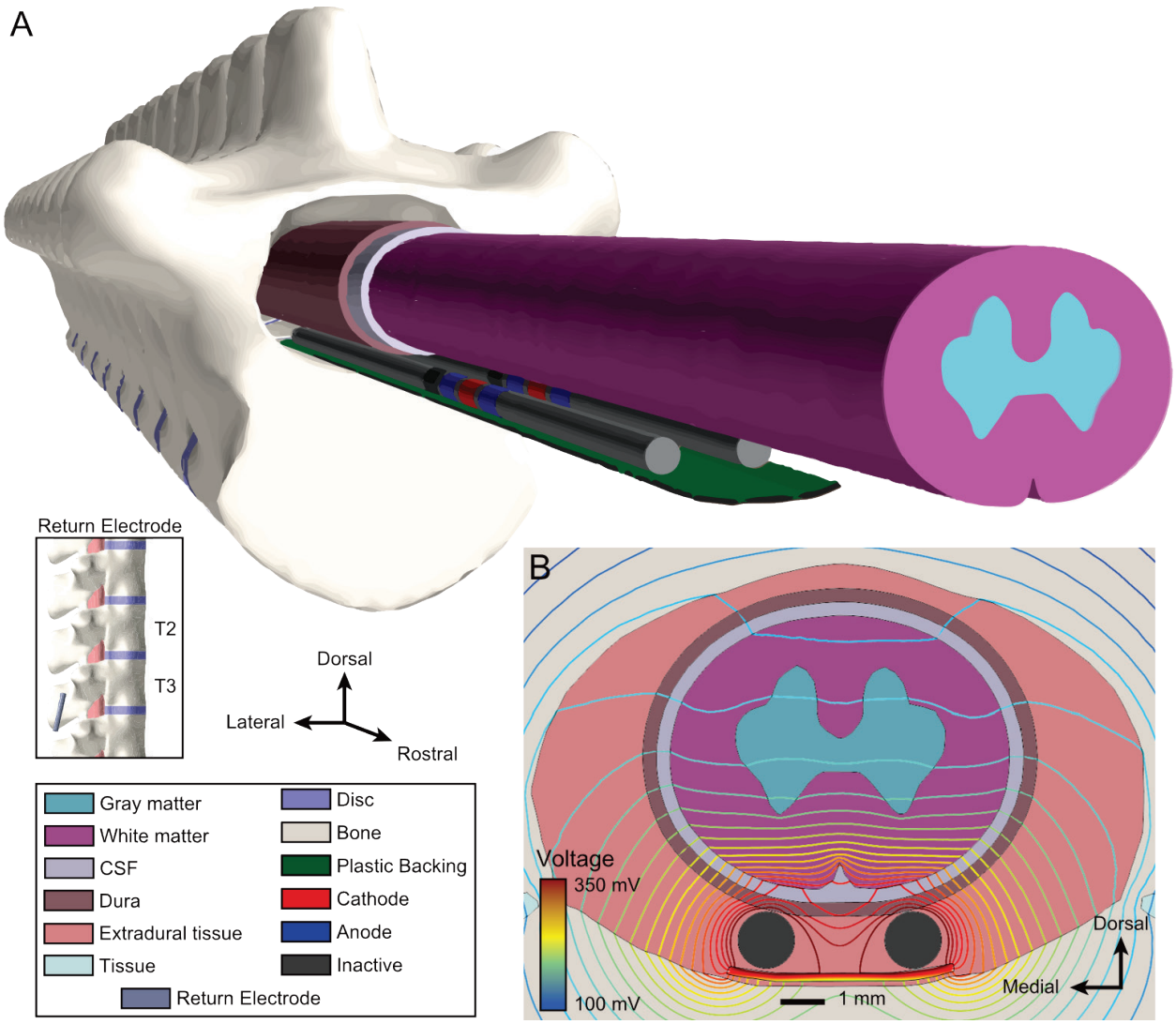


**Figure 3.1**: Finite element model (FEM) of high-frequency spinal cord stimulation (HF-SCS). (A) Exploded isometric view of the canine-specific FEM. The FEM included explicit representation of the spinal cord, CSF, dura, two four-contact percutaneous HF-SCS leads, vertebral column, intervertebral discs, and the general thorax. The return electrode was positioned in the back musculature between the transverse process and spinal processes (see inset). (B) Contour plot of the voltages generated throughout the spinal cord and surrounding anatomy in response to monopolar (1 mA) stimulation applied through two adjacent electrodes.

Based on previous experimental work, each lead configuration consisted of two parallel percutaneous wire leads (1.25 mm diameter) with four electrode contacts in the rostrocaudal

direction. We evaluated three main geometrical lead parameters: mediolateral spacing between the electrode arrays (lead separation), contact length, and contact spacing (edge-to-edge distance between adjacent contacts on an individual lead array).

Following surface generation of the various tissues and electrodes, we discretized our FEM into tetrahedral elements using 3-matic (Materialise NV, Belgium) with higher node densities near the contacts. We imported our mesh into COMSOL Multiphysics (COMSOL Inc., USA) and defined electrical conductivities for each tissue type using data from the literature (**Table 3.1**). We applied a Neumann boundary condition of a unit current stimulus (1 A) to our stimulation electrodes, while inactive electrodes were modeled as equipotential with zero net current across their surface. We applied a Dirichlet boundary condition of 0 V at the return electrode. We calculated electrostatic FEM solutions with an iterative equation solver using the conjugate gradient method. For each possible active electrode, we repeated FEM calculations of the voltage distribution generated by a unit stimulus applied at that individual electrode. We used superposition to calculate the overall voltage distributions generated by bipolar or tripolar stimulation.

**Table 3.1**: Electrical conductivities used in the finite element model.

| Tissue | Conductivity (S/m) | Reference |
|---|---|---|
| Gray matter | 0.230 | [120] |
| White matter (longitudinal) | 0.600 | [120] |
| White matter (transverse) | 0.083 | [120] |
| Cerebrospinal fluid | 1.700 | [120] |
| Dura mater | 0.600 | [43] |
| Extradural tissue | 0.250 | [92] |
| Vertebral bone | 0.020 | [121], [147] |
| Intervertebral disc | 0.650 | [92] |
| General thorax | 0.250 | [120] |

*Neuron models.* In this study, we used the software package, NEURON, to evaluate the direct effects of HF-SCS on the axonal pathways within the VLF and on local motoneurons [133]. To simulate HF-SCS induced activation of ascending fibers that can produce phrenic activation, we defined multi-compartment axon models ascending within the ventral half of our canine spinal cord (**Figure 3.2C**). We based these axon models on a previously published double-cable axon model with finite myelin impedance (**Figure 3.2A**) [127]. Based on previous studies, each axon had a diameter of 10 μm and a corresponding conduction velocity of 57 m/s [74], [175]. VLF fibers were distributed throughout the ventral half of the spinal cord to evaluate thresholds throughout the ventral and lateral funiculi (**Figure 3.2C**). We positioned a total of 156 axons in the ventral half of the spinal cord, with 82 fibers in the lateral funiculi.

Previous work demonstrates that ventral HF-SCS at the T2 spinal level could activate upper thoracic inspiratory motoneurons, which predominantly produce inspiratory behavior [7], [60]. We therefore modeled intercostal motoneurons throughout the T1-T6 spinal cord (**Figure 3.2E**). We adapted our motoneuron models from the work by Greiner et al., which contain a multicompartment soma, dendritic tree, axon initial segment, and a myelinated axon (**Figure 3.2B**) [6], [10]. We scaled the soma and axon diameters to match measurements from previous feline studies (50.0 μm and 3.6 μm, respectively) [176]. For each motoneuron pool (T1-T6), ten motoneuron cell bodies spanned both the spinal segment as well as the caudal half of the rostrally adjacent segment [177]–[179]. Each motoneuron axon exited the spinal cord, then moved caudally through the CSF and the dura and merged with other axons from the same spinal level, before exiting through the intraforaminal space (**Figure 3.2E**) [180].

*Neural recruitment by HF-SCS.* We assessed the direct neural response to HF-SCS by applying the extracellular voltages calculated in the FEM to the neuron models. We interpolated

the scaled extracellular voltages onto the model axons and neurons described above and used a bisection algorithm (error < 1%) to calculate the activation threshold for each axon and neuron. We defined the activation threshold as the minimum stimulation amplitude necessary to generate one or more action potentials in a particular axon or motoneuron. For each set of model parameters, we calculated the activation threshold for each model axon and neuron in response to 200 μs rectangular stimulus pulses applied at a rate of 300 Hz. At stimulation amplitudes just above the neural threshold, neural activity consisted of a short initial transient period of activity in response to the initial stimulus pulses. However, this amplitude of stimulation did not generate sustained neuron activation throughout the duration of the pulse train. Slightly higher stimulus amplitudes were required to produce sustained activation when compared to activation in response to a single stimulus pulse. Therefore, to calculate the sustained activation thresholds for each axon or motoneuron, we applied 40 consecutive pulses and only evaluated activation during the last 20 pulses of the stimulus train. Because our past experimental work has demonstrated that a pulse frequency of 300 Hz produces the optimal recruitment of inspiratory muscles, we only considered this optimal pulse frequency of 300 Hz in our model analysis [7], [11], [68]–[70], [96]. For each lead design, we calculated the activation thresholds for bilateral stimulation using monopolar, bipolar, and tripolar stimulation configurations. In all configurations, the stimulation electrode (cathode) was the second contact from the top (red electrodes in **Figure 3.3A**). For bipolar stimulation, the anode was positioned as the third contact from the top of each lead (bottom blue electrodes in **Figure 3.3A**) For tripolar stimulation, the anodes were the first and third contacts (blue electrodes in **Figure 3.3A**).

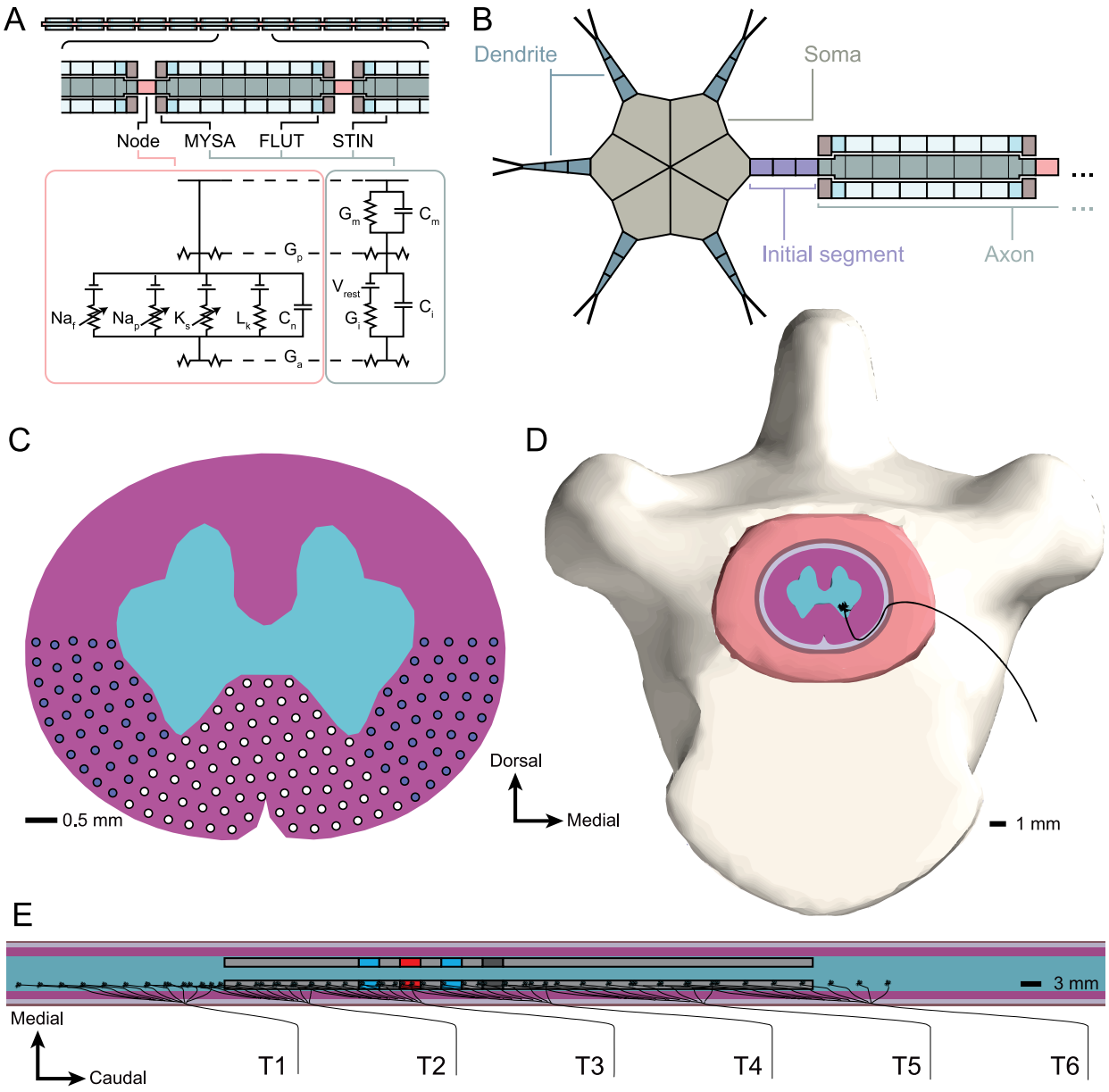


**Figure 3.2**: Multicompartment models of axons and intercostal motoneurons in the upper thoracic spinal cord. (A) We represented ascending spinal cord axons using a previously published multicompartment cable model of a myelinated axon [127]. (B) We generated motoneuron models that included a multi-tap soma, dendritic arborizations, an initial segment consisting of three compartments, and a myelinated axon [10], [181]. (C) We distributed ascending fibers (10 µm diameter) within the white matter of the cord throughout the ventral (white circles) and the ventrolateral funiculi (blue circles) to determine the activation thresholds of these axons. (D) We positioned the cell body of our motoneuron models within the ventral horn of the gray matter. Axons then traveled through the white matter, CSF, dura, and epidural space before entering the bulk tissue surrounding the cord. (E) Positions and trajectories of the motoneurons within the spinal cord, and their relationship to two leads with 3 mm long contacts and an edge-to-edge contact spacing of 3 mm.

*Model investigations.* We tested three primary variables in our computational models: mediolateral lead separation between the two parallel wire leads, electrode contact length, and

rostrocaudal edge-to-edge electrode contact spacing (**Table 3.2**). To examine the effect of each variable on the neural recruitment during HF-SCS, we calculated the activation thresholds for VLF fibers and motoneurons for each parameter set.

*Mediolateral lead separation*. As described above, we examined HF-SCS applied via two parallel four-contact electrode arrays. The lead separation was the lateral distance between the axial midlines of the two leads. Due to the limited size of the backing to the electrodes, we calculated activation thresholds for lead separations of 0.0, 1.0, 1.5, 2.0, and 3.0 mm.

*Contact length*. We considered the effects of contact size on the neural recruitment during HF-SCS by examining different contact lengths. We calculated the activation thresholds for contacts with lengths of 3 and 6 mm.

*Rostrocaudal contact spacing*. We also considered the effects of rostrocaudal spacing between individual contacts. For contacts with a length of 3 mm, we calculated the activation thresholds for edge-to-edge spacings between individual electrodes of 1, 3, and 6 mm. For contacts with a length of 6 mm, we calculated the activation thresholds for edge-to-edge spacings of 1, 3, 6, 9, and 12 mm.

**Table 3.2**: List of parameters for each group of simulations.

Lead separation (mediolateral) (**Figure 3.3**)

| | |
|---|---|
| **Lead separation** | **0.0, 1.0, 1.5, 2.0, and 3.0 mm** |
| Contact length | 6.0 mm |
| Contact spacings | 12.0 mm |
| Neural targets | VLF axons and motoneurons |
| Stimulation configurations | Monopolar, bipolar, and tripolar |

Contact length (**Figure 3.4**)

| | |
|---|---|
| **Contact lengths** | **3.0 and 6.0 mm** |
| Contact spacing | 3.0 mm |
| Lead separation | 2.0 mm |
| Neural targets | VLF axons and motoneurons |
| Stimulation configurations | Monopolar, bipolar, and tripolar |

Contact spacing (edge-to-edge) (**Figure 3.5**)

| | |
|---|---|
| **Contact spacings** | **3.0 mm contacts: 1.0, 3.0, and 6.0 mm**<br>**6.0 mm contacts: 1.0, 3.0, 6.0, 9.0, and 12.0 mm** |
| Contact lengths | 3.0 mm and 6.0 mm |
| Lead separation | 2.0 mm |
| Neural targets | VLF axons and motoneurons |
| Stimulation configurations | Monopolar, bipolar, and tripolar |

Stimulation configurations (**Figure 3.3**, **Figure 3.4**, **Figure 3.5**)

| | |
|---|---|
| **Stimulation configurations** | **Monopolar, bipolar, and tripolar** |
| Contact lengths | 3.0 mm and 6.0 mm |
| Lead separation | 0.0, 1.0, 1.5, 2.0, and 3.0 mm |
| Neural targets | VLF axons and motoneurons |
| Contact spacings | 3.0 mm contacts: 1.0, 3.0, and 6.0 mm<br>6.0 mm contacts: 1.0, 3.0, 6.0, 9.0, and 12.0 mm |

The free parameters are indicated in bold. VLF = ventrolateral funiculus.

### *3.3.2 Experimental testing*

Based on the model predictions, we evaluated the efficacy of two lead designs (the first design with 3 mm contacts and 3 mm edge-to-edge spacing and the second design with 6 mm contacts and 12 mm edge-to-edge spacing) via *in vivo* canine experiments. Experiments were performed in three adult mongrel male dogs weighing 30.0 – 32.7 kg (mean: 31.4 ± 0.8 kg) under

the approval of the Institutional Animal Care and Use Committees of Case Western Reserve University. Animals were initially anesthetized with pentobarbital sodium (25 mg/kg), given intravenously. We provided additional doses (1–2 mg/kg) as needed. It is important to note that in our unpublished observations we have found that pentobarbital results in no significant changes in inspiratory muscle activation during HF-SCS. Animals were tracheostomized, intubated with a cuffed endotracheal tube (10 mm ID) that was sutured in the trachea in the midcervical region and mechanically ventilated. We placed a catheter in the femoral vein to administer fluids and supplemental anesthesia. We monitored blood pressure and heart rate (Waveline Pro Multi-Function Monitor, DRE, Louisville KY) via a femoral arterial catheter. We maintained the body temperature at 38 ± 0.5°C with a heating blanket (Harvard Apparatus, Holliston, MA). We monitored end-tidal $PCO_2$ at the trachea and oxygen saturation from the earlobe (Waveline Pro Multi-Function Monitor). Tidal volume was measured by electrical integration of the flow signal from a pneumotachograph (Series 3700, Hans Rudolph, Shawnee, KS). For lead placement, we performed a laminectomy at the T4–T5 level and inserted each lead into the ventral epidural space at the midline and advanced the leads to the T2 spinal region. To secure the parallel wire leads in place, we fixed them to an 8 mm wide polyurethane plastic backing.

We used a square-wave pulse stimulator (model S88; Grass Technologies, West Warwick, RI) equipped with a stimulus isolation unit (PSIU6; Grass Technologies) to provide monopolar, bipolar, or tripolar stimulation. We assessed changes in airway pressure generation during ventral SCS at the T2 level over a wide range of stimulus amplitudes and frequencies (0.5–6 mA per electrode lead, 20 – 1,000 Hz). Stimulus train duration was set at 0.8 s since a plateau in pressure generation is generally achieved at this time. Stimulus pulse width was maintained at 0.2 ms. A remote ground electrode was positioned in the back musculature. In all trials, SCS was performed

after hyperventilation-induced apnea. Following temporary separation from the ventilator, airway pressure generation during SCS using a pressure transducer (MP45; Validyne, Northridge, CA) connected to the endotracheal tube, during airway occlusion at functional residual capacity was measured. All recordings were monitored and stored on a computer using a data acquisition and analysis system (Spike 2 with 1401 interface: Cambridge Electronic Design, Cambridge, UK).

*Experimental protocol and data analysis*. In separate trials, we experimentally tested two lead designs within each animal. We tested one lead design with electrode contacts having a length of 3 mm and an edge-to-edge spacing of 3 mm, and a second lead design with electrode contacts having a length of 6 mm and edge-to-edge spacing of 12 mm. Using these two lead designs, we evaluated the generation of airway pressure and the total volume inhaled in response to stimulation using the same three stimulation configurations considered in our computational model analyses: monopolar, bipolar, and tripolar configurations. We performed these measurements over a range of stimulation amplitudes for both lead designs and all three stimulation configurations. Following the convention in the clinical SCS field, we have reported model and experimental stimulation amplitudes as the sum of the total cathodic output (e.g., 1 mA applied at the right cathode and 1 mA applied at the left cathode corresponds to a stimulation amplitude of 2 mA). We applied each stimulation amplitude 2-3 times and reported all experimental data as mean ± standard error of the mean. We performed statistical analysis using a repeated measures analysis of variance and paired t-test. We established statistical significance as a two-sided p-value of $< 0.05$.

## 3.4 Results

### *3.4.1 Computational model predictions*

*Mediolateral lead separation*. We initially used our computational model to test how the distance separating the two parallel HF-SCS lead affected the activation thresholds for the ascending VLF fibers. We calculated activation thresholds for lead separations of 0.0, 1.0, 1.5, 2.0, and 3.0 mm (**Figure 3.3**). For monopolar stimulation, the median activation thresholds for the VLF fibers were 1.44, 1.42, 1.40, 1.39, and 1.39 mA, respectively. Bipolar thresholds were 1.26, 1.25, 1.24, 1.23, and 1.20 mA while tripolar thresholds were 1.27, 1.26, 1.25, 1.23, and 1.22 mA. These results show a small maximum percentage difference (< 5%) in the activation thresholds for the VLF fibers resulting from mediolateral distance between the two leads. Therefore, lead separation did not have a significant effect on HF-SCS recruitment of the VLF fibers. We also evaluated the effect of lead separation on motoneuron thresholds, but as with the VLF fibers, found limited differences in recruitment between the 5 tested lead separations (data not shown).

*Contact length*. In our computational model, we evaluated neural recruitment during HF-SCS as a function of contact length. We calculated the activation thresholds for VLF fibers and T2-T5 motoneurons. We evaluated two contact lengths (3 and 6 mm) on VLF and motoneuron thresholds with an electrode spacing of 3 mm (**Figure 3.4**). For axons within the VLF, the 3 mm contacts had median activation thresholds of 1.22, 1.26, and 1.36 mA for monopolar, bipolar, and tripolar stimulation, respectively (**Figure 3.5B**). The 6 mm contacts had median thresholds of 1.42, 1.29, and 1.30 mA, respectively (**Figure 3.5B**). Therefore, 3 mm contacts activated VLF fibers at lower monopolar amplitudes, while the 6 mm contacts provided more efficient recruitment for tripolar stimulation. However, these differences were small, and corresponded to a mean percentage difference of only 5.7%.

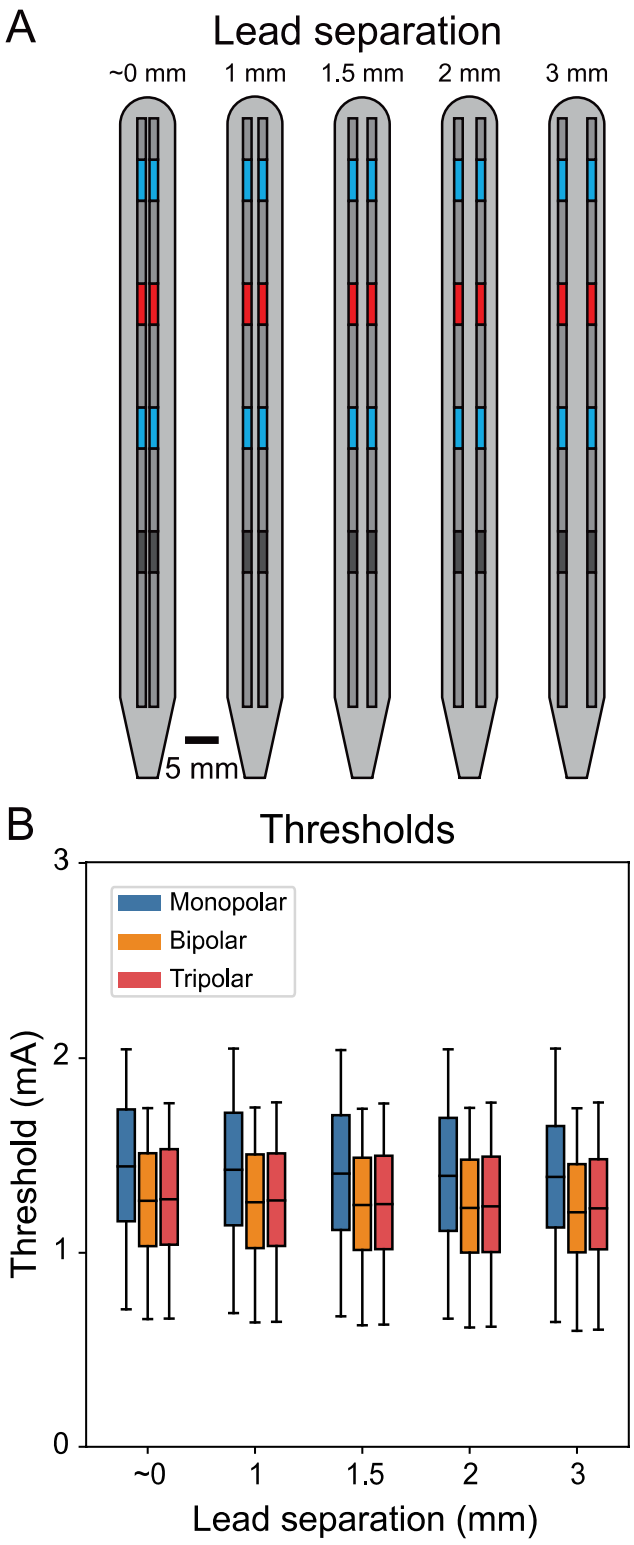


**Figure 3.3**: Effect of mediolateral lead separation on neural recruitment. (A) We performed model analysis for mediolateral lead separations of 0.0, 1.0, 1.5, 2.0 and 3.0 mm (contact length of 6 mm, 12 mm contact spacing). (B) We represented activation thresholds for axons within the VLF for the five lead separations for monopolar, bipolar, and tripolar stimulation using standard box plots. For each box plot, the minimum, 25$^{th}$ percentile, median, 75$^{th}$ percentile, and maximum activation thresholds are represented by the bottom whisker, bottom of the box, black horizontal line, top of the box, and top whisker, respectively.

For monopolar stimulation, activation thresholds of the T2-T5 motoneurons were similar for both contact lengths (mean percentage difference of 14.1%) (**Figure 3.4B**). For bipolar and tripolar stimulation, activation thresholds of T2, T3, and T5 motoneurons were also similar for both contact lengths (mean percentage difference of 7.5% and 3.0% for bipolar and tripolar stimulation, respectively) (**Figure 3.4B**). However, for bipolar and tripolar stimulation, 6 mm contacts recruited up to 20% more T4 motoneurons for a given stimulation amplitude (**Figure 3.4B**). Therefore, relative to the shorter 3 mm contacts, 6 mm contacts not only provided similar recruitment of VLF fibers, but the longer contacts could recruit a larger number of motoneurons at a given stimulation amplitude.

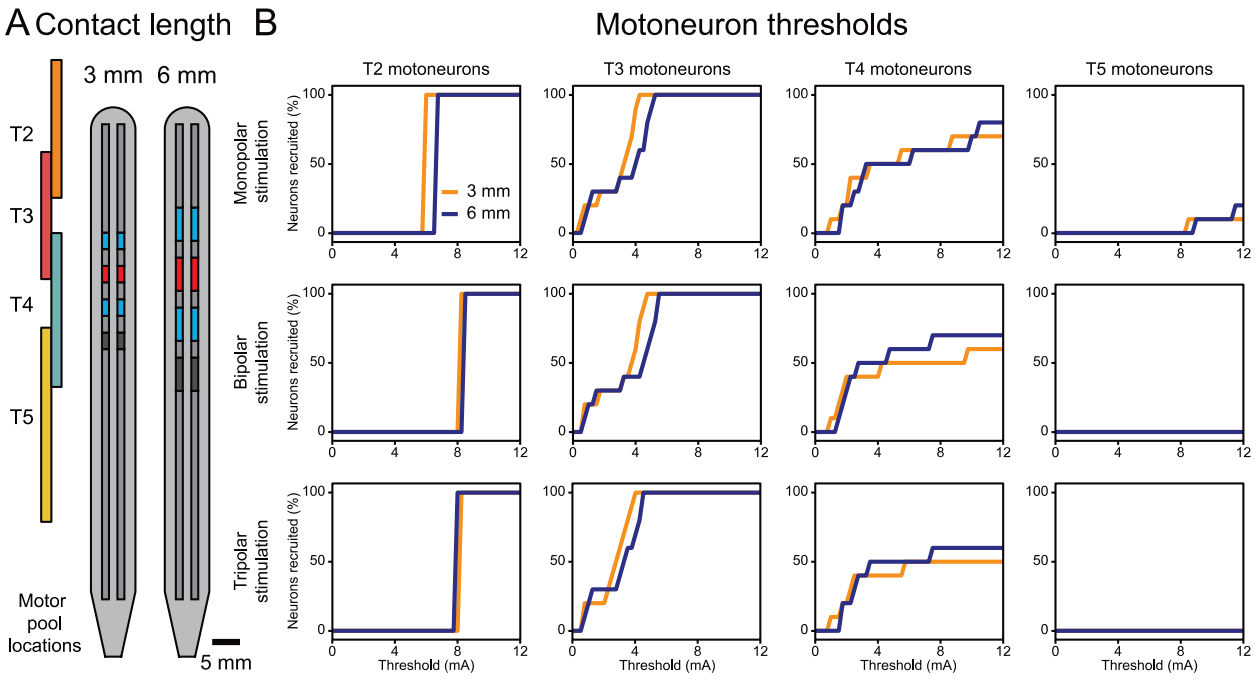


**Figure 3.4**: Effect of contact length on neural recruitment. (A) Positioning of the motoneuron pools (left) compared to two electrode configurations (right) with contact lengths of 3 and 6 mm (3 mm edge-to-edge contact spacing, 2 mm mediolateral lead separation). (B) Motoneuron thresholds for both contact lengths for monopolar, bipolar, and tripolar stimulation configurations.

*Rostrocaudal contact spacing*. The edge-to-edge spacing or vertical distance between adjacent contacts on a given lead had a significant effect on the activation thresholds for both VLF fibers and motoneurons. For axons within the VLF, larger rostrocaudal contact spacing generally produced the lowest activation thresholds (**Figure 3.5B**). For a contact length of 3 mm, tripolar stimulation produced median activation thresholds of 2.36 and 1.06 mA for contact spacings of 1 and 6 mm, respectively. For a contact length of 6 mm, tripolar stimulation produced median activation thresholds of 1.71 and 1.23 mA for contact spacings of 1 and 12 mm, respectively.

Rostrocaudal contact spacing showed similar trends of motoneuron recruitment. As expected, monopolar thresholds for recruitment were similar across all the tested contact spacings (data not shown). However, bipolar and tripolar stimulation showed increased recruitment for large contact spacings (>6 mm) (**Figure 3.5C**). For tripolar stimulation, we measured complete T2 motoneuron recruitment at 10.5, 8.0, 7.0, 6.75, and 6.75 mA for contact spacings of 1, 3, 6, 9, and 12 mm, respectively. Complete recruitment of T4 motoneurons only occurred with contact spacings of 9 or 12 mm (10.0 and 6.75 mA, respectively) (**Figure 3.5C**). Because their axons projected close to the cathode (**Figure 3.2E**), T3 motoneuron recruitment was largely unaffected by contact spacing and complete recruitment occurred below 5.5 mA for all contact spacings (**Figure 3.5C**). In general, these results suggest that larger rostrocaudal spacing or edge-to-edge distance between adjacent contacts should increase the recruitment of axons within the VLF and inspiratory motoneurons.

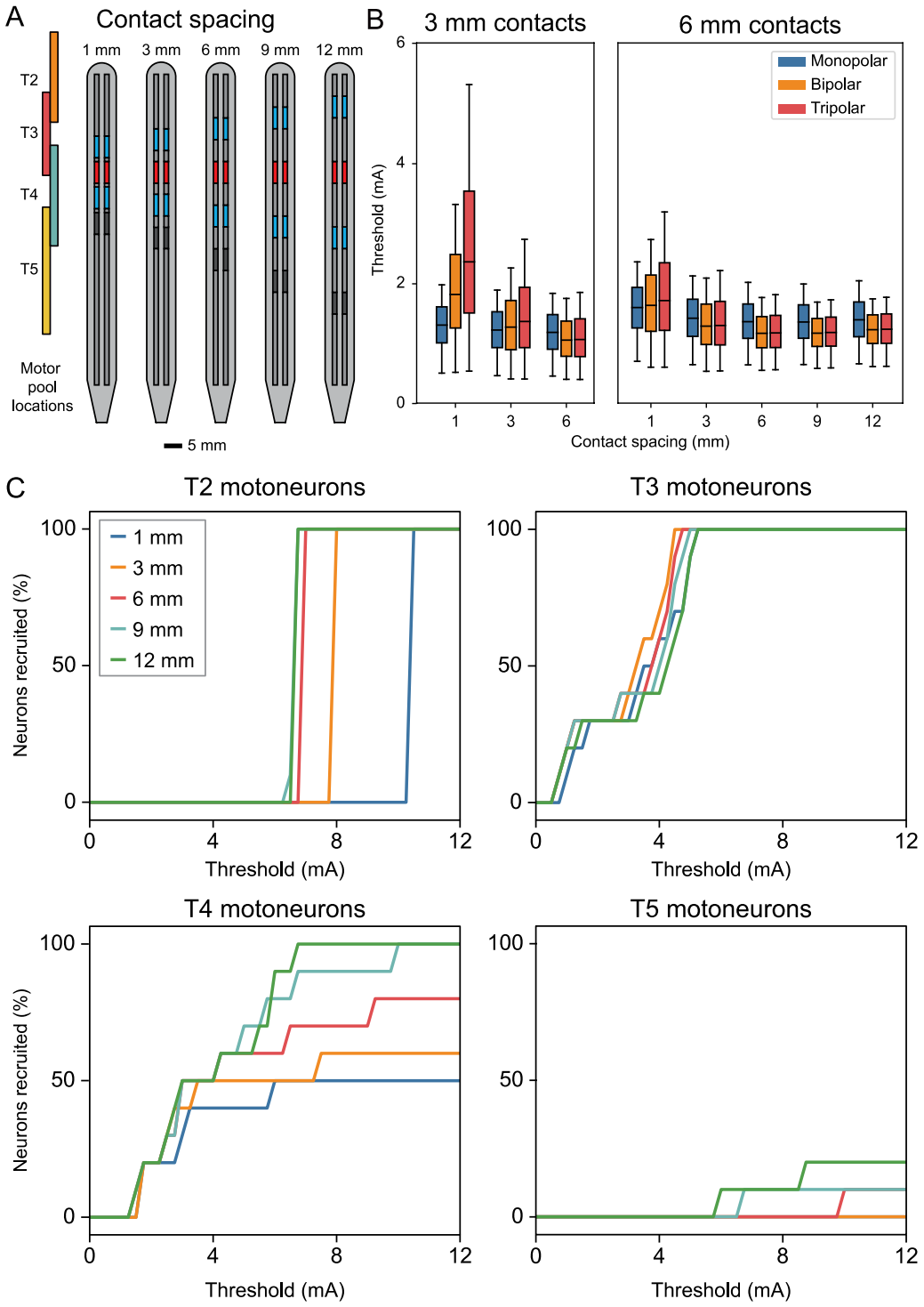


**Figure 3.5**: Effect of rostrocaudal contact spacing on neural recruitment. (A) Locations of the cell bodies of the various relevant motoneuron pools (left) and the various contact spacings tested for the 6 mm contact electrodes (right) (2 mm lead separation). (B) Recruitment of VLF fibers. For a contact length of 3 mm, we evaluated edge-to-edge contact spacings of 1, 3, and 6 mm. For a contact length of 6 mm, we tested edge-to-edge contact spacings of 1, 3, 6, 9, and 12 mm. Due to their common use in clinical devices, we evaluated thresholds for the following stimulation configurations: monopolar, bipolar, and tripolar. Each box plot shows the activation threshold for the first axon, 25, 50, 75, and 100% of VLF fibers. (C) Motoneuron recruitment by spinal level (T2-T5) as a function of contact spacing. These recruitment curves are for tripolar stimulation with 6 mm contacts and 2 mm mediolateral lead separation.

*Optimal lead design.* Based on the model predictions described above, we hypothesized that a lead design with long contacts (6 mm) and large rostrocaudal contact spacing (12 mm) would lead to optimal recruitment of both VLF fibers and motoneurons (**Figure 3.6A**). Therefore, we performed further computational analyses with this type of lead design along with a second suboptimal lead design that had smaller contacts and smaller contact spacings (3 mm contact length, 3 mm contact spacing) (**Figure 3.6A**).

For recruitment of VLF fibers with monopolar stimulation, the lead design with 3 mm contacts produced lower activation thresholds relative to the lead design with 6 mm contacts (mean percent difference of -15.1%) (**Figure 3.6B**). However, the 6 mm lead design produced lower activation thresholds for both bipolar and tripolar stimulation (mean percent difference of 1.5% and 8.2%, respectively) that were similar to the activation thresholds for monopolar stimulation with the 3 mm lead design (**Figure 3.6B**).

For motoneuron recruitment with monopolar stimulation, both lead designs produced similar activation thresholds (mean percent difference of 11.3%) (top row in **Figure 3.6C, D**). However, for a given stimulation amplitude (e.g., 7.5 mA), the 6 mm lead design recruited a higher total percentage of motoneurons relative to the 3 mm lead design for both bipolar (82.5% vs. 37.5% of T2-T5 motoneurons) and tripolar (77.5% vs. 37.5% of T2-T5 motoneurons) stimulation (middle and bottom rows in **Figure 3.6C, D**).

These computational modeling results suggest that monopolar stimulation with either lead design should produce similar recruitment of VLF fibers and inspiratory motoneurons. However, at a given HF-SCS amplitude, the lead design with 6 mm contacts and 12 mm contact spacing should produce improved neural recruitment for bipolar and tripolar stimulation.

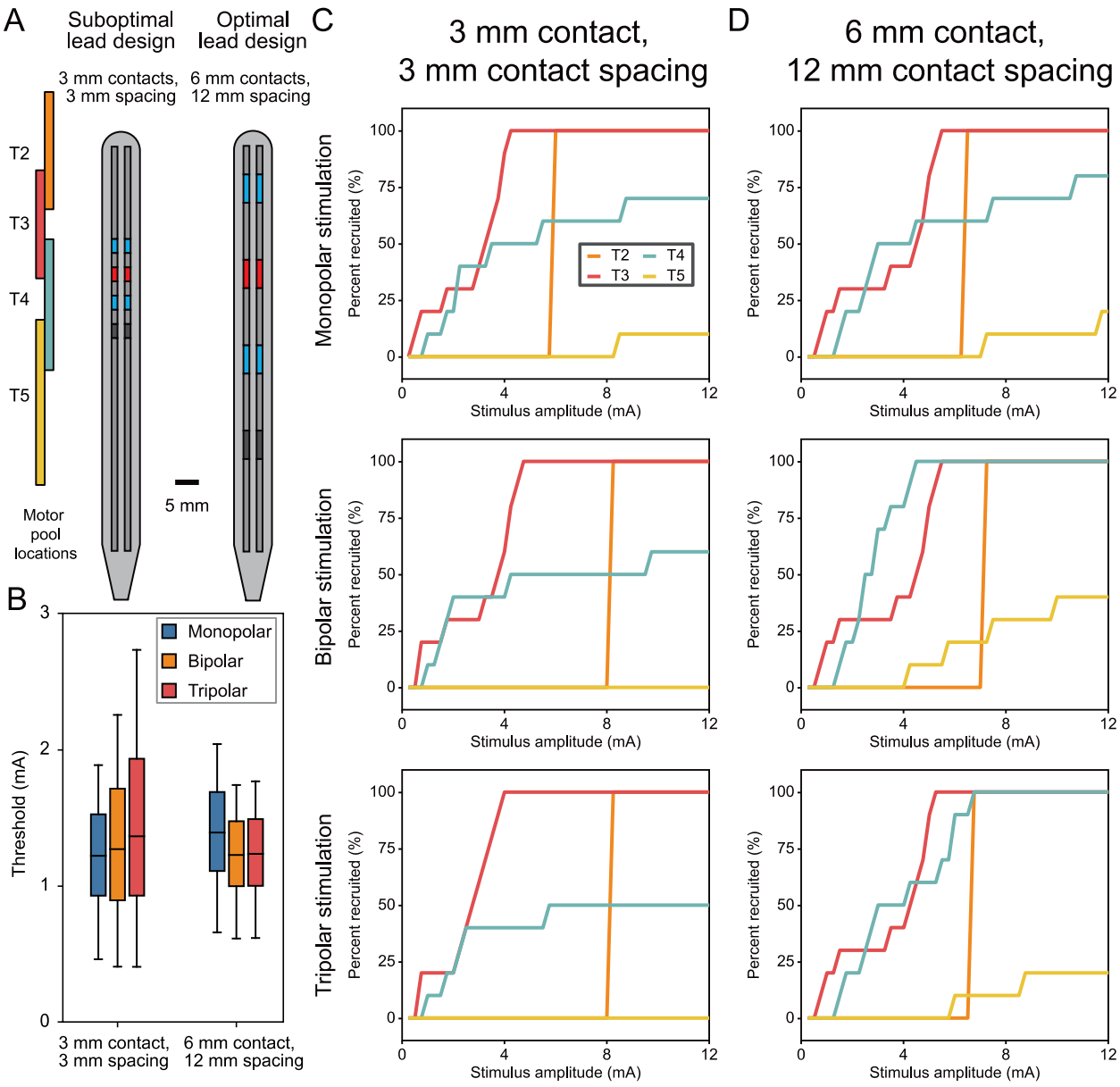


**Figure 3.6**: Neural recruitment for theoretically suboptimal and optimal lead designs. (A) The suboptimal lead configuration had a contact length of 3 mm and rostrocaudal edge-to-edge contact spacing of 3 mm. The optimal lead design had a contact length of 6 mm and rostrocaudal edge-to-edge contact spacing of 12 mm. Both lead designs had a mediolateral lead spacing of 2 mm. (B) Activation thresholds for axons within the VLF for the two lead designs for monopolar, bipolar, and tripolar stimulation. Boxplots represent recruitment of first axon, then 25, 50, 75, and 100% recruitment of VLF fibers. (C) Percentage of motoneurons recruited within each spinal cord segment as a function of stimulation amplitude for monopolar (top row), bipolar (middle row), and tripolar (bottom row) stimulation for the suboptimal lead design. (D) Same as in (C) except for the optimal lead design.

*3.4.2 Experimental testing*

Based on the computational model analyses described in the previous section, we performed *in vivo* canine experiments to evaluate the efficacy of the suboptimal (3 mm contacts and 3 mm contact spacings) and optimal (6 mm contacts and 12 mm contact spacings) lead designs. Mean blood pressure and heart rate remained stable throughout the period of stimulation. The mean spontaneous breathing tidal volume was 301±7 ml with an airway pressure of 17.2±0.4 $cmH_2O$. To evaluate the efficacy of these lead designs in generating inspiratory activity, we assessed changes in airway pressure generation and inspired volume over a wide range of stimulus amplitudes during ventral HF-SCS at the T2 spinal level. Although we tested a wide range of stimulus frequencies, we only reported the results for a pulse frequency of 300 Hz because mean airway pressure and inspired volume were always largest at this pulse frequency in support of our previous work [7], [11], [68]–[70], [96]. Mean negative airway pressure generation and inspired volume over a wide range of HF-SCS amplitudes are presented in **Figure 3.7**. There were progressive increases in the magnitude of airway pressure generation and inspired volume with increasing HF-SCS amplitude from 0 to 4 mA. The maximal inspiratory pressures typically occurred at HF-SCS amplitudes around 4 mA. Mean maximal negative airway pressures (Paw) and inspired volumes are presented in **Table 3.3**. Mean maximal negative airway pressures (Paw) for the suboptimal lead design were 84±6, 64±3, and 58±6 $cmH_2O$ for monopolar, bipolar, and tripolar stimulation, respectively. Mean maximal inspired volumes for the suboptimal lead design were 1239±159, 1182±131, and 1091±103 mL for monopolar, bipolar, and tripolar stimulation, respectively. The maximal inspiratory pressures for the optimal lead were 89±6, 80±2, and 82±10 $cmH_2O$ for monopolar, bipolar, and tripolar stimulation, respectively. Mean maximal inspired

volumes for the optimal lead design were 1316±138, 1283±73, and 1281±140 mL for monopolar, bipolar, and tripolar stimulation, respectively.

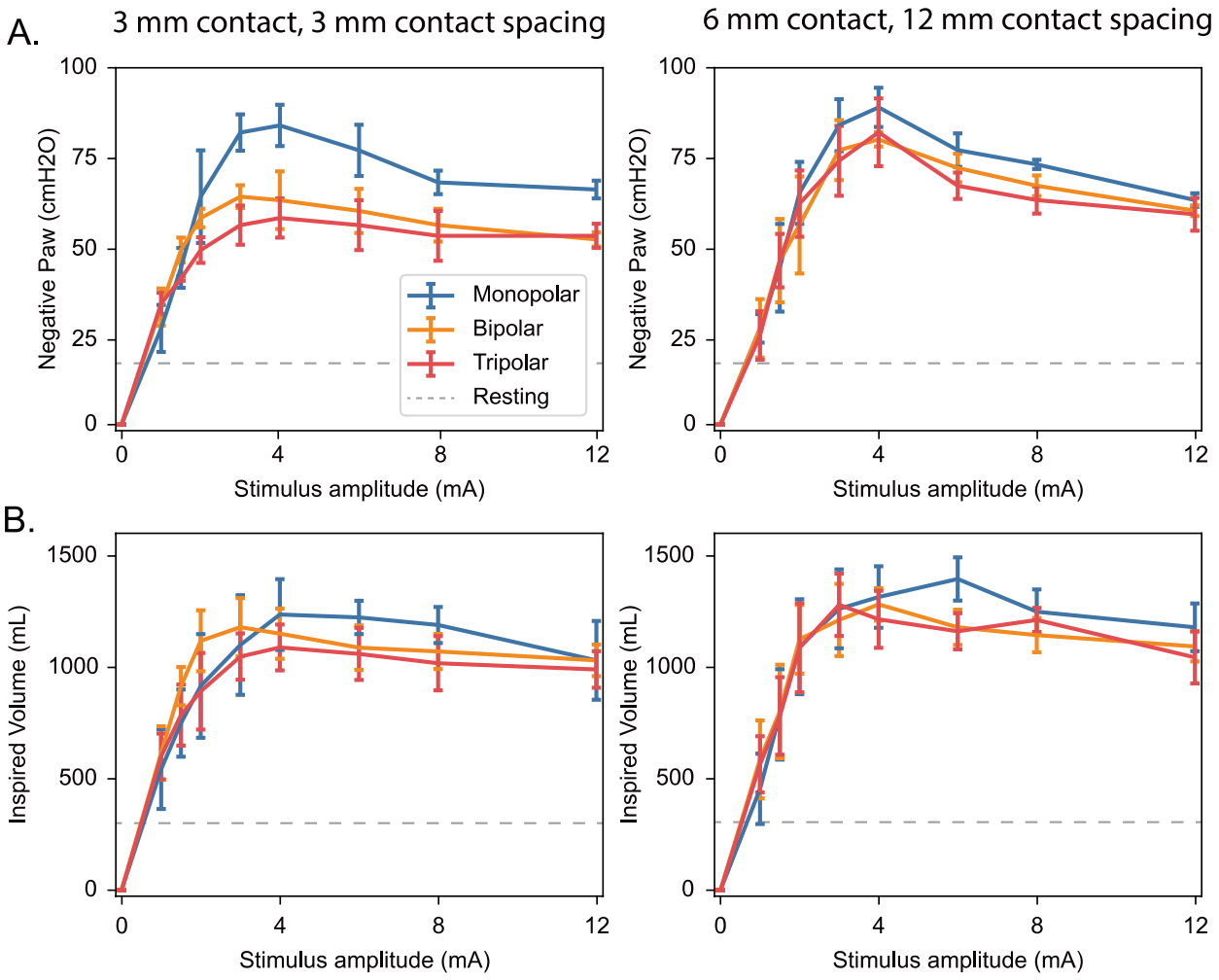


**Figure 3.7**: *In vivo* responses to ventral HF-SCS. Mean changes in (A) airway pressure and (B) inspired volumes as a function of stimulation amplitude for monopolar, bipolar, and tripolar stimulation. The gray dashed lines indicate the mean airway pressure (17.2 ± 0.4 $cmH_2O$, top) and mean spontaneous breathing tidal volume (301 ± 7 ml, bottom). In the left column, HF-SCS was applied via two parallel leads with contact lengths of 3 mm and rostrocaudal contact spacings of 3 mm. In the right plots, HF-SCS was applied via two parallel leads with contact lengths of 6 mm and rostrocaudal contact spacings of 12 mm. The reported amplitude represents the total current from both electrode arrays (e.g., 12 mA total current equates to 6 mA per cathode).

**Table 3.3**: In vivo maximal inspiratory pressures for the two lead designs.

| Lead design / Stimulation configuration | Maximal Negative Paw (cmH2O) | | | Inspired Volume (mL) | | |
|---|---|---|---|---|---|---|
| | Monopolar | Bipolar | Tripolar | Monopolar | Bipolar | Tripolar |
| 3 mm contact, 3 mm spacing | 84 ± 6 | 64 ± 3* | 58 ± 6* | 1239 ± 159 | 1182 ± 131 | 1091 ± 103* |
| 6 mm contact, 12 mm spacing | 89 ± 6 | 80 ± 2** | 82 ± 10** | 1316 ± 138 | 1283 ± 73 | 1281 ± 140 |

*P < 0.05 compared to monopolar stimulation configuration. **P<0.05 between the two lead designs for the given stimulation configuration.

## 3.5 Discussion

This study represents the first computational modeling analysis to assess which neural elements are directly activated by upper thoracic HF-SCS to restore inspiration and to optimize lead design. Furthermore, we tested our predictions in an animal model of HF-SCS. We believe that this approach provides significant insight into the mechanisms in which HF-SCS activates inspiratory muscles and provides information to optimize the stimulation parameters and electrode design.

### *3.5.1 The mechanisms of spinal cord stimulation for inspiration*

The theoretical and experimental findings of this study provide insight into the mechanisms of action of ventral HF-SCS to activate the inspiratory muscles. The model-based thresholds for axons in the VLF and the upper thoracic motoneurons were within the therapeutic range of canine experiments of SCS for inspiration. In a canine model, experimental measures of inspiratory pressure in response to 300 Hz stimulation using parallel wire leads (6 mm contacts, 12 mm gaps) begin to build at amplitudes as low as 0.5 mA. The maximal inspiratory pressure appears to peak at around 4-6 mA of total current [7]. While strong diaphragm recruitment is vital for inspiratory pressure generation, concurrent activation with the inspiratory intercostals has previously been

shown to result in changes in inspiratory pressures greater than the sum of either individual muscle group [182]. Therefore, activation of only one muscle group, such as the diaphragm, results in limited inspiratory pressures [72], [182]. Based on our modeling results, stimulation as low as 2 mA resulted in near complete VLF activation for monopolar, bipolar, or tripolar stimulation with a sufficiently large contact spacing (>6 mm) (**Figure 3.4B**). However, for motoneurons with the optimal stimulation configuration (6 mm contact length, 12 mm contact spacing), 2 mA of stimulation recruited only 20% of T3 and 30% of T4 motoneurons, with no activation in either T2 or T5 motoneurons (**Figure 3.6D**). But at higher stimulation amplitudes, such as 7 mA monopolar stimulation, we predicted complete activation of T2 and T3 motoneurons, and recruitment of 60% of T4 motoneurons (**Figure 3.6D**). Bipolar and tripolar stimulation resulted in even stronger recruitment of T4 motoneurons, and even showed recruitment of T5 motoneuron (**Figure 3.5D, Figure 3.6D**). The predicted higher motoneuron activation thresholds may partly explain why peak inspiratory pressures are measured at 4-6 mA *in vivo*. The increased and broader recruitment of motoneurons at these higher amplitudes could aid diaphragm activation to produce large inspiratory pressures. Future studies will be needed to better quantify, validate, and confirm this effect.

### *3.5.2 Theoretical optimal lead design*

We evaluated how three electrode design parameters affected the activation of VLF fibers and motoneurons. These model electrode configurations mimicked the design parameters that we evaluated in our *in vivo* experiments. We initially evaluated the effect of the mediolateral lead spacing or separation between the two parallel electrode arrays. Due to the finite size of the electrode backing, the maximum allowable separation between the percutaneous leads was 3 mm. Our analysis showed a minimum in threshold with a 3 mm separation, although the differences in

threshold when compared to the 1.5 mm or 2 mm lateral separations were minor (<3% difference in median VLF thresholds) (**Figure 3.3**).

Contact length had a small effect on activation thresholds. With regards to axons within the VLF, shorter 3 mm contacts could lead to slightly lower thresholds for monopolar stimulation relative to longer 6 mm contacts. However, for bipolar and tripolar stimulation, the shorter contacts required significantly higher stimulation amplitudes to activate VLF fibers (**Figure 3.5B**). The 3 mm and 6 mm contacts produced small differences in motoneuron recruitment, especially for monopolar stimulation (**Figure 3.4B**). However, at a given stimulation amplitude, the short 3 mm contacts did recruit a smaller percentage of caudal T4 motoneurons for bipolar and tripolar stimulation (**Figure 3.4B**) that may reduce the efficacy of these shorter contacts in restoring inspiration.

The rostrocaudal edge-to-edge spacing between individual contacts had a large effect on stimulation thresholds, particularly for bipolar and tripolar stimulation. Large contact spacings (>6 mm) resulted in the lowest median activation thresholds for activation of axons within the VLF, especially for bipolar and tripolar stimulation (**Figure 3.5B**). Furthermore, large rostrocaudal separation between individual contacts typically recruited the largest number of motoneurons, including rostral and caudal motoneurons, for a given stimulation amplitude (**Figure 3.5C**). We obtained the maximum motoneuron recruitment for a lead design with contacts with a length of 6 mm and an edge-to-edge spacing of 12 mm.

Stimulation configuration had a large effect on the activation thresholds for both VLF fibers and motoneurons. For small rostrocaudal spacing between individual contacts (1-3 mm), monopolar stimulation resulted in the lowest activation thresholds for both VLF fibers and motoneurons relative to bipolar and tripolar stimulation (**Figure 3.5B, Figure 3.6C**). However,

for large contact spacings (>6 mm), bipolar and tripolar stimulation produced lower activation thresholds for VLF fibers (**Figure 3.5B, Figure 3.6B**) and recruited a larger percentage of more caudal motoneurons from the T4 and T5 levels (middle and bottom rows in **Figure 3.6C-D**).

Therefore, our computational modeling results suggest that the ideal lead design would have longer contacts with larger edge-to-edge spacing between individual contacts. This result is not obvious as previous modeling work of spinal cord stimulation for pain demonstrated non-monotonic relationships between design parameters, such as contact length and contact spacing, and neural recruitment as a function of stimulation amplitude [99], [100]. This previous modeling work along with our work within the context of HF-SCS for inspiration, demonstrate that an optimal electrode size, spacing, and stimulation configuration can be found that produce the three-dimensional electric fields that optimize neural recruitment. As described above, past experimental evidence suggests that concurrent activation of axons within the VLF and upper thoracic motoneurons leads to maximum inspiratory pressure [7], [182]. Therefore, a lead design with longer contacts and larger rostrocaudal contact spacing theoretically provides the best ability to activate VLF fibers and recruit a large number of motoneurons, especially from more caudal spinal levels.

### *3.5.3 In vivo testing*

We then performed experimental measurements to assess the potential efficacy of our theoretical-optimal lead design relative to a suboptimal lead design. Model predictions for these two lead designs are shown in **Figure 3.6** and the corresponding experimental measurements of airway pressure and inspired volumes are shown in **Figure 3.7**. In general, our *in vivo* results were in excellent agreement with our computational model predictions.

For the suboptimal lead design (3 mm contact length, 3 mm contact spacing), our computational model predicted that monopolar stimulation would activate the largest percentage of both VLF fibers and motoneurons relative to bipolar or tripolar stimulation (**Figure 3.6B-C**). The *in vivo* results show a similar trend to the model predictions, with peak inspiratory pressures of 84 ± 5.8, 64 ± 3.2, 58 ± 5.5 cmH2O, for monopolar, bipolar, and tripolar, respectively (**Figure 3.7, Table 3.3**).

For the theoretical-optimal lead design (6 mm contact length, 12 mm contact spacing), our computational model predicted that bipolar stimulation would lead to the lowest thresholds for VLF fibers and broad recruitment of both nearby (T2) and more caudal (T3-T5) motoneurons (**Figure 3.6B, D**). However, our *in vivo* data showed no statistically significant differences in HF-SCS-induced inspiratory pressures or inspired volumes between monopolar, bipolar, or tripolar stimulation with this lead design (**Figure 3.7, Table 3.3**). A lack of significant differences could be due to the small number of animals that we considered in this study.

However, our computational model predictions and experimental results did agree when comparing the two lead designs. First, our computational model predicted similar monopolar thresholds between the two lead designs. This prediction agreed with the experimental measurements in which both lead designs produced similar changes in airway pressure and inspired volumes (**Figure 3.7, Table 3.3**). For bipolar and tripolar stimulation, our computational model predicted that the optimal lead design would activate a larger number of both VLF fibers and motoneurons (**Figure 3.6**). This prediction agreed with our *in vivo* data in which we detected statistically significant higher peak inspiratory pressures generated during bipolar and tripolar stimulation with the optimal lead design relative to the suboptimal lead design (**Table 3.3**). Therefore, our computational modeling and experimental results largely support the potential

advantages of a lead design with longer contacts and larger edge-to-edge contact spacing to improve inspiratory activity generated during ventral HF-SCS.

The main neural targets we modeled in this study, the VLF fibers and upper thoracic motoneurons, are thought to lead to downstream activation of both the diaphragm and the inspiratory intercostal muscles [7], [11], [59], [60], [72]. Our experimental measurements have demonstrated that the diaphragm and inspiratory intercostals contribute ~47 and ~53%, respectively, of the total inspiratory pressures in response to HF-SCS [70]. This result is different than spontaneous breathing in which the inspiratory intercostals are only responsible for ~31% of the tidal volume [70]. Our current work highlights that HF-SCS at the T2 level can lead to strong recruitment of VLF fibers and activation of motoneurons at the thoracic interspaces with the largest inspiratory contributions [60].

*3.5.4 Study limitations*

Although our data demonstrated a strong agreement between model predictions and experimental testing, our study had several potential limitations. One potential limitation was that our computational model did not consider the downstream effects of HF-SCS on the neural circuits responsible for inspiration. This limitation did not allow our model to capture the significant differences in motor output as function of pulse frequency that have been demonstrated in our previous work [68]. Higher frequencies (>200 Hz) result in greater inspiratory pressures and volumes at lower stimulation amplitudes that is likely a result of summation of excitatory post-synaptic potentials (EPSPs) in higher-order neurons in the inspiratory pathways [67], [68]. To better characterize indirect effects of stimulation additional post-synaptic neural elements are required to evaluate how these EPSP's lead to both phrenic motoneuron activation as well as post-synaptic inspiratory intercostal activation [67]. While it is known from the literature that these

pathways do exist as reflex arcs, the synaptic layout and details of the connections between VLF and the phrenic motoneurons remains unknown. More research will be needed to fully describe these structures [11], [59], [73], [169].

To improve model predictions, these network effects can be incorporated into future model analyses following methods utilized in other computational modeling studies of SCS [9], [67], [181]. Furthermore, we did not consider additional neural elements, such as afferent fibers and interneurons making direct synaptic connections onto the intercostal motoneurons, that could also play a role in HF-SCS-induced inspiration [60]. In this initial modeling study, we focused our attention on the likely first-order neural targets of ventral HF-SCS. VLF fibers are large, myelinated axons positioned only a few millimeters away from the electrode and are therefore likely to be recruited during ventral HF-SCS. Likewise, the ventral trajectory of motoneurons also make them likely to be activated by stimulation. Incoming afferents and interneurons, in comparison, are much more dorsal relative to the VLF or the motoneurons and thus less likely to be directly activated by ventral HF-SCS. Furthermore, it is important to recognize that while some studies have evaluated the morphology of thoracic spinal interneurons, there are many unknowns regarding the connections, morphology, ion channels, and functional role they play in modulating respiratory motoneurons [175]. Future studies will be invaluable to provide the information necessary to build the next generation of computational models for optimizing ventral HF-SCS to restore inspiration.

With regards to the experimental measurements, it is important to consider secondary effects of the stimulation. It is possible that the HF-SCS could produce unwanted side effects, such as the activation of limb muscles. While we have observed these effects in past experiments that require high stimulation amplitudes, these effects were minimal during HF-SCS at 300 Hz at low

stimulus amplitudes. Additionally, as in previous studies, we observed stable heart rates and blood pressures in response to HF-SCS [7]. Finally, it could be hypothesized that stimulation may trigger activity of brainstem respiratory centers which lead to inspiratory muscle activation. However, our previous investigations have demonstrated that brainstem respiratory centers are not involved in the observed responses to HF-SCS [71].

### 3.6 Conclusions

This study represents the first attempt to employ a computational modeling approach to investigate the mechanisms of HF-SCS to activate the inspiratory muscles and to optimize lead design to best target spinal respiratory neurons. In general, our computational model predictions demonstrated excellent agreement with our experimental testing. We evaluated many lead designs and stimulation configurations to maximally recruit fibers in the VLF and to directly activate motoneurons. Our results suggest that maximal activation can be achieved with longer (e.g., 6 mm) contacts and a larger edge-to-edge spacing (e.g., 12 mm) between electrodes. While these results need to be further validated in future studies, we believe the results of this study will help improve the efficacy of SCS technologies for inspiratory muscle pacing.

# Chapter 4: Evoked Potentials Recorded from the Spinal Cord During Neurostimulation for Pain

Part of the material for this chapter has been adapted with modifications from the following publication:

1. C. J. Anaya, **H. J. Zander** *et al.*, "Evoked Potentials Recorded From the Spinal Cord During Neurostimulation for Pain: A Computational Modeling Study", *Neuromodulation.*, vol. 23, no. 1, 2020, doi: 10.1111/ner.12965. [105]

## 4.1 Abstract

*Objectives*

Spinal cord stimulation (SCS) for pain is typically implemented in an open-loop manner using parameters that remain largely unchanged. To improve the overall efficacy and consistency of SCS, one closed-loop approach proposes to use evoked compound action potentials (ECAPs) recorded from the SCS lead(s) as a feedback control signal to guide parameter selection. The goal of this study was to use a computational modeling approach to investigate the source of these ECAP recordings and technical and physiological factors that affect their composition.

*Methods:*

We developed a computational model that coupled a finite element model of lower thoracic SCS with multicompartment models of sensory axons within the spinal cord. We used a reciprocity-based approach to calculate SCS-induced ECAPs recorded from the SCS lead.

*Results*

Our model ECAPs contained a triphasic, P1, N1, P2 morphology. The model P2-N1 amplitudes and conduction velocities agreed with previous experimental data from human subjects. Model results suggested that the ECAPs are dominated by the activation of axons with diameters 8.7-10.0 μm located in the dorsal aspect of the spinal cord. We also observed changes in the ECAP amplitude, timing, and shape due to the electrode location relative to the vertebrae and spinal cord, as well as from alternate stimulation configurations and pulse widths.

*Conclusion*

Our modeling results suggest that clinically effective SCS relies on the activation of a large number of axons within a narrow fiber diameter range and that several factors affect the composition of the ECAP recordings. These results can improve how we interpret and implement these recordings in a potential closed-loop approach to SCS.

## 4.2 Introduction

Spinal cord stimulation (SCS) is a common neuromodulation therapy for chronic pain conditions (e.g., failed back surgery syndrome) that are often refractory to conventional treatments. The goal of conventional SCS is to deliver electrical stimulation to the large-diameter afferent axons located within the dorsal columns (DCs) of the spinal cord in an attempt to create analgesia

via “gating” mechanisms of pain modulation [13], [183]. However, even after decades of clinical use and dramatic technological improvements, SCS has shown only limited success rates (approximately 58% of patients receive ≥ 50% reduction in pain) [184].

To potentially improve clinical outcomes, a novel closed-loop SCS paradigm has been proposed that utilizes evoked compound action potentials (ECAPs) in the spinal cord as a feedback control signal for stimulation [2], [47]. This approach uses inactive electrodes in the implanted SCS arrays to record ECAPs generated during SCS. These ECAPs reflect the summation of individual action potentials generated by an SCS pulse and provide a quantitative measure of neural recruitment in the spinal cord. The ECAP amplitude serves as a control signal to continuously define stimulation parameters that provide pain relief while minimizing discomfort. While the therapeutic potential of this approach was demonstrated in a recent open-label uncontrolled clinical study [47], the physiological factors influencing these recordings has not been thoroughly investigated. This knowledge gap may limit our ability to use this type of closed-loop approach to optimize SCS-induced analgesia.

Experimental recordings of spinal cord ECAPs in humans report a triphasic morphology – an initial positive wave (P1), followed by a sharp negative peak (N1), and ending with a second positive wave (P2) – and conduction velocities that vary from 37 to 82 m/s depending on the study [185]–[187]. A study by Parker et al. demonstrated that it was possible to record these ECAPs during clinical SCS by using the inactive electrodes on the implanted SCS trial lead [46]. The authors reported that the ECAP amplitude was correlated with the degree of SCS-induced paresthesia coverage over the painful area. The ECAP recordings demonstrated conduction velocities in the range of 49-65 m/s, suggesting that SCS activated axons with diameters between 8.1-10.8 μm [46].

Several factors may affect neural recruitment during SCS and the corresponding spinal ECAP. For example, SCS-induced ECAPs recorded in a sheep model showed that the ECAP amplitude was attenuated when stimulation and recording was performed on electrodes located beneath the vertebral lamina [136]. The spinal cord also moves due to changes in body position (e.g., standing, sitting, prone) as well as respiration and heartbeat [188]. This movement alters the distance between the spinal cord and the stimulating electrodes and can lead to overstimulation or understimulation for a given set of stimulation parameters. A closed-loop SCS system using ECAPs as a control signal may improve outcomes by accounting for these potential changes in the distance between the spinal cord and the stimulating electrodes. The feasibility of the closed-loop approach was demonstrated in a preliminary clinical study in which ≥ 80% of patients experienced a ≥ 50% reduction in their pain [42], [47]. However, there is still a lack of understanding behind the origin of these ECAPs and the various technical and physiological factors that affect the composition of these recordings. Addressing these knowledge gaps could help optimize the clinical efficacy of this closed-loop approach in SCS.

In addition to improving the mechanistic understanding of treatment, it is vital that the implementation of closed-loop SCS maximize the signal-to-noise ratio of the recorded ECAP signal. Large and variable stimulation artifact are recorded during this closed-loop SCS approach, which can obscure the underlying ECAP and cause clinically misleading results [49]. A recent study characterized the significant effect of stimulation artifact on recorded ECAPs, and subsequently identified several stimulation configurations and pulse widths that reduce the stimulus artifact in sheep [49]. These configurations (e.g., bipolar, guarded cathode, and triphasic bipolar) and pulse widths (i.e., 120 – 300 μs) have been shown to not only impact stimulus artifact, but also affect the timing and amplitude of the ECAP recordings. However, it is unknown how

these alternate stimulation configurations and pulse widths affect the underlying neural recruitment during stimulation.

Computational modeling has been used to investigate the physiological and technical factors that affect the direct neural response to SCS [9], [15], [43], [90], [92], [102], [189]. The aim of this study was to use computational modelling to characterize the composition of ECAP recordings during SCS. We developed a computational model that coupled a finite element model of lower-thoracic SCS with multicompartment models of sensory axons to calculate ECAP signals recorded from the spinal cord during stimulation. We hypothesized that the specific fiber-size distribution within the DC of the spinal cord would be responsible for the characteristics of SCS-induced ECAPs. Additionally, we assessed the potential effects of electrode location and dorsal cerebrospinal fluid (CSF) thickness on the amplitude and morphology of SCS-induced ECAP recordings. We hypothesized that ECAP amplitude and shape would be affected by electrode position relative to the vertebrae, electrode position relative to the spinal midline, and dorsal CSF-layer thickness. Finally, we simulated various stimulation configurations and pulse widths and characterized their effects on the ECAP origin and morphology.

### 4.3 Materials and Methods

We used a computational model of SCS to calculate ECAPs recorded via inactive electrodes in the implanted lead. The computational model consisted of two main components: (1) a finite element model (FEM) of an SCS lead implanted in the dorsal epidural space of the spinal cord, and (2) multicompartment cable models of spinal cord DC axons. We calculated ECAPs during SCS using the following procedure: (1) we used the FEM to calculate the extracellular voltages generated in the spinal cord and surrounding tissues during SCS; (2) we populated the

spinal cord white matter with multicompartment cable models of sensory axons; (3) we assessed the direct axonal response to SCS by applying the extracellular voltages to the sensory axon models to obtain transmembrane currents in response to stimulation; and (4) we calculated the SCS-induced ECAP by using a reciprocal FEM solution to determine the voltage generated at each recording electrode.

### *4.3.1 Finite element model (FEM) of SCS*

First, we developed a three-dimensional FEM of lower thoracic SCS to calculate the extracellular voltages generated during stimulation (**Figure 4.1A**). The model consisted of the gray and white matter of the spinal cord and dorsal rootlets, surrounded by CSF, dura mater, as well as epidural fat filling the extradural space and a three-dimensional anatomical representation of the vertebral column including intervertebral discs [115]. The dimensions of the spinal cord and the gray and white matter boundaries were defined by human cadaver samples of the lower thoracic spinal cord [106]. We placed five dorsal rootlets with diameters of 0.25 mm at each spinal level [108]. Unless specified otherwise, we set the dorsal CSF-layer thickness to 3.2 mm [17] and the dura thickness to 300 μm with the dorsal surface flattened for computational simplicity [43], [90]. We stacked seven identical and anatomically-accurate T9 vertebrae in the rostrocaudal direction to make the vertebral column with intervertebral discs based on a previously-published model [115]. We included an explicit representation of an eight-electrode percutaneous lead implanted in the epidural tissue. The SCS lead dimensions mimicked the electrodes used in previously-reported experimental recordings [46], with 1.3 mm lead diameter, 30 cm lead length, 3 mm contact length, and 4 mm edge-to-edge contact spacing. To mimic scar tissue formation around the implanted SCS lead, we included a 300 μm-thick encapsulation layer domain surrounding the lead [113]. We placed the spinal column inside a general thorax domain mimicking the anatomy observed in

healthy humans [117], [119]. We used the 3-Matic Module within the Mimics Innovation Suite (Materialise, Belgium) to define and mesh the model geometry. We specified higher mesh densities at the electrode array and encapsulation layer as well as within a 64-mm long region of interest surrounding the electrodes.

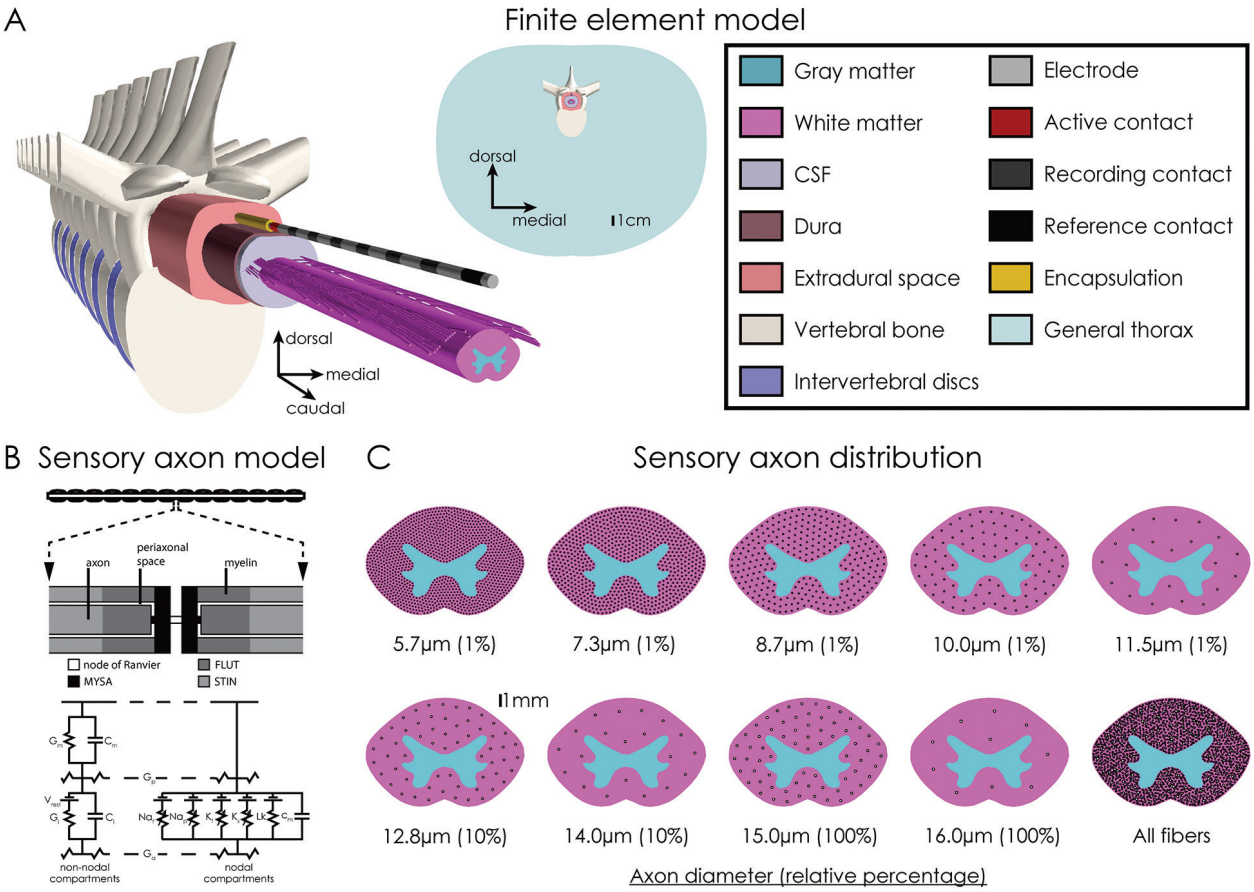


**Figure 4.1**: Computational model of spinal cord stimulation (SCS). A. Finite element model of the lower thoracic spinal cord with surrounding anatomy and an eight-electrode SCS lead implanted in the extradural space. Isometric and axial views of the model are shown on the left and middle, respectively. B. Sensory axon model of dorsal column fibers. Figure was adapted from [127]. C. Distribution of sensory axons in the spinal cord for each discrete fiber diameter used in the first-generation model. We determined the density of each fiber size using previous-published histological data from the human spinal cord [14]. For computational simplicity, we populated our model with only a relative percentage of the total physiological densities and scaled the results accordingly.

We imported the FEM into the finite element analysis software, COMSOL Multiphysics 5.3a (COMSOL, INC., USA). We modeled each tissue using purely resistive properties, and we assigned electric conductivity values using values available in the literature [43], [92], [113]

(**Table 4.1**). We set the encapsulation layer conductivity to 0.11 S/m [113] so that the average model monopolar electrode impedances (359 Ω) matched average clinical values [90]. We used the most caudal electrode (C7) as the stimulating electrode. To simulate current-controlled monopolar stimulation, we applied a unit current source at the stimulating electrode (i.e., 1A) and set the outer-most boundaries of the general thorax domain to ground (i.e., 0V). We modeled the SCS lead shaft as a perfect insulator, and we modeled inactive electrodes as equipotential surfaces with zero net current across their surface. We solved the Laplace equation to determine the resulting voltages at each node in the FEM.

**Table 4.1**: Electrical conductivities assigned to the spinal cord and surrounding tissues

| Tissue | Conductivity (S/m) | Reference |
|---|---|---|
| White matter (longitudinal) | 0.600 | [120] |
| White matter (transverse) | 0.083 | [120] |
| Gray matter | 0.230 | [120] |
| CSF | 1.700 | [120] |
| Dura mater | 0.600 | [43] |
| Extradural space | 0.250 | [92] |
| Vertebral bone | 0.020 | [121] |
| Intervertebral disc | 0.650 | [92] |
| General thorax | 0.250 | [120] |
| Electrode encapsulation | 0.110 | [97], [113] |

*4.3.2 Multicompartment cable model of SCS*

Second, we developed computer models of sensory axons within the DC of the spinal cord. Our multicompartment cable models of DC sensory axons were based on a previously published model of a mammalian sensory axon for specific fiber diameters that was parametrized to accurately reproduce conduction velocities, action potential shape, and strength-duration relationships for sensory axons [77], [127]–[129] (**Figure 4.1B**). For this study, we considered axon diameters of 5.7-16.0 μm with densities based on histological data of the human spinal cord

[14]. In the first-generation model, we divided the histological data describing axon number as a function of diameter into the discrete axon diameters that were available for the given axon model (i.e., 5.7, 7.3, 8.7, 10.0, 11.5, 12.8, 14.0, 15.0, 16.0 μm) [127], [129]. Second, we normalized this data to determine the percentage of axons within each specified diameter range. Third, to calculate the density of axons for a given diameter, we multiplied the percentage of axons by the total density of axons per area (i.e., 22.92 axons/1000 $\mu m^2$) [14]. Finally, to determine the total number of axons for a given diameter, we then multiplied the individual axon density by the cross-sectional area of our model white matter (i.e., 23.62 $mm^2$). The spinal cord DC is densely populated by small diameter axons and contains fewer, more dispersed large diameter axons [14]. To ease computational demand while properly modeling the density of each individual fiber diameter, we selectively used a fraction of the true anatomical densities for each fiber diameter: 1% for diameters ≤ 11.5 μm, 10% for diameters of 12.7 and 14.0 μm, and 100% for diameters ≥ 15.0 μm (**Figure 4.1C**). When calculating the model ECAP, we scaled the relative signal contribution from each fiber size by the appropriate scale factor to achieve 100% of the true anatomical density. We distributed each fiber diameter group evenly within the white matter boundaries using Lloyd's algorithm (**Figure 4.1C**) [130]. We will refer to this model as the "first-generation model" for the remained of this text.

*4.3.3 Assessment of the direct axonal response to SCS*

We assessed the direct axonal response to SCS by applying the extracellular voltages calculated in our FEM to each compartment of our sensory axon cable models. We performed simulations for stimulation amplitudes between 1-10 mA, in 1 mA steps, using a cathodic, monophasic stimulus waveform with a frequency of 50 Hz and a pulse width of 210 μs. We performed all axon simulations with the software package, NEURON, within the Python

programming environment using a supercomputer cluster [133], [190], [191]. We calculated model solutions using backward Euler implicit integration with a time step of 0.002 ms.

### *4.3.4 Calculation of ECAP recordings*

To simulate ECAP recordings, we used the theorem of reciprocity to calculate the time-dependent voltages generated at each electrode by the axonal response to SCS [76], [192]–[195]. We applied a unit current source (i.e., 1 A) at the individual recording electrode, grounded the outer-most boundaries of the general thorax (i.e., 0 V), applied the floating boundary conditions at the other electrodes, and solved the Laplace equation to obtain the resulting model tissue voltages. We interpolated the resulting voltages onto each axonal compartment, interpreting this voltage as the voltage impressed onto the recording electrode by a unit (i.e., 1 A) current source placed at the spatial location of each compartment. We calculated the ECAP by superimposing the voltages generated at the recording electrode from the scaled transmembrane currents of each independent compartment. We repeated this process for each recording electrode and obtained bipolar differential recordings using the most rostral electrode (i.e., C0) as a reference signal, subtracting it from each recording electrode. To mimic the processing done experimentally, we low-pass filtered each signal at 7.5 kHz using a two-pole low-pass Butterworth filter [46].

### *4.3.5 Evaluation of model ECAP recordings*

To characterize our model ECAP recordings, we defined a model sensory threshold (ST) and discomfort threshold (DT). The ST was defined as the stimulus amplitude that resulted in activation of ≥ 10% of the DC fibers in the spinal cord, and the DT was defined as 1.4*ST [9], [90], [92], [196]. We defined the ECAP amplitude as the difference between the P2 and N1 peak amplitudes, ECAP spread as the full width of the signal at half the N1 peak maximum value

(FWHM), and ECAP conduction velocity as the time difference between the N1 peaks recorded at adjacent contacts divided by the center-to-center distance between adjacent electrodes (i.e., 7 mm) [46], [185]–[187], [189].

We explored the effects of electrode position relative to the vertebrae, lead lateral shift, and dorsal CSF-layer thickness on SCS-induced ECAP recording waveform shape and amplitude. In our base model, we placed the lead so that the middle electrode (C3) was centered between adjacent vertebral laminae (**Figure 4.2A**). We then shifted the lead along the rostrocaudal axis by 11.8 mm to center electrode C3 beneath the vertebral lamina to account for any effects of electrode location relative to the vertebrae. Additionally, we characterized the effects of lead lateral displacement by shifting the lead 2.0-mm lateral from the spinal cord midline. Lastly, the amount of CSF between the dura and the spinal cord varies significantly as a function of spinal level, varies between patients, and changes with movement, heartbeat, and respiration [17]. To account for these changes, we shifted the spinal cord along the dorsoventral axis to vary the dorsal CSF-layer thickness between 2.0, 3.2, and 4.4 mm to observe the effects of CSF-layer thickness on the recordings. We calculated each model's ST and DT and compared each model's C3-C0 bipolar ECAP recording at DT. To avoid potential confounds due to differences in stimulation-induced axonal response between models, we also calculated each model ECAP using the same neural response generated with the base model conditions (C3 electrode centered between adjacent vertebral laminae, the lead placed at the spinal cord midline, and a dorsal CSF-layer thickness of 3.2 mm).

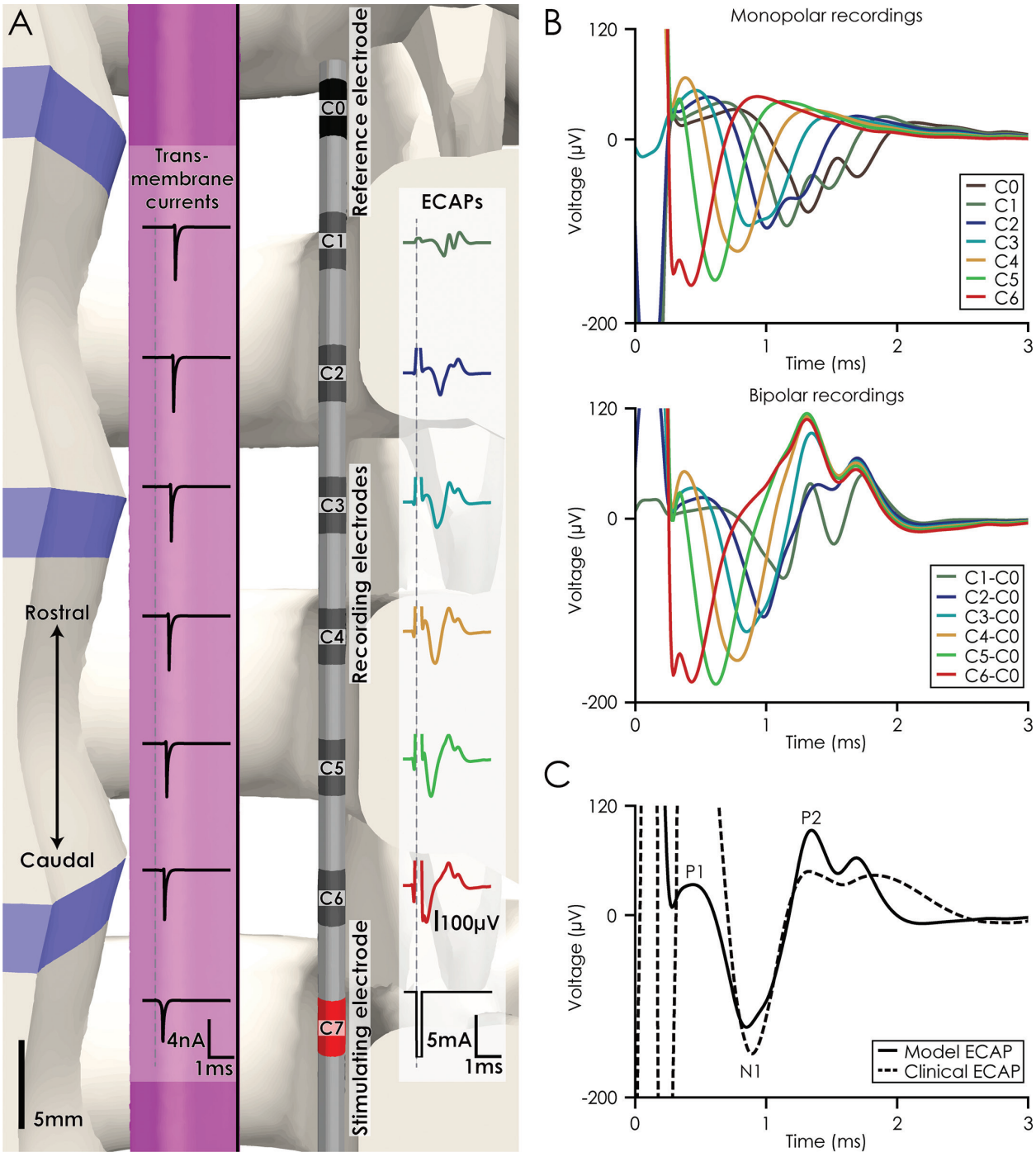


**Figure 4.2**: Model-based recordings of evoked compound action potentials (ECAP) induced by SCS with the first-generation model. A. Sagittal cross section view of the spinal cord, SCS lead, and surrounding vertebral bone and discs. In the traces overlapping the spinal cord, we show an example of the transmembrane currents generated in a single axon in response to a monophasic stimulus pulse. In the traces on the right, we show the stimulus pulse as well as bipolar recordings of the summated response of all axons in our model. The dashed lines represent the time of stimulus onset. B. ECAP recordings at each contact for monopolar and bipolar (referenced to C0) configurations. C. A bipolar (C3-C0) model ECAP recording compared to a previously-reported clinical ECAP recording (see Figure 5B in [46]). The model and clinical ECAP recordings were obtained at stimulation amplitudes near the model-based discomfort threshold and the patient comfort threshold, respectively.

*4.3.6 Continuation of the ECAP modeling – the second-generation model*

In addition to the first-generation computational model described above; we developed a second iteration of the model with a few alterations to the original model design. We designed this new model to better match the experimental setup used in a previous publication presenting preclinical and clinical ECAP recordings during SCS [49]. The main priority of this second model was to evaluate how alternate stimulation configurations and pulse widths influence the ECAP amplitude, timing, and shape.

To mimic the acute recording conditions described in [49], we designed the FEM without an electrode encapsulation layer and updated the conductivity of the epidural space (0.04 S/m) to match previous studies [43], [88], [90], [99], [140]. In the epidural tissue along the anatomical midline, we included a new 56.5 cm long percutaneous SCS array with eight electrodes that each were 3 mm long with a 4 mm edge-to-edge electrode spacing (model #977D260, Medtronic). The novel FEM did not include explicit representations of the dorsal rootlets in the FEM, as previous modeling work has shown that their presence has a negligible effect on model predictions [97].

While the original first-generation model contained only nine distinct axon diameters ranging from 5.7 - 16.0 μm, in the novel model we linearly interpolated the axonal properties for all diameters in between the minimum and maximum characterized axon sizes. To distribute axons within our model, we divided our axon models into 83 unique fiber diameter groups (one fiber diameter group every 0.1 μm between 5.7 and 12.0 μm, and every 0.2 μm between 12.0 and 16.0). Using the method previously described, we determined the number of axons for each fiber diameter group based on cadaver histological data of the superficial dorsal columns in the human spinal cord (**Figure 4.3**) [14], [97], [130]. To better distribute the fibers throughout the white matter of the spinal cord, our fibers were grouped based on the diameter ranges shown in **Table**

**4.2**. Likewise, to ease computational demand, fibers were populated at reduced densities relative to the physiological densities (see **Table 4.2**). These steps reduced the total number of fibers evaluated in our model to 1913 fibers. When we subsequently calculated the model ECAP recordings, we scaled the relative signal contribution of each group by these density scaling factors. This novel computational model will be referred to as the "second-generation" model hereafter in the text, and references both the FEM alterations as well as the fiber distribution changes in the new model.

**Table 4.2**: Fiber sizes, densities, and number of fibers for the second-generation model.

| Fiber diameter range | Density (%) | Number of fibers |
|---|---|---|
| **5.7-6.0** | 0.5 | 111 |
| **6.0-7.0** | 0.5 | 311 |
| **7.0-8.0** | 1.0 | 433 |
| **8.0-9.0** | 1.0 | 237 |
| **9.0-10.0** | 2.5 | 261 |
| **10.0-11.0** | 5.0 | 204 |
| **11.0-12.0** | 10.0 | 132 |
| **12.0-14.0** | 10.0 | 79 |
| **14.0-16.0** | 100.0 | 145 |
| **Total** | - | 1913 |

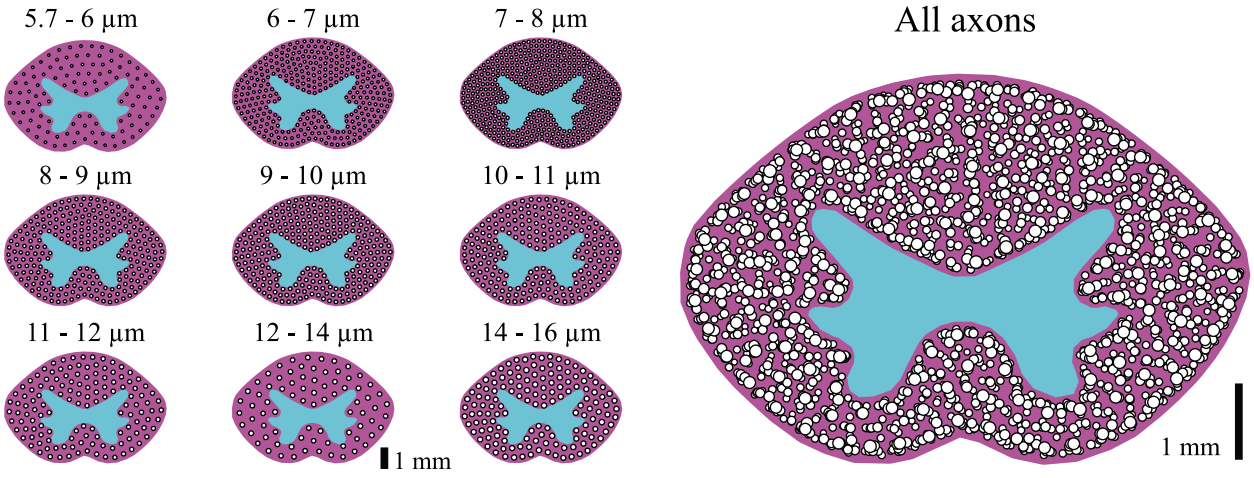


**Figure 4.3**: The fiber distribution in the second-generation model. We separated axons in this model into 83 unique diameters, grouped, and distributed throughout the white matter of the spinal cord. To reduce computational demand, fiber densities were reduced by the values shown in **Table 4.2**.

*4.3.7 ECAP amplitude and timing – stimulation configuration and pulse width*

With the second-generation model, we evaluated how ECAP morphology changes in response to varying stimulation configurations and pulse widths. We simulated monopolar (C7-), bipolar (C7-/C6+), wide bipolar (C7-/C5+), guarded cathode (C7+/C6-/C5+), and guarded anode (C7-/C6+/C5-) stimulation configurations using biphasic, cathodic leading, charge-balanced waveforms with a pulse width of 150 μs. We also applied bipolar (C7-/C6+) stimulation using a charge balanced anodic-leading triphasic stimulation waveform with pulse widths of 75, 150, and then 75 μs. All stimulation configuration and pulse widths for the new model were evaluated at stimulation amplitudes ranging from 1 mA to 10 mA in 1 mA increments and a frequency of 50 Hz. ECAPs generated by this new model were evaluated with a bipolar recording configuration (C0-/C1+).

We also evaluated the effects of pulse width on ECAP amplitude and timing. Using biphasic, cathodic-leading, bipolar (C7-/C6+) stimulation, we applied six pulse widths: 120, 150, 180, 210, 240, and 300 μs. We predicted the neural response to constant current stimulation (1 – 10 mA in 1 mA steps), or with constant charge applied (1.2 μC applied per phase). All axon simulations for the second-generation model were performed using NEURON in a Python programming environment and were computed using a supercomputing cluster at the University of Michigan [133].

## 4.4 Results

*4.4.1 Model-based ECAP recordings*

In the first-generation model, we calculated model ECAP recordings induced by SCS, with a lead placed in the dorsal epidural space at lower thoracic spinal levels. In our model, we estimated

a ST of 6 mA (i.e., ≥ 10% of DC fiber activation) [9], [92] and a corresponding DT of 8 mA (i.e., 1.4*ST) [90], [196] for monopolar stimulation applied at electrode, C7 (frequency = 50 Hz, pulse width = 210 μs) (**Figure 4.2A**). Therefore, we assumed a model-based therapeutic window of 6-8 mA. The model ECAP exhibited a triphasic shape, starting with a positive P1 peak, followed by a sharp negative N1 peak, and ending with a second positive P2 peak for both monopolar and bipolar ECAP recordings (**Figure 4.2B**). The signals recorded on electrodes far from the stimulating electrode are smaller in size and more spread out as the signals in each fiber-size group propagate at different velocities. A small stimulus artifact precedes the model ECAP recording due to the response to the electrical stimulus of the membrane capacitance at the nodes of Ranvier [194]. We compared our model ECAP at the DT with a clinical ECAP recording performed on an electrode 28-mm away from the stimulating electrode [46] (**Figure 4.2C**). Both the clinical and model recordings contain the N1 and P2 peaks of the triphasic spinal ECAP morphology, with a similar N1 peak latency, and a P2-N1 amplitude of 200 μV and 216 μV for the clinical and model ECAPs, respectively. The clinical ECAP recording contains a large stimulus artifact from the recording electrodes being in close proximity to the stimulating electrodes [46]. This large stimulus artifact affects the detection of the P1 peak observed in the model ECAP recording for electrodes near the stimulating electrode.

### *4.4.2 ECAP properties – stimulation amplitude*

In the first-generation model, we calculated ECAPs for stimulus amplitudes over the range of 1-10 mA (**Figure 4.4A**). The P2-N1 amplitude increased linearly over this range of stimulus amplitudes (**Figure 4.4B**). As the stimulus amplitude was increased, the ECAP P2-N1 amplitude increased, but the latency of the N1 peak stayed relatively constant. At lower stimulus amplitudes (i.e., 3 mA), the ECAP conduction velocity was higher (~78 m/s) (**Figure 4.4C**). At higher

stimulus amplitudes (i.e., ≥ 4 mA), smaller diameter fibers were activated and the ECAP conduction velocity decreased to an average value of 53.5 m/s. The FWHM is the width of the N1 waveform at half its peak value and can provide information about the range of fiber diameters captured by the ECAP N1 wave. The FWHM increased linearly at lower stimulation amplitudes but plateaued before reaching the therapeutic window (**Figure 4.4D**), and it shows that the relative proportion of fiber diameters recruited and captured in the N1 peak, stays relatively constant with any further increase in stimulation amplitude.

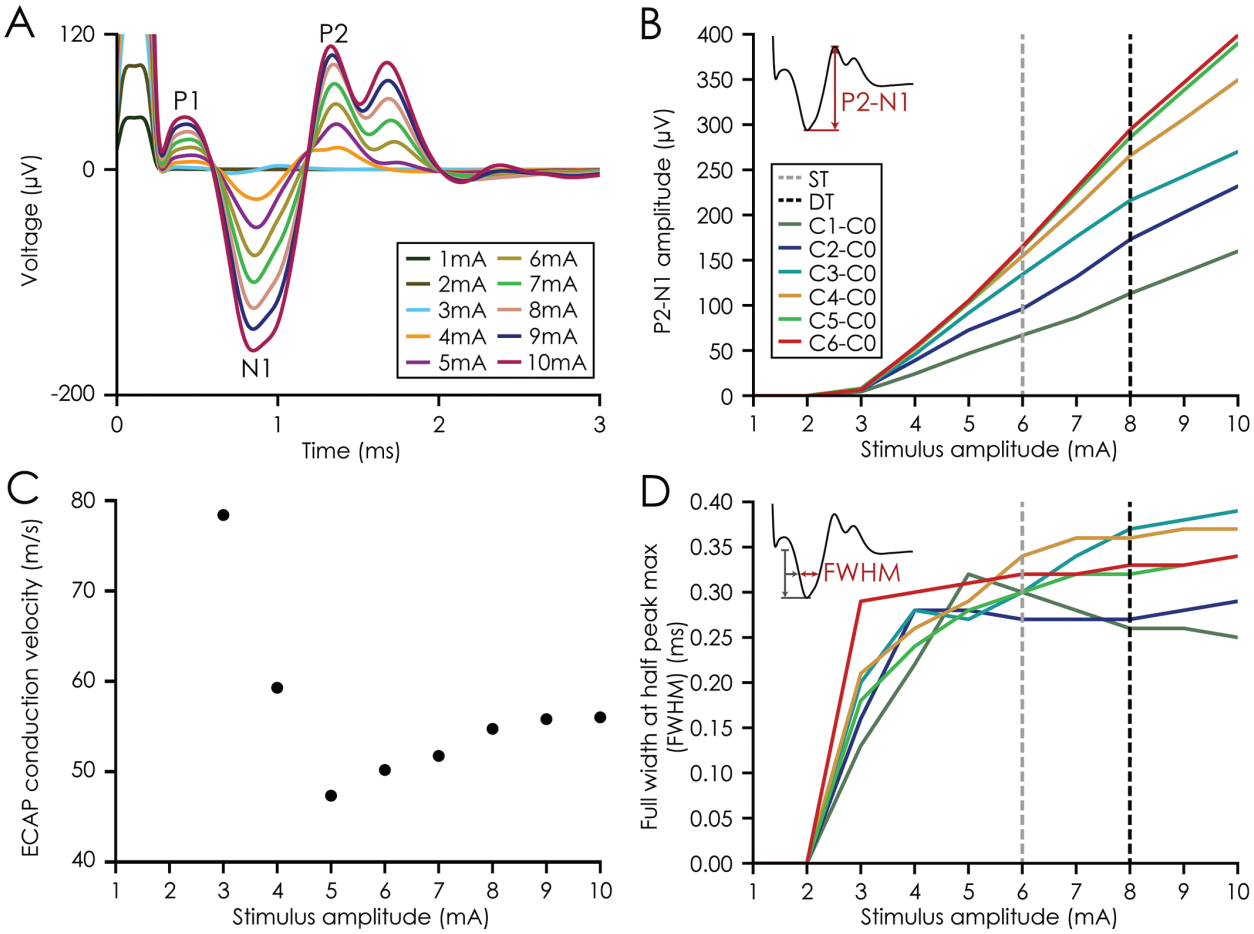


**Figure 4.4**: SCS-induced ECAP recordings as a function of stimulus amplitude using the first-generation model. A. Bipolar ECAP recordings from electrodes, C3-C0, as function of stimulus amplitude. B. P2-N1 amplitude as a function of stimulus amplitude. C. ECAP conduction velocities as a function of stimulus amplitude, measured using the N1 latency difference between neighboring electrodes. D. ECAP full width at half max (FWHM) as a function of stimulus amplitude. In B and D, the model-based therapeutic range is highlighted by dashed lines at the sensory threshold (ST) and discomfort threshold (DT).

*4.4.3 ECAP composition – axon size*

In the first-generation model, we measured the percentage of each fiber-diameter group recruited at each stimulation amplitude (**Figure 4.5A**). We observed fiber activation starting at a minimum stimulus amplitude of 2 mA, which recruited only fibers > 12.0 μm. Within the model-based therapeutic window, the largest percentages of activated fibers had diameters of 7.3, 8.7, and 10.0 μm. To determine the corresponding relative contribution of each fiber diameter to the measured ECAP at each stimulation amplitude, we calculated the individual signal for each fiber diameter group alongside the overall model ECAP (**Figure 4.5B**). We quantified the contribution of each fiber diameter group to the total ECAP amplitude by removing each individual group from the overall ECAP (**Figure 4.5C**). For 7.3 μm fibers, the percent difference in ECAP amplitude after removing these fibers from the ECAP was -11.0 and -13.1% measured at ST and DT, respectively. For 8.7 μm fibers, the percent difference was -35.0 and -39.4% measured at ST and DT, respectively. For 10.0 μm fibers, the percent difference was -30.6 and -27.4% measured at ST and DT, respectively. For 11.5 μm fibers, the percent difference was -8.3 and -7.2% for ST and DT, respectively. For all fibers with diameter ≥ 12.8 μm, the percent difference was -4.5 and -3.2% for ST and DT, respectively. Only a small number of fibers with a diameter of 5.7 μm were recruited within the therapeutic window (i.e., < 2.5%) and removing these fibers only produced a percent difference of 0.0 and -0.4% for ST and DT, respectively. These results demonstrate that the 8.7 and 10.0 μm fibers had the greatest contributions to the overall ECAP amplitude (i.e., P2-N1).

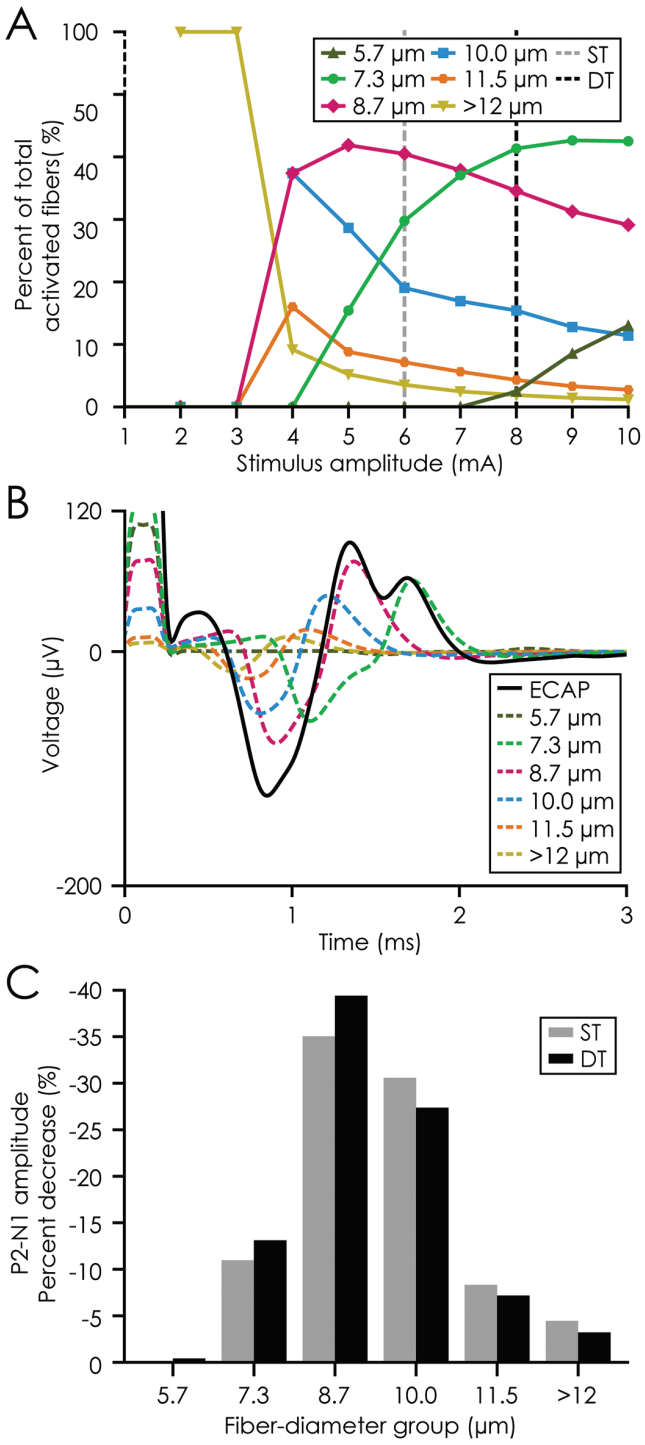


**Figure 4.5**: Contribution of fiber size to the overall ECAP waveform in the first-generation model. A. Relative contributions of each fiber size to the total number of fibers activated at a given stimulus amplitude. Dashed lines indicate an axis break to 100%. The model-based therapeutic range is highlighted by dashed lines at the sensory threshold (ST) and discomfort threshold (DT). B. Overall ECAP waveform along with the individual ECAPs generated by each fiber-diameter group at a stimulus amplitude of 8 mA. C. Percent decrease in P2-N1 amplitude when an individual fiber-diameter group was removed from the ECAP recording at the model-based ST and DT.

*4.4.4 ECAP size and shape – anatomical considerations*

In the first-generation model, we considered three conditions that could potentially affect stimulation thresholds and the corresponding ECAP recording during clinical SCS: 1) electrode position relative to the vertebrae, 2) lead lateral shift, and 3) thickness of the dorsal CSF-layer (**Figure 4.6**). To test the effects of electrode location relative to the vertebral column on ECAP recordings, we shifted the position of the recording electrode, C3, so that it was centered beneath the vertebral lamina (**Figure 4.6A**). When the electrode is centered beneath the vertebral lamina, there was a minimal increase in the number of fibers recruited by stimulation. This shift in electrode position increased the P2-N1 amplitude but had virtually no effect on the waveform morphology (**Figure 4.6A**). Although a lateral shift in lead location activated fibers at different spatial locations within the DC, it produced a minimal difference in the overall number of recruited fibers and minimal differences in the corresponding ECAP shape and amplitude (**Figure 4.6B**). Lastly, increasing the thickness of the dorsal CSF-layer increased the stimulus amplitude required to reach ST (ST=4, 6, and 9 mA for 2.0, 3.2, and 4.4 mm thickness, respectively). The P2-N1 amplitude decreased and the increase in distance between the electrode and the spinal cord exerted a low-pass filtering effect on the waveform shape, apparent in the P2 peak morphology (**Figure 4.6C**). We also compared model ECAP recordings calculated using the same underlying neural activity (i.e., neural activation produced in the base model conditions with C3 centered between lamina, the lead placed at the spinal cord midline, and a dorsal CSF thickness of 3.2 mm) for each set of model conditions with different lead or spinal cord positions. Even with the same underlying neural activity, we observed similar effects on ECAP size and shape for each condition (data not shown). Therefore, the trends observed under the different model conditions were largely

attributed to changes in the lead and/or spinal cord position and not due to corresponding differences in neural recruitment.

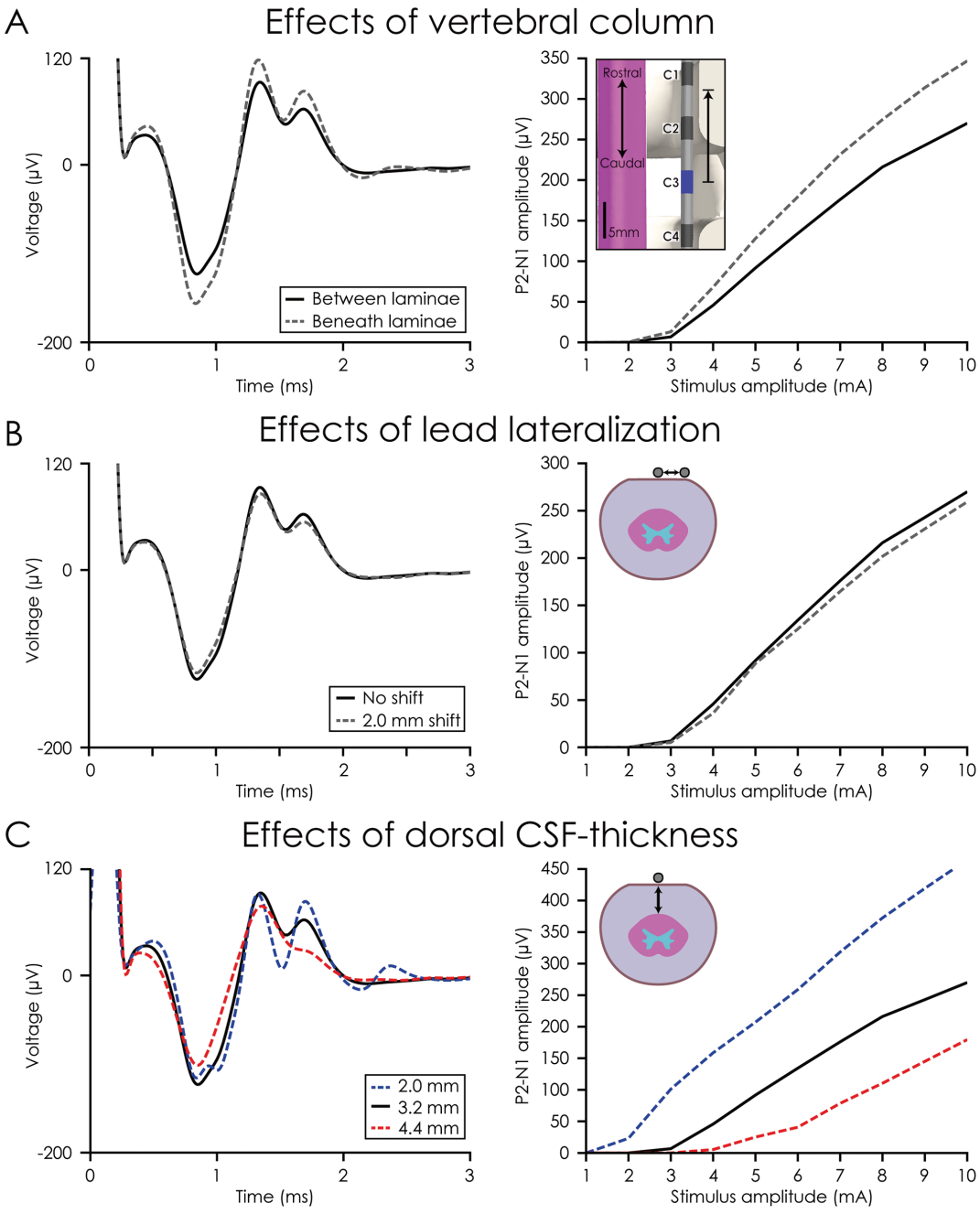


**Figure 4.6**: Effect of electrode and spinal cord position on ECAP recordings in the first-generation model. A. To examine the effect of electrode position relative to the spine, we considered the ECAP with the recording electrode (C3) centered between two vertebral laminae and with the recording electrode centered directly beneath the vertebral lamina (see inset on right). B. To examine the effect of a lateral lead placement, we obtained model based ECAP recordings with the lead centered at the spinal cord midline and the lead shifted 2 mm lateral (see inset on right). C. To examine the effect of spinal cord position, we moved the spinal cord in the anterior-posterior direction and calculated model-based ECAPs for dorsal CSF thicknesses of 2.0, 3.2, and 4.4 mm (see inset on right). Plots in the left column show the ECAP recordings at each model determined discomfort threshold, while the plots in the right column show the corresponding ECAP amplitude as a function of stimulus amplitude.

*4.4.5 ECAP amplitude and fiber recruitment – stimulation configuration*

In the second-generation model, we evaluated the ECAP recordings obtained with various stimulation configurations. These stimulation configurations included biphasic monopolar (C7-), bipolar (C7-/C6+), wide bipolar (C7-/C5+), guarded cathode (C7+/C6-/C5+), and guarded anode (C7-/C6+/C5-). We also evaluated triphasic bipolar stimulation (C7-/C6+). ECAP's generated with a stimulation amplitude of 5mA are shown in **Figure 4.7**. Biphasic monopolar stimulation resulted in an ECAP amplitude of 12.6 μV in the new model. Biphasic bipolar, wide bipolar, and guarded cathode stimulation resulted in much higher ECAP amplitudes of 22.9, 22.8, and 25.0 μV, respectively. Stimulation with the guarded anode and bipolar triphasic resulted in P2-N1 amplitudes of 15.4 and 10.4 μV, respectively (**Table 4.3**). For each configuration, we determined the overall percentage of recruited axons (**Figure 4.7B** and **Table 4.3**). Stimulation with biphasic bipolar, wide bipolar, and guarded cathode configurations recruited a larger number of smaller diameter (<12 μm) fibers and corresponded to higher overall fiber recruitments for these configurations. The trends in the overall fiber recruitment closely resemble the trends in the predicted ECAP amplitudes (**Figure 4.7C**).

**Table 4.3**: ECAP amplitude for each stimulation configuration in the second-generation model (5 mA stimulation)

| **Configuration** | **Monopolar** | **Bipolar** | **Wide bipolar** | **Guarded cathode** | **Guarded anode** | **Bipolar (Triphasic)** |
|---|---|---|---|---|---|---|
| Amplitude (μV) | 12.6 | 22.9 | 22.8 | 25.0 | 15.4 | 10.4 |
| Overall neuron recruitment (%) (All diameters) | 0.57 | 1.18 | 1.22 | 1.29 | 0.58 | 0.46 |

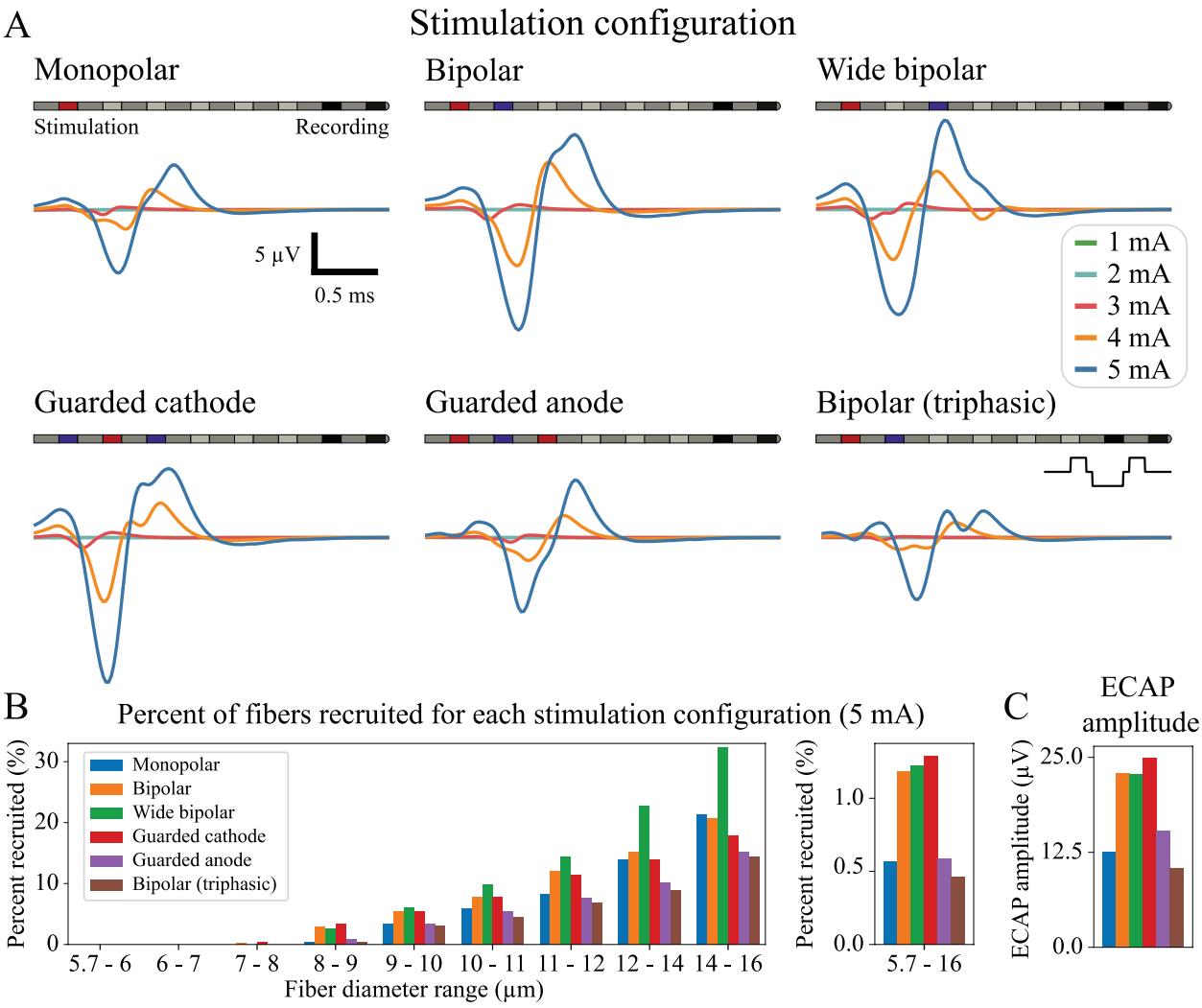


**Figure 4.7**: The effects of stimulation configuration on the amplitude and morphology of ECAP recordings using the second-generation model. A. The effect of stimulation configuration on ECAP morphology for biphasic monopolar, bipolar, wide bipolar, guarded cathode, and guarded anode stimulation, as well as for triphasic bipolar stimulation. B. Left: The percentage of fibers from each diameter range that was recruited during stimulation with each stimulation configuration. Right: The total percent fiber recruitment for the six tested configurations. C. Calculated ECAP amplitude for the various stimulation configurations.

### *4.4.6 ECAP timing – pulse width*

In the second-generation model, we evaluated six pulse widths ranging from 120 µs to 300 µs to determine the effect of pulse width on N1 and P2 timings in the recorded ECAP. We compared ECAP recordings for either constant amplitude (5 mA, **Table 4.4**) or with constant total injected charge per pulse (1.2 µC, **Table 4.5**). The ECAPs that were generated for constant amplitude are plotted in **Figure 4.8A**. In general, both N1 and P2 amplitudes were delayed with

increasing pulse width. Constant amplitude stimulation resulted in N1 times of 0.96, 1.04, 1.06, 1.08, 1.12, and 1.16 ms for pulse widths of 120, 150, 180, 210, 240, and 300 µs, respectively. P2 timings followed a similar trend, although there was more variation in the P2 timing (1.34, 1.46, 1.42, 1.66, 1.46, and 1.92 ms, respectively). To identify the cause of this progressive delay in ECAP timing, we plotted the time delays between the onset of stimulation and AP generation with the charge normalized pulse widths (**Figure 4.8C**). With increases in pulse width, action potential generation became more spread out in time and had a higher mean time to AP initiation (mean ± standard deviation time to AP initiation: 126 ± 63, 152 ± 66, 184 ± 90, 202 ± 80, 232 ± 114, 289 ± 153 µs for 120, 150, 180, 210, 240, and 300, respectively). This likely contributed to the slight decrease in recorded ECAP amplitudes for long pulse width simulations (**Table 4.5**).

**Table 4.4**: ECAP timing for each pulse width for 5 mA stimulation in the second-generation model. N1 and P2 timings are defined as the duration to each peak from the onset of stimulation

| **Pulse width (µs)** | **120** | **150** | **180** | **210** | **240** | **300** |
|---|---|---|---|---|---|---|
| N1 time (ms) | 0.96 | 1.04 | 1.06 | 1.08 | 1.12 | 1.16 |
| P2 time (ms) | 1.34 | 1.46 | 1.42 | 1.66 | 1.46 | 1.92 |

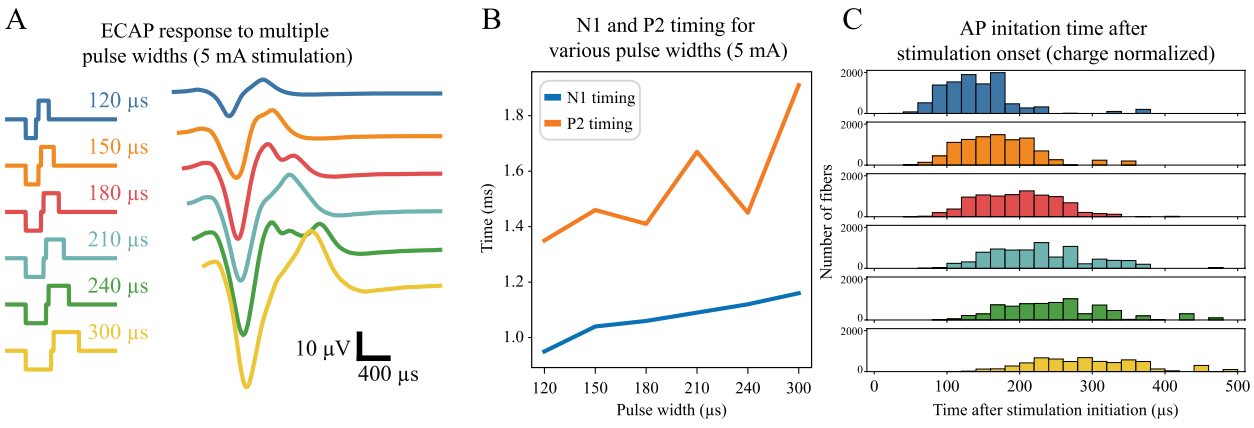


**Figure 4.8**: The effect of pulse width on ECAP and AP initiation times in the second-generation model. A. ECAP generation for pulse widths of 120, 150, 180, 210, 240, and 300 µs and a stimulation amplitude of 5 mA. B. The corresponding timing of N1 and P2 for each tested pulse width. C. Histograms showing the delay in AP initiation from the start of stimulation for each pulse width. We applied stimulation using charge normalized pulses to allow for more direct comparisons in the total neural recruitment (see **Table 4.5**)

**Table 4.5**: ECAP timing for each pulse width using charge normalized pulses in the second-generation model.

| Pulse width (μs) | 120 | 150 | 180 | 210 | 240 | 300 |
|---|---|---|---|---|---|---|
| Stimulation amplitude (mA) | 10 | 8 | 6.667 | 5.714 | 5 | 4 |
| Injected charge (μC) | 1.20 | 1.20 | 1.20 | 1.20 | 1.20 | 1.20 |
| P2-N1 amplitude (μV) | 43.67 | 41.98 | 39.38 | 39.18 | 37.98 | 35.61 |
| N1 time (ms) | 1.00 | 1.04 | 1.06 | 1.1 | 1.12 | 1.16 |
| P2 time (ms) | 1.32 | 1.36 | 1.40 | 1.44 | 1.46 | 1.76 |

## 4.5 Discussion

We developed a computational model of SCS to characterize ECAP signals recorded from the spinal cord. We coupled a FEM and multicompartment models of spinal cord axons to calculate ECAPs recorded from inactive electrodes. We calculated ECAPs over a range of stimulus amplitudes and defined a model-based therapeutic window. We then examined the effects of the lead location relative to the spine and spinal cord, stimulation configuration, and pulse width on the ECAP size, shape, and neural origin.

### *4.5.1 SCS-induced ECAPs and fiber recruitment during clinical SCS*

At the model-based DT, our model ECAPs resembled clinical recordings taken at the patient's comfort limit, i.e., triphasic morphology, similar N1 peak latency, and a similar P2-N1 amplitude (**Figure 4.2C**) [46]. Within the therapeutic window, we observed a linear relationship between the measured P2-N1 amplitude and stimulus amplitude (**Figure 4.4B**). This trend was also observed experimentally in humans and a sheep model of SCS-induced ECAPs [46], [50], [136]. For stimulation amplitudes within the therapeutic window, our model ECAP conduction velocities remained relatively constant with a range of 47-59 m/s. This trend was similar to clinical observations in which the conduction velocities remained relatively constant irrespective of the stimulation amplitude with a range of 49-65 m/s [42], [46].

To examine the range of fiber sizes recruited by clinical SCS, we designed our first-generation model to include physiological fiber sizes and densities within the spinal cord [14]. We then considered the relative contribution of different fiber sizes to the SCS-induced ECAP by examining how removing individual fiber-size groups affected the overall ECAP. Removing fiber diameters of 8.7 and 10.0 μm from the ECAP produced the largest percent decrease in the measured ECAP amplitude (i.e., -35 and -31% at ST, respectively) (**Figure 4.5C**). This result can also help us understand the type of fibers that are recruited in clinically effective SCS. In a previous clinical study, Parker et al. demonstrated a correlation between the ECAP amplitude and the degree of paresthesia overlap with the painful area [46]. Because conventional SCS may require pain-paresthesia overlap [2], DC fibers with diameters ≥ 8.7 μm are most likely activated during clinically effective stimulation.

*4.5.2 Anatomical considerations in SCS-induced ECAP recordings*

In this study, we used our model to investigate several anatomical factors relevant to SCS that might affect the size and/or shape of the ECAP recordings. Our FEM included a realistic anatomical representation of the spine, which allowed us to investigate how electrode location relative to the vertebrae affects ECAP recordings. Parker et al. observed differences in the P2-N1 amplitude that were potentially related to electrode location relative to structures of the sheep vertebral column [136]. Similarly, we observed an increase in the ECAP amplitude for electrodes located beneath the vertebral lamina relative to electrodes located between two adjacent laminae (**Figure 4.6A**). These results were similar when the two model conditions were compared using the same underlying neural activity (data not shown). Therefore, our results suggest that electrodes may have different recording amplitudes based on their relative position along the vertebral column.

Lead migration is common in SCS, especially with percutaneous leads [197], and could result in changes in the ECAP recordings. Our results showed that a 2-mm lateral shift in lead position relative to the spinal cord midline produced no appreciable change in the ECAP amplitude and shape (**Figure 4.6B**). Our model results are similar to spinal potential recordings performed in human volunteers, where the position of an intrathecal recoding microelectrode along the mediolateral axis did not affect the magnitude and shape of the recorded signal [186]. These results suggest that the mediolateral location of the recording electrodes will minimally affect the size and shape of the ECAP recording.

The clinical efficacy of a given set of SCS parameters can vary with movement of the spinal cord that occurs due to postural changes, heartbeat, and respiration [188]. It is estimated that the spinal cord can move ~2-3 mm in the anterior-posterior direction at the lower thoracic spinal levels and can increase or decrease the distance between the spinal cord and the SCS electrodes. Therefore, this movement can lead to overstimulation or understimulation and a corresponding change in the ECAP amplitude [46]. To investigate the effects of spinal cord movement on the corresponding ECAP, we varied the thickness of the dorsal CSF-layer within our model (**Figure 4.6C**). As the dorsal CSF-layer thickness was increased, the model-based ST increased and the ECAP amplitude decreased. Additionally, the increase in distance between the spinal cord and recording electrode affected the shape of the P2 component, smoothing the morphology of the signal. To isolate the effects of electrode-to-cord distance, we also investigated these changes while using the same underlying neural activity in our simulations. With an increase in dorsal CSF-layer thickness and the same underlying neural activity, we observed a similar decrease in ECAP amplitude and a low-pass filtering effect that smoothed the morphology of the waveform (data not shown). Changes in the electrode-to-cord distance can lead to significant changes in the ECAP

amplitude and these trends occur even for the same underlying neural activity. In closed-loop SCS, stimulation amplitude is controlled to maintain ECAP amplitude within a specific range in an attempt to maintain more consistent levels of activation within the spinal cord [47]. To optimize this approach, closed-loop SCS algorithms should consider possible changes in ECAP amplitude that may occur solely due to differences in the electrode-to-cord distance.

*4.5.3 Applications of alternate stimulation configurations and pulse widths*

We evaluated the effect of stimulation configuration on neural activation and corresponding ECAP morphology. Stimulation with biphasic bipolar, wide bipolar, or guarded cathode configurations demonstrated P2-N1 amplitudes that were larger (48 – 137 %) than stimulation with either monopolar, guarded anode, or triphasic bipolar configurations (**Figure 4.7**, **Table 4.3**). These differences in amplitude are largely due to differences in total neural recruitment, which closely tracked with predicted ECAP amplitude. Bipolar, wide bipolar, and guarded cathode configurations all recruited a large number of axons with fiber diameters <12 μm, which resulted in larger P2-N1 amplitudes (**Figure 4.5**, **Figure 4.7**). In addition to the number of fibers recruited, the timing of action potential generation in individual fibers also affected overall ECAP shape. While most stimulation configurations resulted in neural recruitment that was consistent in location and in time, both guarded anode and triphasic bipolar configurations generated additional clusters of action potentials in response to stimulation (data not shown). These additional clusters were generated near the return electrode during the recharge phases of stimulation and may contribute to the smaller ECAP amplitudes observed.

The differences in pulse width also affected ECAP timing, amplitude, and neural recruitment. We simulated ECAP recordings for six pulse widths ranging from 120 μs to 300 μs with both constant amplitude (5 mA) and charge normalized (1.2 μC) stimulation. As expected,

increasing pulse widths activated more axons and led to increased ECAP amplitudes. We found that longer pulse widths progressively increased the delay of N1 and P2 (**Figure 4.7**, **Table 4.4**). This remained consistent even with normalized total injected charge across pulse widths (**Table 4.5**). Our modeling work matches recent experimental observations [49].

To investigate the cause of the increasing ECAP latency, we generated histograms of the offsets between the onset of stimulation and the initiation of APs for various pulse widths (**Figure 4.8C**). Shorter pulse widths led to not only a shorter mean time to AP initiation, but also to more synchrony in AP initiation timing. While the higher amplitude ECAPs of short pulse widths may have benefits from a sensing perspective, the shorter delay and higher stimulation amplitude can result in increased stimulation artifact, which may obfuscate the recorded ECAP [49]. To better identify and evaluate this problem, future research will need to develop computational models to simulate the stimulation artifacts generated during closed-loop SCS, which can be highly variable and posture dependent [49].

### *4.5.4 Study limitations and future work*

In this study, we utilized multicompartment models of sensory axons in the white matter of the spinal cord as the electrical source in our ECAP recordings. These sensory axon models have previously been shown to accurately model the behavior of sensory axons for discrete fiber diameters within the range of diameters used in this study [77], [127], [129]. Since we only used discrete fiber sizes in the first-generation model, differences in conduction velocities in the propagating action potentials of different fiber-size groups led to differences in the P2 peak morphology of our model ECAPs when compared to the clinical ECAP recordings (**Figure 4.2C**). To minimize this effect in the second-generation model, we increased the resolution of the fibers sizes into 83 fiber groups ranging from 5.7 to 16 μm. Additional neuron models, such as dorsal

horn neurons, were excluded from our analysis. Even though only a small percent of current (<10%) is believed to enter the spinal cord during SCS [15], it may be possible to excite dorsal horn neurons at high stimulus amplitudes and somatic action potentials from these neurons have been hypothesized to produce a late potential in the ECAP following the initial triphasic wave [186]. However, in humans, these late potentials were only observed at stimulation amplitudes well above a patient's comfort limit and with significant delay (5-10 ms) [46]. Future work should investigate the extent to which activity in the dorsal horn affects recordings beyond the therapeutic window, as it might provide insights into the nature of the discomfort caused by overstimulation.

Currently, no clear relationship has been established between clinical measurements of ST or DT and the corresponding degrees of DC neural activation. In this study, we defined a model-based ST as ≥10% activation of DC fibers and DT as 1.4*ST to compare the trends observed in our model ECAPs with previously-published clinical ECAP recordings [46]. These assumptions are a potential limitation of our study; however, other recent SCS modeling studies have used a similar percentage of DC activation to estimate ST and motor thresholds that produced results that matched well with clinical and preclinical measurements [9], [92], [198]. Furthermore, the DT has previously been defined as 1.4*ST based on clinical observations and has also been used in previous modeling studies as a close approximation for DT in SCS patients [15], [90], [196].

In this study, we utilized a canonical model of SCS that incorporated anatomical details based on average values in the literature. This canonical model did not account for the inter-patient variability in anatomy and SCS lead placement that has been reflected in interpatient variability in clinical ECAP recording with regards to both amplitude and shape [17], [46]. However, in this study, our goal was to use a canonical model to gain insights into the underlying origin of SCS-induced ECAPs as well as the various physiological and technical factors that affect these

recordings. Future studies should consider sources of inter-patient variability and examine their effects on the ECAP recordings.

One area of interest for future computational models could be the behavior described in Chakravarthy et al. [49]. In this work, the authors describe multiphasic ECAPs that include additional negative and positive peaks (N2, P3, etc.) that can be recorded in some patients. These additional peaks appear to manifest at longer pulse width and have smaller amplitudes than N1 or P2 peaks. The authors noted that these additional peaks did not appear in every experiment, but they expressed the potential for these peaks to assess ECAP amplitude when earlier features are effaced by artifact. In this work, we observed that action potentials could be initiated on the return electrode during the recharge phase of stimulation (or during the initial anodic phase of tripolar stimulation). In general, longer pulse widths tended to increase the number of neurons firing on this recharge phase, and the effect was also dependent on the electrode position with respect to the vertebrae. It may be that these secondary action potentials contribute to the multi-phase ECAPs previously described in the sheep model. These additional waveforms may also be a result of activation of the post-synaptic dorsal column pathway [199]–[201]. Future modeling work will be needed to characterize these two theories and identify how they contribute to the observed multiphasic effect. Additionally, work will be needed to determine how electrode position and geometry influence this activation.

### 4.6 Conclusion

ECAPs during SCS can be used to investigate neural activation and the corresponding mechanisms of action of clinical SCS. These ECAPs also have the potential to serve as a control signal to optimize SCS parameters during closed-loop SCS on a patient-specific basis. However,

to successfully interpret these signals, we must understand their origin. In this study, we used a computational model to investigate various technical and physiological factors that affect the composition of these ECAP recordings. Our computational modeling results reproduced several trends observed in clinical data. Our modeling results suggest that clinically effective SCS relies on the activation of a large number of axons within a narrow fiber diameter range (i.e., 8.7-10.0 μm). Model results also suggest that the ECAP amplitude and shape is affected by electrode position relative to the vertebrae as well as the amount of CSF between the recording electrodes and the spinal cord. We also characterized changes in ECAP morphology, origin, and timing using alternate stimulation configurations and pulse widths that have previously been described to minimize stimulation artifact. We found that bipolar, wide bipolar, and guarded cathode maximized ECAP amplitudes through increased neural recruitment. Longer pulse widths were shown to increase the delay in ECAP peaks due to delays in AP generation for individual fibers within the cord, while also requiring smaller stimulation amplitudes. This may be beneficial for stimulus artifact reduction. Overall, these findings improve our mechanistic understanding of closed-loop stimulation and can be used for more consistent and efficacious stimulation.

# Chapter 5: Discussion

## 5.1 Summary of main findings and implications

SCS is a neuromodulation therapy with both a long history and a recent period of rapid innovation. This growth has led to several novel developments and applications of SCS for the treatment of chronic pain and for muscle activation following spinal cord injury (SCI) [1]. While these SCS applications have shown efficacious results and some have even earned approval by the United States Food and Drug Administration (FDA), there remain considerable mechanistic knowledge gaps [2]. This thesis provides detailed computational analysis of the mechanisms and neural activation of three SCS applications: SCS for inspiratory muscle activation following SCI and both traditional and closed-loop SCS for chronic pain management.

In Chapter 2 of this work, I investigated the impact of several anatomical and technical factors that can influence the neural response to SCS [97]. I compared and quantified neural predictions for several common modeling simplifications, as well as developed several new techniques for model creation. There were significant changes in model predictions that arose from variations in overall model impedance (for voltage-controlled stimulation), dura mater conductivity, and representation of the vertebrae within the finite element model. I also evaluated simplifications that resulted in minor changes in neural threshold predictions, such as representation of the rootlets in the finite element model and overall model impedance (for current controlled stimulation). Finally, I determined that frequency dependent conductivities and permittivities do not significantly alter model predictions for 10 kHz stimulation.

The primary focus of this chapter (Chapter 2) was to identify how changes to the finite element model design effect the predicted neural response to SCS. This has both direct implications in clinical applications of SCS and may also aid in future SCS modeling development. For clinical applications, this work suggested that current-controlled stimulation may reduce the effects of electrode impedance variability as compared to voltage-controlled stimulation. These results are highly relevant to the clinical implementation of SCS due to the large variations in electrode impedance observed across electrodes within an individual array or across patients and the continued use of voltage-controlled stimulation in clinical settings [2], [12]. I also identified that neural recruitment generated by percutaneous electrodes can change based on the lead position relative to the spine. While this variation can be reduced with paddle arrays, it should be considered in the future implementation of SCS.

In addition to improving the clinical implementation, the work in Chapter 2 may directly impact future modeling studies. I identified several factors of model design that improve the predictions of neural activity (i.e., vertebral position relative to spine, dura conductivity, tissue impedance for voltage-controlled stimulation) or that can be excluded from the finite element model to decrease model development time (i.e., tissue impedance for current-controlled stimulation, frequency dependent tissue properties for 10 kHz stimulation, dorsal rootlets in the finite element model). These factors influenced the design of the models in subsequent chapters (e.g., the lead position relative to the vertebrae directly led to our model reproducing experimental results in Chapter 4, the vertebrae were modeled while the rootlets were not included in the FEM in Chapter 3, etc.). We hope the factors described in this chapter may have a similar effect on future model development and results.

In Chapter 3, I developed a computational model of ventral T2 SCS for inspiratory muscle activation in canines [168]. To do this, I evaluated the activation of two neuronal targets that lead to inspiratory muscle activation: ascending fibers in the ventrolateral funiculus (VLF) that synapse onto the phrenic motoneurons (innervating the diaphragm) and the local intercostal motoneurons (innervating the inspiratory intercostals) [7], [58], [60], [96]. With this model, I evaluated variations in lead separation, contact length, contact spacing, and stimulation configuration to maximize recruitment of the target neural groups. We then evaluated the optimal (6 mm contacts with 12 mm gaps) and suboptimal (3 mm contacts with 3 mm gaps) lead configurations via *in vivo* canine experiments. The modeling predictions demonstrated excellent agreement with the experimental results.

Naturally, the modeling performed in Chapter 3 has direct benefit on the implementation of HF-SCS for inspiration. Prior to this work, experimental evidence of this therapy was mostly empirical, which limited future development of this technique. The lead configuration developed can be used in subsequent experimental work to better understand the mechanisms of this novel SCS application. In addition to direct experimental impact, the mechanistic identification of likely neural targets may lead to improved translational capabilities. A similar therapy, SCS for walking following SCI, has utilized the mechanistic understanding from computational models to translate the therapy from rats and non-human primates into efficacious human studies [1], [6], [9], [65], [67], [202], [203]. We hope that a similar translation occurs with ventral HF-SCS. Historical studies provide optimism on the translational capabilities of neuromodulatory techniques from canine to effective clinical trials and devices [62], [66], [204]–[206]. Were this translation to occur, future modeling work can use the methodology and results presented here to optimize stimulation for human subjects, as there are significant variations in the spinal cord anatomy (specifically

ventral CSF thickness, spinal cord size, and variations in the respiratory effects of inspiratory muscles) that may influence the effectiveness of therapy and lead design [17], [72], [171]–[173].

In Chapter 4 of this work, I developed a computational model of closed-loop SCS for chronic pain management [105]. My model predicted ECAP peaks, amplitudes, and timings that were consistent with experimental evidence. I identified the neural origins of the recorded ECAP waveform to largely be generated by a relatively narrow fiber range (i.e., 8.7-10.0 μm). I then evaluated changes in the ECAP waveform that result from alternate lead and anatomical positions. While moving the lead laterally had little effect on ECAP predictions, the rostrocaudal lead location with respect to the vertebrae influenced ECAP amplitudes, which was consistent with literature [105], [136]. Furthermore, the dorsal thickness of the CSF had a large impact on recorded ECAP amplitudes. Finally, I evaluated ECAP signals for alternate stimulation configuration and pulse widths that have been previously shown to alter stimulation artifact and ECAP morphologies. I found bipolar, wide bipolar, and guarded cathode configurations maximized ECAP amplitudes through increased recruitment of small (<12 μm) diameter fibers. Increasing pulse widths also generated progressively longer delays in ECAP timing due to the increased time to mean neural recruitment.

This modeling work can be used to improve our understanding and implementation of closed-loop SCS. We sought to investigate the neural origins of the ECAP signal as well as how it changed in response to a variety of anatomical and technical factors. As an objective measure of neural activation, a better understanding of the neural origins of the ECAP may have profound clinical implications. Specifically, ECAP measurements could be used to inform about the health of the spinal cord and the effects of treatment over time [41]. ECAP waveforms may also be used for the diagnoses and treatment of chronic pain and help develop personalized mechanism-based

treatments. They might be used to help identify neural dysfunctions, and could help optimize dosing of treatments that impact neural activation, like some pain medication (e.g., opioids and anticonvulsants) [41]. For these possible outcomes, the origins of the ECAP need to be highly characterized and understood. Furthermore, this work also evaluated changes in ECAP morphology and origin for several stimulation configurations and pulse widths that reduce the effects of stimulation artifact, which has been previously shown to completely mask the ECAP signal [49]. These configurations and waveforms allow for better identification of the ECAP waveform during treatment, which is vital for the treatment's success.

## 5.2 Future directions

### *5.2.1 Model reductions*

One major goal of Chapter 2 was to evaluate how simplifications in model design affect the predicted neural response of SCS. This was intended to guide future modeling work and directly impacted the models developed in Chapters 3 and 4. This project identified factors that affect model results and suggests factors that can be neglected in model design, streamlining model development and testing. The improved accuracy and development speed is especially important with the recent FDA announcement to integrate virtual testing and computational modeling into the medical device regulatory approval process [207]. Furthermore, it is predicted that models will see increased future demand due to the effective translational capabilities, expanded integration in medical devices, and the increased use as clinical decision support tools [1]. Therefore, this present work identifying the necessary details for model development is very impactful for future modeling studies.

There are two main factors that warrant further analysis: dura mater conductivity and the presence of dorsal rootlets in the FEM. My model found that dura mater conductivity significantly altered predictions of neural activation. While the dural membrane conductivity remains largely unknown, it would be a valuable parameter for future experimental studies to evaluate [139]. Additionally, the present work identifies that the presence of dorsal rootlets does not significantly alter neural thresholds; however, these results may not extend to alternate spinal levels due to variations in root/rootlet density, branching, and diameter [155], [156]. Future modeling studies should evaluate the influence of cervical, lumbar, or sacral roots/rootlets in FEM predictions using the same methodology described in Chapter 2.

### *5.2.2 Ventral HF-SCS for inspiration*

Although the results of Chapter 3 identify two direct neural targets of stimulation and focus of their activation, HF-SCS involves a monosynaptic or polysynaptic reflex arc which likely contributed to the observed inspiratory response [7], [54], [59], [60], [73], [74], [208]. Future iterations of the model could evaluate the effects of indirect neural activation resulting from the synaptic structure of the pre-phrenic motoneurons as well as both interneurons and afferent sensory neurons that synapse on the inspiratory intercostals [60], [208], [209]. Indirect effects of stimulation may be responsible for the frequency dependent effects of stimulation. A recent computational model demonstrated that high frequency, low amplitude SCS can result in temporal summation of EPSP's on post-synaptic neurons, leading to increased motor neuron recruitment [67]. A similar effect may contribute to the observed inspiratory behavior. Characterizing these effects and the synaptic structure will give a more complete understanding of the mechanisms leading to inspiratory muscle activation.

For future translation of this work, it is vital that the results produced in a canine model translate into similar levels of activation in humans. While historical success for translation of respiratory therapies give optimism about the success of HF-SCS, future modeling work will need to determine the optimal stimulation configuration for humans using the same methodology described in Chapter 3 [62], [66], [204]–[206]. This future modeling work will be essential given the variations in anatomy between species, including vastly differing ventral CSF thicknesses, spinal cord sizes, and variations in the location and respiratory contribution of inspiratory muscles across species [17], [60], [72], [171]–[173]. These differences warrant the development of novel computational models to optimize the stimulation parameters.

### *5.2.3 Closed-loop SCS for pain management*

While the application of closed-loop SCS has demonstrated remarkable success in clinical trials, there are still unknowns related to the generation of the ECAP waveform. In particular, ECAP morphology occasionally shows additional peaks in the recorded signal [49]. These additional peaks may be a result of action potential initiation near the return electrode during the recharge phase of stimulation (the return electrode applies cathodic stimulation during the recharge phase of stimulation). However, an additional hypothesis suggests that these additional peaks arise from activation of the post-synaptic dorsal column pathway [199]–[201]. Evaluation of these two hypotheses is ideal for future computational models, and the implementation of them may be based on the methods established in Chapter 4.

Likewise, while the present work explored a limited number of metrics related to ECAP generation and morphology, much work remains to fully characterize how ECAPs change in response to stimulation frequency, posture, alternate lead designs, anatomical factors (including spinal cord size, spinal canal dimensions, CSF volumes, fiber diameters, axon distribution, neural

trajectories, ion channel properties, heart rate, respiration, disease state, etc.), and movement [49], [50]. It may be ideal to evaluate these factors using a patient-specific approach, which has recently demonstrated superior accuracy to traditional canonical approaches [94]. Future work should focus on closed-loop neural activation changes with respect to frequency. A recent study evaluating frequency effects for closed-loop stimulation found that as the stimulation frequency increased, recorded ECAP amplitudes dropped while perceived paresthesia increased [50]. The authors hypothesized multiple mechanisms for the decrease in ECAP amplitude, including potassium accumulation in the peri-axonal space or electrogenic pump mediated excitability which could lead to intermittent blocking of fibers or increases in fiber thresholds [50]. These hypotheses are well suited for future computational models, and may give insight into how sensation is encoded in the spinal cord [50].

One limitation of the closed-loop approach to SCS is the large stimulus artifact that can mask the underlying ECAP signal. While the present work identifies alternate stimulation configurations and pulse widths that minimize stimulation amplitude, these results could be improved if a biophysical model of stimulus artifact were included in the analysis. This artifact model might require predictions of the tissue resistance and a circuit model of the electrode tissue interface, as was done in a recent study evaluating cortico-cortical evoked potentials [210]. Improved artifact modeling could both improve the predictions and analysis of computational models of closed-loop SCS, but also could lead to more efficacious clinical outcomes through improved artifact removal methods.

The inherent methodology of closed-loop SCS directly addresses another major limitation of current computational modeling techniques: validation. In traditional SCS modeling, validation metrics typically include comparing the model electrode impedance to *in vivo* tissue impedances,

or by comparing perception/discomfort thresholds to some percentage of neural activity [1], [90], [92], [97]. However, these metrics either have unclear/arbitrary origins or do not directly measure neural activity [105]. A unique characteristic of the closed-loop paradigm is that it allows for rigorous validation of models using a metric directly resulting from neural activity. The present work represents the initial development of this validated model that reproduces experimental trends and evaluates the neural origins of the ECAP signal and factors that influence ECAP morphology. Future computational studies may use the methodology described in this work to develop more rigorous validation metrics to improve the accuracy of computational models. This will not only improve the understanding and implementation of closed-loop stimulation; but may also lead to improvements in novel forms of SCS, including burst, 10 kHz, and traditional open-loop stimulation.

## Bibliography


[1] M. Capogrosso and S. F. Lempka, “A computational outlook on neurostimulation,” *Bioelectron. Med.*, vol. 6, no. 1, 2020, doi: 10.1186/s42234-020-00047-3.

[2] S. F. Lempka and P. G. Patil, “Innovations in spinal cord stimulation for pain,” *Current Opinion in Biomedical Engineering*, vol. 8. Elsevier, pp. 51–60, Dec. 01, 2018, doi: 10.1016/j.cobme.2018.10.005.

[3] D. J. Anderson *et al.*, “Intradural Spinal Cord Stimulation: Performance Modeling of a New Modality,” *Front. Neurosci.*, vol. 13, p. 253, Mar. 2019, doi: 10.3389/fnins.2019.00253.

[4] T. C. Zhang, J. J. Janik, and W. M. Grill, “Mechanisms and models of spinal cord stimulation for the treatment of neuropathic pain,” *Brain Res.*, vol. 1569, pp. 19–31, 2014, doi: 10.1016/j.brainres.2014.04.039.

[5] R. van den Brand *et al.*, “Restoring voluntary control of locomotion after paralyzing spinal cord injury,” *Science (80-. ).*, vol. 336, no. 6085, pp. 1182–1185, 2012, doi: 10.1126/science.1217416.

[6] N. Greiner *et al.*, “Recruitment of upper-limb motoneurons with epidural electrical stimulation of the cervical spinal cord,” *Nat. Commun.*, vol. 12, no. 1, 2021, doi: 10.1038/s41467-020-20703-1.

[7] A. F. DiMarco and K. E. Kowalski, “Activation of inspiratory muscles via spinal cord stimulation,” *Respir. Physiol. Neurobiol.*, vol. 189, no. 2, pp. 438–449, Nov. 2013, doi: 10.1016/j.resp.2013.06.001.

[8] A. F. DiMarco, K. E. Kowalski, R. T. Geertman, and D. R. Hromyak, “Spinal cord stimulation: A new method to produce an effective cough in patients with spinal cord injury,” *Am. J. Respir. Crit. Care Med.*, vol. 173, no. 12, pp. 1386–1389, 2006, doi: 10.1164/rccm.200601-097CR.

[9] M. Capogrosso *et al.*, “A Computational Model for Epidural Electrical Stimulation of Spinal Sensorimotor Circuits,” *J. Neurosci.*, vol. 33, no. 49, pp. 19326–19340, 2013, doi: 10.1523/JNEUROSCI.1688-13.2013.

[10] N. Greiner and M. Capogrosso, “Anatomically realistic computational model to assess the specificity of epidural electrical stimulation of the cervical spinal cord,” in *Biosystems and Biorobotics*, vol. 21, Springer, Cham, 2019, pp. 44–48.

[11] K. E. Kowalski, J. R. Romaniuk, P. A. Kirkwood, and A. F. DiMarco, “Inspiratory muscle activation via ventral lower thoracic high-frequency spinal cord stimulation,” *J. Appl. Physiol.*, vol. 126, no. 4, pp. 977–983, 2019, doi: 10.1152/japplphysiol.01054.2018.

[12] M. A. Moffitt, D. C. Lee, and K. Bradley, “Spinal Cord Stimulation: Engineering Approaches to Clinical and Physiological Challenges,” in *Implantable Neural Prostheses 1*, E. Greenbaum and D. Zhou, Eds. Springer US, 2009, pp. 155–194.

[13] R. Melzack and P. D. Wall, “Pain mechanisms: a new theory.,” *Science*, vol. 150, no. 3699, pp. 971–9, Nov. 1965, doi: 10.1126/SCIENCE.150.3699.971.

[14] H. K. P. Feirabend, H. Choufoer, S. Ploeger, J. Holsheimer, and J. D. van Gool, "Morphometry of human superficial dorsal and dorsolateral column fibres: significance to spinal cord stimulation," *Brain*, vol. 125, no. 5, pp. 1137–1149, 2002, doi: 10.1093/brain/awf111.
[15] J. Holsheimer, "Which Neuronal Elements are Activated Directly by Spinal Cord Stimulation," *Neuromodulation Technol. Neural Interface*, vol. 5, no. 1, pp. 25–31, 2002, doi: 10.1046/j.1525-1403.2002._2005.x.
[16] R. B. North, M. G. Ewend, M. T. Lawton, and S. Piantadosi, "Spinal cord stimulation for chronic, intractable pain: Superiority of 'multi-channel' devices," *Pain*, vol. 44, no. 2, pp. 119–130, Feb. 1991, doi: 10.1016/0304-3959(91)90125-H.
[17] J. Holsheimer, J. A. Den Boer, J. J. Struijk, and A. R. Rozeboom, "MR assessment of the normal position of the spinal cord in the spinal canal," *Am. J. Neuroradiol.*, vol. 15, no. 5, pp. 951–959, 1994, Accessed: Jul. 10, 2018. [Online]. Available: http://www.ajnr.org/content/ajnr/15/5/951.full.pdf.
[18] M. J. T. Fitzgerald, E. Mtui, and G. Gruener, *Clinical Neuroanatomy and Neuroscience - 5th edition*, 5th ed. Philadelphia, U.S.A: W.B. Saunders Co., 2007.
[19] S. N. Raja *et al.*, "The revised International Association for the Study of Pain definition of pain: concepts, challenges, and compromises," *Pain*, vol. 161, no. 9. NLM (Medline), pp. 1976–1982, Sep. 01, 2020, doi: 10.1097/j.pain.0000000000001939.
[20] C. M. Russo and W. G. Brose, "Chronic pain," *Annual Review of Medicine*, vol. 49. Annual Reviews Inc., pp. 123–133, Nov. 28, 1998, doi: 10.1146/annurev.med.49.1.123.
[21] D. J. Gaskin and P. Richard, "The economic costs of pain in the United States," *J. Pain*, vol. 13, no. 8, pp. 715–724, Aug. 2012, doi: 10.1016/j.jpain.2012.03.009.
[22] D. A. Fishbain, R. Cutler, H. L. Rosomoff, and R. S. Rosomoff, "Chronic pain-associated depression: Antecedent or consequence of chronic pain? A review," in *Clinical Journal of Pain*, 1997, vol. 13, no. 2, pp. 116–137, doi: 10.1097/00002508-199706000-00006.
[23] T. E. Elliott, C. M. Renier, and J. A. Palcher, "Chronic pain, depression, and quality of life: Correlations and predictive value of the SF-36," *Pain Med.*, vol. 4, no. 4, pp. 331–339, Dec. 2003, doi: 10.1111/j.1526-4637.2003.03040.x.
[24] C. A. Warms, J. A. Turner, H. M. Marshall, and D. D. Cardenas, "Treatments for chronic pain associated with spinal cord injuries: Many are tried, few are helpful," *Clin. J. Pain*, vol. 18, no. 3, pp. 154–163, 2002, doi: 10.1097/00002508-200205000-00004.
[25] M. Zenz, M. Strumpf, and M. Tryba, "Long-term oral opioid therapy in patients with chronic nonmalignant pain," *J. Pain Symptom Manage.*, vol. 7, no. 2, pp. 69–77, Feb. 1992, doi: 10.1016/0885-3924(92)90116-Y.
[26] R. A. Rudd, N. Aleshire, J. E. Zibbell, and R. Matthew Gladden, "Increases in Drug and Opioid Overdose Deaths - United States, 2000-2014," *Am. J. Transplant.*, vol. 16, no. 4, pp. 1323–1327, 2016, doi: 10.1111/ajt.13776.
[27] K. Kumar *et al.*, "Spinal cord stimulation versus conventional medical management for neuropathic pain: A multicentre randomised controlled trial in patients with failed back surgery syndrome," *Pain*, vol. 132, no. 1–2, pp. 179–188, Nov. 2007, doi: 10.1016/j.pain.2007.07.028.
[28] R. G. Hazard, "Failed back surgery syndrome: Surgical and nonsurgical approaches," in *Clinical Orthopaedics and Related Research*, Feb. 2006, vol. 443, no. 443, pp. 228–232, doi: 10.1097/01.blo.0000200230.46071.3d.
[29] W. S. Oh and J. C. Shim, "A Randomized Controlled Trial of Radiofrequency

Denervation of the Ramus Communicans Nerve for Chronic Discogenic Low Back Pain," *Clin. J. Pain*, vol. 20, no. 1, pp. 55–60, 2004, doi: 10.1097/00002508-200401000-00011.
[30] J. Guzmán, R. Esmail, K. Karjalainen, A. Malmivaara, E. Irvin, and C. Bombardier, "Multidisciplinary rehabilitation for chronic low back pain: systematic review.," *BMJ*, vol. 322, no. 7301, pp. 1511–6, Jun. 2001, doi: 10.1016/j.jclinepi.2006.03.009.
[31] N. B. Finnerup *et al.*, "Pharmacotherapy for neuropathic pain in adults: a systematic review and meta-analysis.," *Lancet. Neurol.*, vol. 14, no. 2, pp. 162–73, Feb. 2015, doi: 10.1016/S1474-4422(14)70251-0.
[32] R. H. Dworkin *et al.*, "Advances in Neuropathic Pain," *Arch. Neurol.*, vol. 60, no. 11, p. 1524, Nov. 2003, doi: 10.1001/archneur.60.11.1524.
[33] Fortune Business Insights, "Spinal Cord Stimulation Market Research Report," 2021. [Online]. Available: https://www.fortunebusinessinsights.com/industry-reports/spinal-cord-stimulation-market-100313.
[34] H. L. Fields and A. I. Basbaum, "Brainstem control of spinal pain-transmission neurons.," *Annu. Rev. Physiol.*, vol. 40, pp. 217–248, Nov. 1978, doi: 10.1146/annurev.ph.40.030178.001245.
[35] J. Barchini *et al.*, "Spinal segmental and supraspinal mechanisms underlying the pain-relieving effects of spinal cord stimulation: An experimental study in a rat model of neuropathy," *Neuroscience*, vol. 215, pp. 196–208, Jul. 2012, doi: 10.1016/J.NEUROSCIENCE.2012.04.057.
[36] B. Linderoth and R. D. Foreman, "Conventional and Novel Spinal Stimulation Algorithms: Hypothetical Mechanisms of Action and Comments on Outcomes," *Neuromodulation*, vol. 20, no. 6, pp. 525–533, 2017, doi: 10.1111/ner.12624.
[37] S. F. Lempka, B. Howell, K. Gunalan, A. G. Machado, and C. C. McIntyre, "Characterization of the stimulus waveforms generated by implantable pulse generators for deep brain stimulation," *Clin. Neurophysiol.*, vol. 129, no. 4, pp. 731–742, Apr. 2018, doi: 10.1016/j.clinph.2018.01.015.
[38] T. Deer *et al.*, "Success Using Neuromodulation With BURST (SUNBURST) Study: Results From a Prospective, Randomized Controlled Trial Using a Novel Burst Waveform," *Neuromodulation*, vol. 21, no. 1, pp. 56–66, 2018, doi: 10.1111/ner.12698.
[39] D. De Ridder, M. Plazier, N. Kamerling, T. Menovsky, and S. Vanneste, "Burst spinal cord stimulation for limb and back pain," *World Neurosurgery*, vol. 80, no. 5. 2013, doi: 10.1016/j.wneu.2013.01.040.
[40] L. Kapural *et al.*, "Novel 10-kHz High-frequency Therapy (HF10 Therapy) Is Superior to Traditional Low-frequency Spinal Cord Stimulation for the Treatment of Chronic Back and Leg Pain," *J. Am. Soc. Anesthesiol.*, vol. 123, no. 4, pp. 851–860, 2015.
[41] M. Russo *et al.*, "Sustained long-term outcomes with closed-loop spinal cord stimulation: 12-month results of the prospective, multicenter, open-label avalon study," *Neurosurgery*, vol. 87, no. 4, pp. E485–E495, 2020, doi: 10.1093/neuros/nyaa003.
[42] N. Mekhail *et al.*, "Long-term safety and efficacy of closed-loop spinal cord stimulation to treat chronic back and leg pain (Evoke): a double-blind, randomised, controlled trial," *Lancet Neurol.*, vol. 19, no. 2, pp. 123–134, Feb. 2020, doi: 10.1016/S1474-4422(19)30414-4.
[43] S. F. Lempka, C. C. McIntyre, K. L. Kilgore, and A. G. Machado, "Computational analysis of kilohertz frequency spinal cord stimulation for chronic pain management.," *Anesthesiology*, vol. 122, no. 6, pp. 1362–76, 2015, doi:

10.1097/ALN.0000000000000649.
[44] D. De Ridder and S. Vanneste, “Burst and Tonic Spinal Cord Stimulation: Different and Common Brain Mechanisms,” 2015, doi: 10.1111/ner.12368.
[45] S. Ahmed, T. Yearwood, D. De Ridder, and S. Vanneste, “Burst and high frequency stimulation: underlying mechanism of action,” *Expert Review of Medical Devices*, vol. 15, no. 1. pp. 61–70, 2018, doi: 10.1080/17434440.2018.1418662.
[46] J. L. Parker, D. M. Karantonis, P. S. Single, M. Obradovic, and M. J. Cousins, “Compound action potentials recorded in the human spinal cord during neurostimulation for pain relief,” *Pain*, vol. 153, no. 3, pp. 593–601, Mar. 2012, doi: 10.1016/j.pain.2011.11.023.
[47] M. Russo *et al.*, “Effective Relief of Pain and Associated Symptoms With Closed-Loop Spinal Cord Stimulation System: Preliminary Results of the Avalon Study,” *Neuromodulation*, vol. 21, no. 1, pp. 38–47, 2018, doi: 10.1111/ner.12684.
[48] J. Parker, D. Karantonis, and P. Single, “Hypothesis for the mechanism of action of ECAP-controlled closed-loop systems for spinal cord stimulation,” *Healthc. Technol. Lett.*, vol. 7, no. 3, pp. 76–80, 2020, doi: 10.1049/htl.2019.0110.
[49] K. Chakravarthy, H. Bink, and D. Dinsmoor, “Sensing evoked compound action potentials from the spinal cord: Novel preclinical and clinical considerations for the pain management researcher and clinician,” *J. Pain Res.*, vol. 13, pp. 3269–3279, 2020, doi: 10.2147/JPR.S289098.
[50] G. E. Gmel, R. Santos Escapa, J. L. Parker, D. Mugan, A. Al-Kaisy, and S. Palmisani, “The Effect of Spinal Cord Stimulation Frequency on the Neural Response and Perceived Sensation in Patients With Chronic Pain,” *Front. Neurosci.*, vol. 15, no. January, pp. 1–8, 2021, doi: 10.3389/fnins.2021.625835.
[51] F. M. Maynard *et al.*, “International standards for neurological and functional classification of spinal cord injury,” *Spinal Cord*, vol. 35, no. 5, pp. 266–274, 1997, doi: 10.1038/sj.sc.3100432.
[52] L. A. Simpson, J. J. Eng, J. T. C. Hsieh, and D. L. Wolfe, “The health and life priorities of individuals with spinal cord injury: A systematic review,” *J. Neurotrauma*, vol. 29, no. 8, pp. 1548–1555, 2012, doi: 10.1089/neu.2011.2226.
[53] “Spinal Cord Injury Facts and Figures at a Glance 2020 SCI Data Sheet,” Birmingham, Alabama, 2020. Accessed: Jun. 01, 2021. [Online]. Available: www.msktc.org/sci/model-system-centers.
[54] M. A. Lane, K.-Z. Lee, D. D. Fuller, and P. J. Reier, “Spinal circuitry and respiratory recovery following spinal cord injury,” *Respir. Physiol. Neurobiol.*, vol. 169, no. 2, pp. 123–132, Nov. 2009, doi: 10.1016/J.RESP.2009.08.007.
[55] R. Brown, A. F. DiMarco, J. D. Hoit, and E. Garshick, “Respiratory dysfunction and management in spinal cord injury,” in *Respiratory Care*, 2006, vol. 51, no. 8, pp. 853–868.
[56] N. S. C. I. S. Center and National Spinal Cord Injury Statistical Center, “The 2019 Annual Statistical Report for the Spinal Cord Injury Model Systems,” p. 106, 2019.
[57] S. Sahetya, S. Allgood, P. C. Gay, and N. Lechtzin, “Long-Term Mechanical Ventilation,” doi: 10.1016/j.ccm.2016.07.014.
[58] M. A. Lane, “Spinal respiratory motoneurons and interneurons,” *Respir. Physiol. Neurobiol.*, vol. 179, no. 1, pp. 3–13, 2011, doi: 10.1016/j.resp.2011.07.004.
[59] J. T. Hachmann, P. J. Grahn, J. S. Calvert, D. I. Drubach, K. H. Lee, and I. A. Lavrov,

"Electrical Neuromodulation of the Respiratory System After Spinal Cord Injury," *Mayo Clin. Proc.*, vol. 92, no. 9, pp. 1401–1414, 2017, doi: 10.1016/j.mayocp.2017.04.011.
[60] A. De Troyer, P. A. Kirkwood, and T. A. Wilson, "Respiratory action of the intercostal muscles," *Physiol. Rev.*, vol. 85, no. 2, pp. 717–756, 2005, doi: 10.1152/physrev.00007.2004.
[61] W. W. L. Glenn, J. F. Hogan, J. S. O. Loke, T. E. Ciesielki, M. L. Phelps, and R. Rowedder, "Ventilatory Support by Pacing of the Conditioned Diaphragm in Quadriplegia," *Surv. Anesthesiol.*, vol. 29, no. 4, p. 209, 1985, doi: 10.1097/00132586-198508000-00003.
[62] A. F. DiMarco, R. P. Onders, A. Ignagni, K. E. Kowalski, and J. T. Mortimer, "Phrenic nerve pacing via intramuscular diaphragm electrodes in tetraplegic subjects," *Chest*, vol. 127, no. 2, pp. 671–678, 2005, doi: 10.1378/chest.127.2.671.
[63] S. Hirschfeld, G. Exner, T. Luukkaala, and G. A. Baer, "Mechanical ventilation or phrenic nerve stimulation for treatment of spinal cord injury-induced respiratory insufficiency," *Spinal Cord*, vol. 46, no. 11, pp. 738–742, 2008, doi: 10.1038/sc.2008.43.
[64] M. L. Gill *et al.*, "Neuromodulation of lumbosacral spinal networks enables independent stepping after complete paraplegia," *Nat. Med.*, vol. 24, no. 11, pp. 1677–1682, 2018, doi: 10.1038/s41591-018-0175-7.
[65] B. Barra *et al.*, "Selective Recruitment of Arm Motoneurons in Nonhuman Primates Using Epidural Electrical Stimulation of the Cervical Spinal Cord," in *Proceedings of the Annual International Conference of the IEEE Engineering in Medicine and Biology Society, EMBS*, Oct. 2018, vol. 2018-July, pp. 1424–1427, doi: 10.1109/EMBC.2018.8512554.
[66] K. E. Kowalski, J. R. Romaniuk, T. Kowalski, and A. F. DiMarco, "Effects of expiratory muscle activation via high-frequency spinal cord stimulation," *J. Appl. Physiol.*, vol. 123, no. 6, pp. 1525–1531, Dec. 2017, doi: 10.1152/japplphysiol.00402.2017.
[67] E. Formento *et al.*, "Electrical spinal cord stimulation must preserve proprioception to enable locomotion in humans with spinal cord injury," *Nat. Neurosci.*, vol. 21, no. 12, pp. 1728–1741, 2018, doi: 10.1038/s41593-018-0262-6.
[68] A. F. DiMarco and K. E. Kowalski, "High-frequency spinal cord stimulation of inspiratory muscles in dogs: A new method of inspiratory muscle pacing," *J. Appl. Physiol.*, vol. 107, no. 3, pp. 662–669, Sep. 2009, doi: 10.1152/japplphysiol.00252.2009.
[69] A. F. DiMarco and K. E. Kowalski, "Intercostal muscle pacing with high frequency spinal cord stimulation in dogs," *Respir. Physiol. Neurobiol.*, vol. 171, no. 3, pp. 218–224, 2010, doi: 10.1016/j.resp.2010.03.017.
[70] A. F. DiMarco and K. E. Kowalski, "Distribution of electrical activation to the external intercostal muscles during high frequency spinal cord stimulation in dogs," *J. Physiol.*, vol. 589, no. 6, pp. 1383–1395, 2011, doi: 10.1113/jphysiol.2010.199679.
[71] A. F. DiMarco and K. E. Kowalski, "High-frequency spinal cord stimulation in a subacute animal model of spinal cord injury," *Journal of Applied Physiology*, vol. 127, no. 1. pp. 98–102, 2019, doi: 10.1152/japplphysiol.00006.2019.
[72] A. De Troyer and A. M. Boriek, "Mechanics of the respiratory muscles," *Compr. Physiol.*, vol. 1, no. 3, pp. 1273–1300, 2011, doi: 10.1002/cphy.c100009.
[73] E. E. Decima, C. von Euler, and U. Thoden, "Spinal Intercostal-phrenic Reflexes," *Nature*, vol. 214, no. 5085, pp. 312–313, 1967.
[74] E. E. Decima, C. von Euler, and U. Thoden, "Intercostal-to-Phrenic Reflexes in the Spinal Cat," *Acta Physiol. Scand.*, vol. 75, no. 4, pp. 568–579, 1969, doi: 10.1111/j.1748-

1716.1969.tb04412.x.
[75] C. C. Mcintyre and T. J. Foutz, “Computational modeling of deep brain stimulation,” *Handb. Clin. Neurol.*, vol. 116, pp. 55–61, 2013, doi: 10.1016/B978-0-444-53497-2.00005-X.
[76] S. F. Lempka and C. C. McIntyre, “Theoretical Analysis of the Local Field Potential in Deep Brain Stimulation Applications,” *PLoS One*, vol. 8, no. 3, 2013, doi: 10.1371/journal.pone.0059839.
[77] R. D. Graham, T. M. Bruns, B. Duan, and S. F. Lempka, “Dorsal root ganglion stimulation for chronic pain modulates Aβ-fiber activity but not C-fiber activity: A computational modeling study,” *Clin. Neurophysiol.*, vol. 130, no. 6, pp. 941–951, Jun. 2019, doi: 10.1016/j.clinph.2019.02.016.
[78] Y. Ge *et al.*, “Mediating different-diameter Aβ nerve fibers using a biomimetic 3D TENS computational model,” *J. Neurosci. Methods*, vol. 346, 2020, doi: 10.1016/j.jneumeth.2020.108891.
[79] S. Bai, C. Loo, and S. Dokos, “A review of computational models of transcranial electrical stimulation,” *Crit. Rev. Biomed. Eng.*, vol. 41, no. 1, pp. 21–35, 2013, doi: 10.1615/CritRevBiomedEng.2013007163.
[80] A. P. Mourdoukoutas, D. Q. Truong, D. K. Adair, B. J. Simon, and M. Bikson, “High-Resolution Multi-Scale Computational Model for Non-Invasive Cervical Vagus Nerve Stimulation,” *Neuromodulation*, vol. 21, no. 3. Blackwell Publishing Inc., pp. 261–268, Apr. 01, 2018, doi: 10.1111/ner.12706.
[81] K. E. Finn, H. J. Zander, R. D. Graham, S. F. Lempka, and J. D. Weiland, “A Patient-Specific Computational Framework for the Argus II Implant,” *IEEE Open J. Eng. Med. Biol.*, vol. 1, pp. 190–196, 2020, doi: 10.1109/ojemb.2020.3001563.
[82] E. Mirzakhalili, B. Barra, M. Capogrosso, and S. F. Lempka, “Biophysics of Temporal Interference Stimulation,” *Cell Syst.*, vol. 11, no. 6, pp. 557-572.e5, 2020, doi: 10.1016/j.cels.2020.10.004.
[83] B. Coburn, “A Theoretical Study of Epidural Electrical Stimulation of the Spinal Cord - Part II: Effects on Long Myelinated Fibers,” *IEEE Trans. Biomed. Eng.*, vol. BME-32, no. 11, pp. 978–986, Nov. 1985, doi: 10.1109/TBME.1985.325649.
[84] B. Coburn, “Electrical stimulation of the spinal cord: two-dimensional finite element analysis with particular reference to epidural electrodes,” *Med. Biol. Eng. Comput.*, vol. 18, no. 5, pp. 573–584, Sep. 1980, doi: 10.1007/BF02443129.
[85] B. Coburn and W. K. Sin, “A Theoretical Study of Epidural Electrical Stimulation of the Spinal Cord Part I: Finite Element Analysis of Stimulus Fields,” *IEEE Trans. Biomed. Eng.*, vol. BME-32, no. 11, pp. 971–977, Nov. 1985, doi: 10.1109/TBME.1985.325648.
[86] J. Holsheimer and J. J. Struijk, “How do geometric factors influence epidural spinal cord stimulation? A quantitative analysis by computer modeling,” *Stereotact. Funct. Neurosurg.*, vol. 56, no. 4, pp. 234–249, 1991, doi: 10.1159/000099410.
[87] J. J. Struijk and J. Holsheimer, “Transverse tripolar spinal cord stimulation: Theoretical performance of a dual channel system,” *Med. Biol. Eng. Comput.*, vol. 34, no. 4, pp. 273–279, 1996, doi: 10.1007/BF02511237.
[88] J. J. Struijk, J. Holsheimer, G. G. van der Heide, and H. B. K. Boom, “Recruitment of Dorsal Column Fibers in Spinal Cord Stimulation: Influence of Collateral Branching,” *IEEE Trans. Biomed. Eng.*, vol. 39, no. 9, pp. 903–912, 1992, doi: 10.1109/10.256423.
[89] J. Holsheimer and W. A. Wesselink, “Effect of anode-cathode configuration on

paresthesia coverage in spinal cord stimulation," *Neurosurgery*, vol. 41, no. 3, pp. 654–660, 1997, doi: 10.1097/00006123-199709000-00030.
[90] D. Lee, B. Hershey, K. Bradley, and T. Yearwood, "Predicted effects of pulse width programming in spinal cord stimulation: A mathematical modeling study," *Med. Biol. Eng. Comput.*, vol. 49, no. 7, pp. 765–774, Jul. 2011, doi: 10.1007/s11517-011-0780-9.
[91] D. Lee, E. Gillespie, and K. Bradley, "Dorsal column steerability with dual parallel leads using dedicated power sources: A computational model," *J. Vis. Exp.*, no. 48, Feb. 2010, doi: 10.3791/2443.
[92] B. Howell, S. P. Lad, and W. M. Grill, "Evaluation of intradural stimulation efficiency and selectivity in a computational model of spinal cord stimulation," *PLoS One*, vol. 9, no. 12, p. e114938, 2014, doi: 10.1371/journal.pone.0114938.
[93] V. Sankarasubramanian, J. R. Buitenweg, J. Holsheimer, and P. Veltink, "Triple leads programmed to perform as longitudinal guarded cathodes in spinal cord stimulation: A modeling study," *Neuromodulation*, vol. 14, no. 5, pp. 401–410, 2011, doi: 10.1111/j.1525-1403.2011.00383.x.
[94] S. F. Lempka, H. J. Zander, C. J. Anaya, A. Wyant, J. G. Ozinga, and A. G. Machado, "Patient-Specific Analysis of Neural Activation During Spinal Cord Stimulation for Pain," *Neuromodulation*, vol. 23, no. 5, pp. 572–581, Aug. 2020, doi: 10.1111/ner.13037.
[95] N. Khadka *et al.*, "Realistic anatomically detailed open-source spinal cord stimulation (RADO-SCS) model," *J. Neural Eng.*, vol. 17, no. 2, p. 026033, Apr. 2020, doi: 10.1088/1741-2552/ab8344.
[96] A. F. DiMarco and K. E. Kowalski, "Spinal pathways mediating phrenic activation during high frequency spinal cord stimulation," *Respir. Physiol. Neurobiol.*, vol. 186, no. 1, pp. 1–6, 2013, doi: 10.1016/j.resp.2012.12.003.
[97] H. J. Zander, R. D. Graham, C. J. Anaya, and S. F. Lempka, "Anatomical and technical factors affecting the neural response to epidural spinal cord stimulation," *J. Neural Eng.*, vol. 17, no. 3, 2020, doi: 10.1088/1741-2552/ab8fc4.
[98] S. J. Nagel *et al.*, "Spinal Cord Stimulation for Spasticity: Historical Approaches, Current Status, and Future Directions," *Neuromodulation*, vol. 20, no. 4. John Wiley & Sons, Ltd (10.1111), pp. 307–321, Jun. 01, 2017, doi: 10.1111/ner.12591.
[99] J. Holsheimer, J. J. Struijk, and N. R. Tas, "Effects of Electrode Geometry and Combination on Nerve-Fiber Selectivity in Spinal-Cord Stimulation," *Med. Biol. Eng. Comput.*, vol. 33, no. September, pp. 676–682, 1995, doi: 10.1007/BF02510785.
[100] J. Holsheimer and W. A. Wesselink, "Optimum electrode geometry for spinal cord stimulation: the narrow bipole and tripole," *Med. Biol. Eng. Comput*, vol. 35, pp. 493–497, 1997, Accessed: Jun. 20, 2018. [Online]. Available: https://link.springer.com/content/pdf/10.1007/BF02525529.pdf.
[101] V. Sankarasubramanian *et al.*, "Objective Measures to Characterize the Physiological Effects of Spinal Cord Stimulation in Neuropathic Pain: A Literature Review," *Neuromodulation*, vol. 22, no. 2. pp. 127–148, 2019, doi: 10.1111/ner.12804.
[102] J. H. Laird and J. L. Parker, "A model of evoked potentials in spinal cord stimulation," *Proc. Annu. Int. Conf. IEEE Eng. Med. Biol. Soc. EMBS*, pp. 6555–6558, 2013, doi: 10.1109/EMBC.2013.6611057.
[103] J. E. Arle, K. W. Carlson, L. Mei, and J. L. Shils, "Modeling effects of scar on patterns of dorsal column stimulation," *Neuromodulation*, vol. 17, no. 4, pp. 320–333, Jun. 2014, doi: 10.1111/ner.12128.

[104] G. R. Hernández-Labrado, J. L. Polo, E. López-Dolado, and J. E. Collazos-Castro, “Spinal cord direct current stimulation: finite element analysis of the electric field and current density,” *Med. Biol. Eng. Comput.*, vol. 49, no. 7, pp. 417–429, 2011, doi: 10.1007/s11517-011-0756-9.
[105] C. J. Anaya, H. J. Zander, R. D. Graham, V. Sankarasubramanian, and S. F. Lempka, “Evoked Potentials Recorded From the Spinal Cord During Neurostimulation for Pain: A Computational Modeling Study,” *Neuromodulation*, vol. 23, no. 1, pp. 64–73, Jun. 2020, doi: 10.1111/ner.12965.
[106] T. Kameyama, Y. Hashizume, and G. Sobue, “Morphologic features of the normal human cadaveric spinal cord,” *Spine (Phila. Pa. 1976).*, vol. 21, no. 11, pp. 1285–1290, 1996, doi: 10.1097/00007632-199606010-00001.
[107] J. H. Kim, C. W. Lee, K. S. Chun, W. H. Shin, H. G. Bae, and J. C. Chang, “Morphometric relationship between the cervicothoracic cord segments and vertebral bodies,” *J. Korean Neurosurg. Soc.*, vol. 52, no. 4, pp. 384–390, 2012, doi: 10.3340/jkns.2012.52.4.384.
[108] M. Bozkurt *et al.*, “Microsurgical anatomy of the dorsal thoracic rootlets and dorsal root entry zones,” *Acta Neurochir. (Wien).*, vol. 154, no. 7, pp. 1235–1239, 2012, doi: 10.1007/s00701-012-1395-0.
[109] Ö. Kirazlı *et al.*, “Anatomy of the spinal dorsal root entry zone: its clinical significance,” *Acta Neurochir. (Wien).*, vol. 156, no. 12, pp. 2351–2358, 2014, doi: 10.1007/s00701-014-2252-0.
[110] Y. Kanpolat, H. Tuna, M. Bozkurt, and A. H. Elhan, “Spinal and Nucleus Caudalis Dorsal Root Entry Zone Operations for Chronic Pain,” *Neurosurgery*, vol. 62, no. March, pp. 235–244, 2008, doi: 10.1007/s00701-012-1395-0.
[111] J. Struijk, J. Holsheimer, and H. B. K. Boom, “Excitation of dorsal root fibers in SCS: A theoretical study,” *IEEE Trans. Biomed. Eng.*, vol. 40, no. 7, pp. 632–639, 1993, [Online]. Available: https://doi.org/10.1109/10.237693.
[112] M. A. Reina, C. D. Franco, A. López, J. A. Dé Andrés, and A. van Zundert, “Clinical implications of epidural fat in the spinal canal. A scanning electron microscopic study,” *Acta Anaesthesiol. Belg.*, vol. 60, no. 1, pp. 7–17, 2009.
[113] W. M. Grill and T. J. Mortimer, “Electrical properties of implant encapsulation tissue,” *Ann. Biomed. Eng.*, vol. 22, no. 1, pp. 23–33, Jan. 1994, doi: 10.1007/BF02368219.
[114] M. M. Panjabi *et al.*, “Thoracic Human Vertebrae Quantitative Three-Dimensional Anatomy,” *Spine (Phila. Pa. 1976).*, vol. 16, no. 8, pp. 888–901, 1991, doi: 10.1097/00007632-199108000-00006.
[115] C. E. Tschirhart, J. A. Finkelstein, and C. M. Whyne, “Biomechanics of vertebral level, geometry, and transcortical tumors in the metastatic spine,” *J. Biomech.*, vol. 40, no. 1, pp. 46–54, 2007, doi: 10.1016/j.jbiomech.2005.11.014.
[116] I. A. Kapandji, *The physiology of the joints: annotated diagrams of the mechanics of the human joints, Volume 3: The Trunk and the Vertebral Column.* 1987.
[117] M. C. Kao *et al.*, “Prediction of the distance from skin to epidural space for low-thoracic catheter insertion by computed tomography,” *Br. J. Anaesth.*, vol. 92, no. 2, pp. 271–273, 2004, doi: 10.1093/bja/aeh053.
[118] A. Pickard, M. Darby, and J. Soar, “Radiological assessment of the adult chest: Implications for chest compressions,” *Resuscitation*, vol. 71, no. 3, pp. 387–390, 2006, doi: 10.1016/j.resuscitation.2006.04.012.

[119] K. H. Kilburn and T. Asmundsson, “Anteroposterior Chest Diameter in Emphysema,” *Arch Intern Med*, vol. 123, 1969.
[120] L. A. Geddes and L. E. Baker, “The specific resistance of biological material—A compendium of data for the biomedical engineer and physiologist,” *Med. Biol. Eng.*, vol. 5, no. 3, pp. 271–293, 1967, doi: 10.1007/BF02474537.
[121] S. Gabriel, R. W. Lau, and C. Gabriel, “The dielectric properties of biological tissues: II. Measurements in the frequency range 10 Hz to 20 GHz,” *Phys. Med. Biol.*, vol. 41, no. 11, pp. 2251–2269, 1996, doi: 10.1088/0031-9155/41/11/002.
[122] F. Rattay, S. M. Danner, U. S. Hofstoetter, and K. Minassian, “Finite Element Modeling for Extracellular Stimulation,” in *Encyclopedia of Computational Neuroscience*, 2014, pp. 1–12.
[123] F. Rattay, “The basic mechanism for the electrical stimulation of the nervous system,” *Neuroscience*, vol. 89, no. 2, pp. 335–346, 1999, doi: 10.1016/S0306-4522(98)00330-3.
[124] F. Rattay, “Electrical Nerve Stimulation: Theory, Experiments, and Applications - Back Matter,” in *Electrical Nerve Stimulation: Theory, Experiments, and Applications*, Vienna: Springer-Verlag Wien, 1990, pp. 241–264.
[125] E. J. Peterson, O. Izad, and D. J. Tyler, “Predicting myelinated axon activation using spatial characteristics of the extracellular field,” in *Journal of Neural Engineering*, 2011, vol. 8, no. 4, doi: 10.1088/1741-2560/8/4/046030.
[126] B. Howell, K. Gunalan, and C. C. McIntyre, “A Driving-Force Predictor for Estimating Pathway Activation in Patient-Specific Models of Deep Brain Stimulation,” *Neuromodulation*, vol. 22, no. 4, pp. 403–415, Jun. 2019, doi: 10.1111/ner.12929.
[127] C. C. McIntyre, A. G. Richardson, and W. M. Grill, “Modeling the Excitability of Mammalian Nerve Fibers: Influence of Afterpotentials on the Recovery Cycle,” *J. Neurophysiol.*, vol. 87, no. 2, pp. 995–1006, 2002, doi: 10.1152/jn.00353.2001.
[128] J. Howells, L. Trevillion, H. Bostock, and D. Burke, “The voltage dependence of I h in human myelinated axons,” *J. Physiol.*, vol. 590, no. 7, pp. 1625–1640, Apr. 2012, doi: 10.1113/jphysiol.2011.225573.
[129] J. Gaines, K. Finn, J. Slopsema, L. Heyboer, and K. Polasek, “A model of median nerve activation using surface electrical stimulation,” *J. Comput. Neurosci.*, vol. Accepted P, no. 1, pp. 29–43, Aug. 2018, doi: 10.1007/s10827-018-0689-5.
[130] S. Lloyd, “Least squares quantization in PCM,” *IEEE Trans. Inf. Theory*, vol. 28, no. 2, pp. 129–137, Mar. 1982, doi: 10.1109/TIT.1982.1056489.
[131] Q. Du and M. Gunzburger, “Grid generation and optimization based on centroidal Voronoi tessellations,” *Appl. Math. Comput.*, vol. 133, no. 2–3, pp. 591–607, 2002, doi: 10.1016/S0096-3003(01)00260-0.
[132] J. E. Desmedt and G. Cheron, “Central somatosensory conduction in man: Neural generators and interpeak latencies of the far-field components recorded from neck and right or left scalp and earlobes,” *Electroencephalogr. Clin. Neurophysiol.*, vol. 50, no. 5–6, pp. 382–403, Dec. 1980, doi: 10.1016/0013-4694(80)90006-1.
[133] N. T. Carnevale and M. L. Hines, *The NEURON BOOK*. Cambridge, UK: Campridge University Press, 2006.
[134] A. F. Reynolds and A. G. Shetter, “Scarring around cervical epidural stimulating electrode,” *Neurosurgery*, vol. 13, no. 1, pp. 63–65, 1983, doi: 10.1227/00006123-198307000-00013.
[135] P. Dam-Hieu, E. Magro, R. Seizeur, A. Simon, and B. Quinio, “Cervical cord

compression due to delayed scarring around epidural electrodes used in spinal cord stimulation," *J. Neurosurg. Spine*, vol. 12, no. 4, pp. 409–412, 2011, doi: 10.3171/2009.10.spine09193.
[136] J. L. Parker *et al.*, "Electrically Evoked Compound Action Potentials Recorded From the Sheep Spinal Cord," *Neuromodulation Technol. Neural Interface*, vol. 16, no. 4, pp. 295–303, Jul. 2013, doi: 10.1111/ner.12053.
[137] L. Manola, J. Holsheimer, and P. Veltink, "Technical performance of percutaneous leads for spinal cord stimulation: A modeling study," *Neuromodulation*, vol. 8, no. 2, pp. 88–99, Apr. 2005, doi: 10.1111/j.1525-1403.2005.00224.x.
[138] F. Rattay, T. Wien, K. Minassian, and M. R. Dimitrijevic, "Epidural electrical stimulation of posterior structures of the human lumbosacral cord: 2. Quantitative analysis by computer modeling," *Spinal Cord*, vol. 38, pp. 473–489, 2000, doi: 10.1038/sj.sc.3101039.
[139] S. J. Nagel *et al.*, "Spinal dura mater: biophysical characteristics relevant to medical device development," *J. Med. Eng. Technol.*, vol. 42, no. 2, pp. 128–139, 2018, doi: 10.1080/03091902.2018.1435745.
[140] J. Struijk, J. Holsheimer, G. Barolat, J. He, and H. B. K. Boom, "Paresthesia Thresholds in Spinal Cord Stimulation: A Comparison of Theoretical Results with Clinical Data," *IEEE Trans. Rehabil. Eng.*, vol. 1, no. 2, pp. 101–108, Jun. 1993, doi: 10.1109/86.242424.
[141] J. L. Durá, C. Solanes, J. De Andrés, and J. Saiz, "Computational Study of the Effect of Electrode Polarity on Neural Activation Related to Paresthesia Coverage in Spinal Cord Stimulation Therapy," *Neuromodulation*, vol. 22, no. 3, pp. 269–279, Apr. 2019, doi: 10.1111/ner.12909.
[142] V. Sankarasubramanian, J. R. Buitenweg, J. Holsheimer, and P. H. Veltink, "Staggered transverse tripoles with quadripolar lateral anodes using percutaneous and surgical leads in spinal cord stimulation," *Neurosurgery*, vol. 72, no. 3, pp. 483–491, 2013, doi: 10.1227/NEU.0b013e31827d0e12.
[143] C. R. Butson and C. C. McIntyre, "Tissue and electrode capacitance reduce neural activation volumes during deep brain stimulation," *Clin. Neurophysiol.*, vol. 116, no. 10, pp. 2490–2500, Oct. 2005, doi: 10.1016/j.clinph.2005.06.023.
[144] C. A. Bossetti, M. J. Birdno, and W. M. Grill, "Analysis of the quasi-static approximation for calculating potentials generated by neural stimulation," *J. Neural Eng.*, vol. 5, no. 1, pp. 44–53, Mar. 2008, doi: 10.1088/1741-2560/5/1/005.
[145] R. Plonsey and D. B. Heppner, "Considerations of quasi-stationarity in electrophysiological systems," *Bull. Math. Biophys.*, vol. 29, no. 4, pp. 657–664, 1967, doi: 10.1007/BF02476917.
[146] M. Russo and J.-P. Van Buyten, "10-kHz High-Frequency SCS Therapy: A Clinical Summary," *Pain Med. (United States)*, vol. 16, no. 5, pp. 934–942, 2015, doi: 10.1111/pme.12266.
[147] S. Gabriel, R. W. Lau, and C. Gabriel, "The dielectric properties of biological tissues: III. Parametric models for the dielectric spectrum of tissues," *Phys. Med. Biol.*, vol. 41, no. 11, pp. 2271–2293, 1996, doi: 10.1088/0031-9155/41/11/003.
[148] T. L. Yearwood, B. Hershey, K. Bradley, and D. Lee, "Pulse width programming in spinal cord stimulation: A clinical study," *Pain Physician*, vol. 13, no. 4, pp. 321–335, 2010, doi: 10.36076/ppj.2010/13/321.
[149] S. F. Lempka, M. D. Johnson, S. Miocinovic, J. L. Vitek, and C. C. McIntyre, "Current-

controlled deep brain stimulation reduces in vivo voltage fluctuations observed during voltage-controlled stimulation," *Clin. Neurophysiol.*, vol. 121, no. 12, pp. 2128–2133, Dec. 2010, doi: 10.1016/j.clinph.2010.04.026.
[150] R. B. North, D. H. Kidd, F. Farrokhi, and S. A. Piantadosi, "Spinal cord stimulation versus repeated lumbosacral spine surgery for chronic pain: A randomized, controlled trial," *Neurosurgery*, vol. 56, no. 1, pp. 98–106, 2005, doi: 10.1227/01.NEU.0000144839.65524.E0.
[151] B. Howell, L. E. Medina, and W. M. Grill, "Effects of frequency-dependent membrane capacitance on neural excitability," *J. Neural Eng.*, vol. 12, no. 5, p. 56015, 2015, doi: 10.1088/1741-2560/12/5/056015.
[152] S. J. Thomson *et al.*, "Effects of Rate on Analgesia in Kilohertz Frequency Spinal Cord Stimulation: Results of the PROCO Randomized Controlled Trial," *Neuromodulation*, vol. 21, no. 1, pp. 67–76, 2018, doi: 10.1111/ner.12746.
[153] W. Awwad *et al.*, "Analysis of the spinal nerve roots in relation to the adjacent vertebral bodies with respect to a posterolateral vertebral body replacement procedure," *J. Craniovertebral Junction Spine*, vol. 8, no. 1, pp. 50–57, 2017, doi: 10.4103/0974-8237.199869.
[154] R. S. Tubbs *et al.*, "Meningeal relationships to the spinal nerves and rootlets: a gross, histological, and radiological study with application to intradural extramedullary spinal tumors," *Child's Nerv. Syst.*, vol. 31, no. 5, pp. 675–681, 2015, doi: 10.1007/s00381-015-2648-z.
[155] Y. Liu, X. Zhou, J. Ma, Y. Ge, and X. Cao, "The diameters and number of nerve fibers in spinal nerve roots," *J. Spinal Cord Med.*, vol. 38, no. 4, pp. 532–537, Jul. 2015, doi: 10.1179/1079026814Z.000000000273.
[156] W. Pallie, "The Intersegmental Anastomoses of Posterior Spinal Rootlets and Their Significance," *J. Neurosurg.*, vol. 16, no. 2, pp. 188–196, 1959, doi: 10.3171/jns.1959.16.2.0188.
[157] A. Karatas, S. Caglar, A. Savas, A. H. Elhan, and A. Erdogan, "Microsurgical anatomy of the dorsal cervical rootlets and dorsal root entry zones," *Acta Neurochir. (Wien).*, vol. 147, no. 2, pp. 195–199, 2005, doi: 10.1007/s00701-004-0425-y.
[158] J. D. Law, "Spinal stimulation: Statistical superiority of monophasic stimulation of narrowly separated, longitudinal bipoles having rostral cathodes," *Appl. Neurophysiol.*, vol. 46, no. 1–4, pp. 129–137, 1983, doi: 10.1159/000101252.
[159] G. Barolat, S. Zeme, and B. Ketcik, "Multifactorial analysis of epidural spinal cord stimulation," *Stereotact. Funct. Neurosurg.*, vol. 56, no. 2, pp. 77–103, 1991, doi: 10.1159/000099395.
[160] A. L. Zannou, N. Khadka, M. FallahRad, D. Q. Truong, B. H. Kopell, and M. Bikson, "Tissue Temperature Increases by a 10 kHz Spinal Cord Stimulation System: Phantom and Bioheat Model," *Neuromodulation*, vol. 2019, 2019, doi: 10.1111/ner.12980.
[161] N. D. Crosby, J. J. Janik, and W. M. Grill, "Modulation of activity and conduction in single dorsal column axons by kilohertz-frequency spinal cord stimulation," *J. Neurophysiol.*, vol. 117, no. 1, pp. 136–147, 2017, doi: 10.1152/jn.00701.2016.
[162] Z. Song, H. Viisanen, B. A. Meyerson, A. Pertovaara, and B. Linderoth, "Efficacy of Kilohertz-Frequency and Conventional Spinal Cord Stimulation in Rat Models of Different Pain Conditions," *Neuromodulation Technol. Neural Interface*, vol. 17, no. 3, pp. 226–235, 2014, doi: 10.1111/ner.12161.

[163] K. Chakravarthy, H. Richter, P. J. Christo, K. Williams, and Y. Guan, “Spinal Cord Stimulation for Treating Chronic Pain: Reviewing Preclinical and Clinical Data on Paresthesia-Free High-Frequency Therapy,” *Neuromodulation*, vol. 21, no. 1, pp. 10–18, 2018, doi: 10.1111/ner.12721.
[164] J. Caylor *et al.*, “Spinal cord stimulation in chronic pain: evidence and theory for mechanisms of action,” *Bioelectron. Med.*, vol. 5, no. 1, pp. 1–41, 2019, doi: 10.1186/s42234-019-0023-1.
[165] L. Manola and J. Holsheimer, “Technical performance of percutaneous and laminectomy leads analyzed by modeling,” *Neuromodulation*, vol. 7, no. 4, pp. 231–241, 2004, doi: 10.1111/j.1094-7159.2004.04207.x.
[166] S. M. Danner, U. S. Hofstoetter, J. Ladenbauer, F. Rattay, and K. Minassian, “Can the Human Lumbar Posterior Columns Be Stimulated by Transcutaneous Spinal Cord Stimulation? A Modeling Study,” *Artif. Organs*, vol. 35, no. 3, pp. 257–262, 2011, doi: 10.1111/j.1525-1594.2011.01213.x.
[167] W. A. Wesselink, J. Holsheimer, and H. B. K. Boom, “Analysis of current density and related parameters in spinal cord stimulation,” *IEEE Trans. Rehabil. Eng.*, vol. 6, no. 2, pp. 200–207, Jun. 1998, doi: 10.1109/86.681186.
[168] H. J. Zander, K. E. Kowalski, A. F. DiMarco, and S. F. Lempka, “Model-Based Optimization of Spinal Cord Stimulation for Inspiratory Muscle Activation,” *Neuromodulation Technol. Neural Interface*, 2021, doi: 10.1111/ner.13415.
[169] E. E. Decima and C. von Euler, “Intercostal and Cerebellar Influences on Efferent Phrenic Activity in the Decerebrate Cat,” *Acta Physiol. Scand.*, vol. 76, no. 1–2, pp. 148–158, 1969, doi: 10.1111/j.1748-1716.1969.tb04459.x.
[170] T. F. Fletcher, H. E. Evans, and A. De Lahunta, “Miller’s Anatomy of the Dog.,” 4th ed., Elsevier Health Sciences, 2013, p. 871.
[171] I. Dabanoglu, M. E. Kara, and M. K. Ocal, “Normal morphometry of the thoracic aorta in the German shepherd dog: A computed tomographic study,” *J. Vet. Med. Ser. C Anat. Histol. Embryol.*, vol. 33, no. 3, pp. 53–58, 2003, doi: 10.1111/j.1439-0264.2006.00717.x.
[172] R. Berguer, J. Porto, B. Fedoronko, and L. Dragovic, “Selective deep hypothermia of the spinal cord prevents paraplegia after aortic cross-clamping in the dog model,” *J. Vasc. Surg.*, vol. 15, no. 1, pp. 62–72, 1992, doi: 10.1016/0741-5214(92)70014-C.
[173] C. Persson, J. Summers, and R. M. Hall, “The effect of cerebrospinal fluid thickness on traumatic spinal cord deformation,” *J. Appl. Biomech.*, vol. 27, no. 4, pp. 330–335, 2011, doi: 10.1123/jab.27.4.330.
[174] J. De Andres, M. A. Reina, J. M. Hernandez, A. Carrera, A. Oliva, and A. Prats-Galino, “Role of spinal anatomical structures for neuromodulation,” *Reg. Anesth. Pain Med.*, vol. 36, no. 5, pp. E130–E137, 2011, Accessed: May 17, 2017. [Online]. Available: http://www.embase.com/search/results?subaction=viewrecord&from=export&id=L70735558%5Cnhttp://sfx.library.uu.nl/utrecht?sid=EMBASE&issn=10987339&id=doi:&atitle=Role+of+spinal+anatomical+structures+for+neuromodulation&stitle=Reg.+Anesth.+Pain+Med.&title=Reg.
[175] S. A. Saywell, T. W. Ford, C. F. Meehan, A. J. Todd, and P. A. Kirkwood, “Electrophysiological and Morphological Characterization of Propriospinal Interneurons in the Thoracic Spinal Cord,” *J. Neurophysiol.*, vol. 105, no. 2, pp. 806–826, Feb. 2011, doi: 10.1152/jn.00738.2010.
[176] J. Lipski and R. L. Martin-body, “Morphological properties of respiratory intercostal

motoneurons in cats as revealed by intracellular injection of horseradish peroxidase," *J. Comp. Neurol.*, vol. 260, no. 3, pp. 423–434, 1987, doi: 10.1002/cne.902600308.
[177] C. F. Meehan *et al.*, "Rostrocaudal Distribution of Motoneurones and Variation in Ventral Horn Area within a Segment of the Feline Thoracic Spinal Cord," *J. Comp. Neurol.*, vol. 472, no. 3, pp. 281–291, 2004, doi: 10.1002/cne.20096.
[178] N. Larnicol, D. Rose, D. Marlot, and B. Duron, "Spinal localization of the intercostal motoneurones innervating the upper thoracic spaces," *Neurosci. Lett.*, vol. 31, no. 1, pp. 13–18, 1982, doi: 10.1016/0304-3940(82)90046-5.
[179] N. Larnicol, D. Rose, D. Marlot, and B. Duron, "Anatomical organization of cat intercostal motor nuclei as demonstrated by HRP retrograde labelling," *J. Physiol. (Paris).*, vol. 78, no. 2, pp. 198–206, 1982.
[180] T. F. Fletcher and University of Minnesota College of Veterinary Medicine, "University of Minnesota Veterinary Anatomy - Spinal Cord Anatomy Lab," 2006. http://vanat.cvm.umn.edu/neurLab2/index.html (accessed Dec. 10, 2020).
[181] N. Greiner *et al.*, "Recruitment of upper-limb motoneurons with epidural electrical stimulation of the primate cervical spinal cord," *bioRxiv*, 2020, doi: 10.1101/2020.02.17.952796.
[182] A. F. DiMarco, G. S. Supinski, and K. Budzinska, "Inspiratory muscle interaction in the generation of changes in airway pressure," *J. Appl. Physiol.*, vol. 66, no. 6, pp. 2573–2578, 1989, doi: 10.1152/jappl.1989.66.6.2573.
[183] C. N. Shealy, J. T. Mortimer, and J. B. Reswick, "Electrical inhibition of pain by stimulation of the dorsal columns: preliminary clinical report.," *Anesth. Analg.*, vol. 46, no. 4, pp. 489–491, 1967, Accessed: Apr. 08, 2018. [Online]. Available: http://schmerzzentrum.ch/newsletter/2006-05/artikel-zu-cord-stimulation/shealy.pdf.
[184] T. C. Zhang, J. J. Janik, and W. M. Grill, "Modeling effects of spinal cord stimulation on wide-dynamic range dorsal horn neurons: influence of stimulation frequency and GABAergic inhibition," *J. Neurophysiol.*, vol. 112, no. 3, pp. 552–567, 2014, doi: 10.1152/jn.00254.2014.
[185] C. Ertekin, "Studies on the Human Evoked Electrospinogram: I. the Origin of the Segmental Evoked Potentials," *Acta Neurol. Scand.*, vol. 53, no. 1, pp. 3–20, 1976, doi: 10.1111/j.1600-0404.1976.tb04321.x.
[186] C. Ertekin, "Studies on the Human Evoked Electrospinogram: II. the Conduction Velocity along the Dorsal Funiculus," *Acta Neurol. Scand.*, vol. 53, no. 1, pp. 21–38, 1976, doi: 10.1111/j.1600-0404.1976.tb04322.x.
[187] Y. Maruyama, K. Shimoji, H. Shimizu, H. Kuribayashi, and H. Fujioka, "Human spinal cord potentials evoked by different sources of stimulation and conduction velocities along the cord," *J. Neurophysiol.*, vol. 48, no. 5, pp. 1098–1107, 1982, doi: 10.1152/jn.1982.48.5.1098.
[188] J. C. Olin, D. H. Kidd, and R. B. North, "Postural changes in spinal cord stimulation perceptual thresholds," *Neuromodulation*, vol. 1, no. 4, pp. 171–175, 1998, doi: 10.1111/j.1525-1403.1998.tb00013.x.
[189] J. L. Parker, J. Laird-Wah, and M. J. Cousins, "Comparison of a simple model of dorsal column axons with the electrically evoked compound action potential," *Bioelectron. Med.*, vol. 1, no. 2, pp. 117–130, 2018, doi: 10.2217/bem-2017-0006.
[190] M. L. Hines, A. P. Davison, and E. Muller, "NEURON and Python," *Front. Neuroinform.*, vol. 3, no. JAN, pp. 1–12, 2009, doi: 10.3389/neuro.11.001.2009.

[191] J. Towns *et al.*, "XSEDE: Accelerating scientific discovery," *Comput. Sci. Eng.*, vol. 16, no. 5, pp. 62–74, Sep. 2014, doi: 10.1109/MCSE.2014.80.
[192] M. A. Moffitt and C. C. McIntyre, "Model-based analysis of cortical recording with silicon microelectrodes," *Clin. Neurophysiol.*, vol. 116, no. 9, pp. 2240–2250, 2005, doi: 10.1016/j.clinph.2005.05.018.
[193] S. F. Lempka, M. D. Johnson, M. A. Moffitt, K. J. Otto, D. R. Kipke, and C. C. McIntyre, "Theoretical analysis of intracortical microelectrode recordings," *J. Neural Eng.*, vol. 8, no. 4, p. 45006, 2011, doi: 10.1088/1741-2560/8/4/045006.
[194] J. J. Briaire and J. H. M. Frijns, "Unraveling the electrically evoked compound action potential," *Hear. Res.*, vol. 205, no. 1–2, pp. 143–156, 2005, doi: 10.1016/j.heares.2005.03.020.
[195] A. R. Kent and W. M. Grill, "Analysis of deep brain stimulation electrode characteristics for neural recording," *J. Neural Eng.*, vol. 11, no. 4, 2014, doi: 10.1088/1741-2560/11/4/046010.
[196] J. He, G. Barolat, and B. Ketcik, "Stimulation Usage Range for Chronic Pain Management," *Analgesia*, vol. 1, no. 1, pp. 75–80, Sep. 1994, doi: 10.3727/107156994819564401.
[197] J. He, G. Barolat, J. Holsheimer, and J. J. Struijk, "Perception threshold and electrode position for spinal cord stimulation," *Pain*, vol. 59, no. 1, pp. 55–63, Oct. 1994, doi: 10.1016/0304-3959(94)90047-7.
[198] S. F. Lempka, H. J. Zander, C. J. Anaya, A. Wyant, J. G. Ozinga, and A. G. Machado, "Model-based analysis of spinal cord stimulation for chronic pain," in *Biosystems and Biorobotics*, vol. 21, Springer, Cham, 2019, pp. 39–43.
[199] E. T. Zhang, M. H. Ossipov, D. Q. Zhang, J. Lai, and F. Porreca, "Nerve injury-induced tactile allodynia is present in the absence of FOS labeling in retrogradely labeled post-synaptic dorsal column neurons," *Pain*, vol. 129, no. 1–2, pp. 143–154, 2007, doi: 10.1016/j.pain.2006.10.009.
[200] V. E. Abraira *et al.*, "The Cellular and Synaptic Architecture of the Mechanosensory Dorsal Horn," *Cell*, vol. 168, no. 1–2, pp. 295-310.e19, 2017, doi: 10.1016/j.cell.2016.12.010.
[201] S. Palmisani, G. E. Gmel, R. Santos Escapa, D. Mugan, A. Al-Kaisy, and J. Parker, "Neurophysiology of the Human Spinal Cord in Patients with Chronic Neuropathic Pain during SCS," *Presentation; NANS 2020 annual meeting*. 2020.
[202] F. B. Wagner *et al.*, "Targeted neurotechnology restores walking in humans with spinal cord injury," *Nature*, vol. 563, no. 7729, pp. 65–93, 2018, doi: 10.1038/s41586-018-0649-2.
[203] C. A. Angeli *et al.*, "Recovery of Over-Ground Walking after Chronic Motor Complete Spinal Cord Injury," *N. Engl. J. Med.*, vol. 379, no. 13, pp. 1244–1250, 2018, doi: 10.1056/nejmoa1803588.
[204] S. Furman, S. K. Koerner, D. J. Escher, A. J. Papowitz, J. Benjamin, and P. Tarjan, "Transvenous stimulation of the phrenic nerves.," *J. Thorac. Cardiovasc. Surg.*, vol. 62, no. 5, pp. 743–751, 1971, doi: 10.1016/s0022-5223(19)42004-7.
[205] A. F. DiMarco, K. E. Kowalski, G. Supinski, and J. R. Romaniuk, "Mechanism of expiratory muscle activation during lower thoracic spinal cord stimulation," *J. Appl. Physiol.*, vol. 92, no. 6, pp. 2341–2346, 2002, doi: 10.1152/japplphysiol.01231.2001.
[206] A. F. DiMarco, R. T. Geertman, K. Tabbaa, G. A. Nemunaitis, and K. E. Kowalski,

"Restoration of cough via spinal cord stimulation improves pulmonary function in tetraplegics," *J. Spinal Cord Med.*, vol. 43, no. 5, pp. 579–585, 2020, doi: 10.1080/10790268.2019.1699678.
[207] S. Gottlieb, "How FDA Plans to Help Consumers Capitalize on Advances in Science," 2017. https://www.fda.gov/news-events/fda-voices/how-fda-plans-help-consumers-capitalize-advances-science (accessed Jun. 15, 2021).
[208] P. A. Kirkwood, J. B. Munson, T. A. Sears, and R. H. Westgaard, "Respiratory interneurones in the thoracic spinal cord of the cat.," *J. Physiol.*, vol. 395, no. 1, pp. 161–192, 1988, doi: 10.1113/jphysiol.1988.sp016913.
[209] R. Shannon, "Reflexes from Respiratory Muscles and Costovertebral Joints," *Compr. Physiol.*, 2011, doi: 10.1002/cphy.cp030213.
[210] L. Trebaul *et al.*, "Stimulation artifact correction method for estimation of early cortico-cortical evoked potentials," *J. Neurosci. Methods*, vol. 264, pp. 94–102, May 2016, doi: 10.1016/j.jneumeth.2016.03.002.